Structural insights into the activation mechanism of antimicrobial GBP1

Inaugural-Dissertation
to obtain the academic degree
Doctor rerum naturalium (Dr. rer. nat.)

submitted to the Department of Biology, Chemistry, Pharmacy
of Freie Universität Berlin

by

Marius Weismehl

2024

The present work was carried out between February 2021 and January 2024 at the Max Delbrück Center for Molecular Medicine in the Helmholtz Association (MDC) under the supervision of Prof. Dr. Oliver Daumke.

1st reviewer: Prof. Dr. Oliver Daumke
2nd reviewer: Prof. Dr. Mikhail Kudryashev

Date of defense: 16.07.2024

I hereby declare that I alone am responsible for the content of my doctoral dissertation and that I have only used the sources or references cited in the dissertation.

Berlin, 17.04.2024

_____

Signature

Publications

Parts of this work have been published in the following manuscript:

Weismehl M, Chu X, Kutsch M, Lauterjung P, Herrmann C, Kudryashev M, Daumke O (2024) Structural insights into the activation mechanism of antimicrobial GBP1. *The EMBO Journal* 43: 615-636. doi: 10.1038/s44318-023-00023-y

Single particle cryo-EM and subtomogram averaging structures have been deposited in the Electron Microscopy Data Bank (EMDB) under accession codes EMD-18698 and EMD-18806, respectively. Coordinates for the membrane-bound GBP1 model have been submitted to the Protein Data Bank (PDB) under accession code 8R1A.

Table of contents

Summary

The dynamin-related human guanylate-binding protein 1 (GBP1) mediates host defenses against microbial pathogens. Upon GTP binding and hydrolysis, auto-inhibited GBP1 monomers dimerize and assemble into soluble and membrane-bound oligomers, which are crucial for innate immune responses. How higher-order GBP1 oligomers are built from dimers, and how assembly is coordinated with nucleotide-dependent conformational changes, has remained elusive.

In this thesis, medium-resolution cryo-electron microscopy-based structural data of soluble and membrane-bound GBP1 oligomers show that GBP1 assembles in an outstretched dimeric conformation, both on the surface of a simple membrane model system and within disk-like soluble oligomers composed of 30 subunits. In both oligomeric states, the surface-exposed helix α4' of the large GTPase domain has been identified to contribute to the lateral oligomerization interface. By re-analyzing and probing nucleotide- and dimerization-dependent movements of the large GTPase domain, a coordinated movement of helix α4' and α3 was shown to mediate nucleotide hydrolysis and facilitate GBP1 oligomerization and formation of an antimicrobial protein coat on a gram-negative bacterial pathogen.

Results of this thesis reveal a sophisticated activation mechanism for GBP1, in which nucleotide-dependent structural changes coordinate dimerization, oligomerization, and membrane binding to allow encapsulation of pathogens within an antimicrobial protein coat.

Zusammenfassung

Das Dynamin-verwandte humane Guanylat-bindende Protein 1 (GBP1) vermittelt Wirtsabwehr gegen mikrobielle Pathogene. Nach der Bindung und Hydrolyse von GTP dimerisieren autoinhibierte GBP1-Monomere und bilden lösliche und membrangebundene Oligomere, die für die angeborene Immunantwort entscheidend sind. Es ist jedoch unklar, wie höher geordnete GBP1-Oligomere aus Dimeren aufgebaut werden und wie die Assemblierung mit nukleotidabhängigen konformationellen Änderungen koordiniert wird.

In dieser Arbeit zeigen strukturelle Daten von löslichen und membrangebundenen GBP1-Oligomeren, die auf mittlerer Auflösung basieren, dass GBP1 in einer ausgestreckten dimeren Konformation sowohl auf der Oberfläche eines einfachen Membranmodells als auch innerhalb von scheibenförmigen löslichen Oligomeren aus 30 Untereinheiten zusammengebaut wird. In beiden oligomeren Zuständen wurde festgestellt, dass die oberflächenexponierte Helix α4' der großen GTPase-Domäne zur lateralen Oligomerisierungsschnittstelle beiträgt. Durch erneute Analyse und Untersuchung nukleotid- und dimerisierungsabhängiger Bewegungen der großen GTPase-Domäne konnte eine koordinierte Bewegung von Helix α4' und α3 aufgezeigt werden. Diese vermittelt Nukleotidhydrolyse und ermöglicht Oligomerisierung von GBP1 und Bildung einer antimikrobiellen Proteinhülle auf einem gramnegativen bakteriellen Pathogen.

Die Ergebnisse dieser Arbeit enthüllen einen ausgeklügelten Aktivierungsmechanismus für GBP1, bei dem nukleotidabhängige strukturelle Veränderungen die Dimerisierung, Oligomerisierung und Membranbindung koordinieren, um ein Einkapseln von Pathogenen in einer antimikrobiellen Proteinhülle zu ermöglichen.

1 Introduction

1.1 Innate immunity against microbial pathogens

Microbial pathogens are a major threat to health, which is why immune defenses are essential for host survival. The vertebrate immune system has evolved two branches of defense strategies: innate and adaptive immunity. The innate immune system constitutes the first line of defense. Physical and chemical barriers, such as epithelial barriers (skin and mucous membranes) and external mucous secretions of bioactive molecules, prevent pathogens from entering internal environments. Humoral and cell-mediated immune responses play a vital role in promptly recognizing and initiating a proinflammatory response against invading pathogens. In 1944, Menkin observed for the first time a fever-promoting substance in mammalian hosts that led to the discovery of endogenous soluble factors involved in inflammation, later on termed “cytokines” (Cohen et al., 1974). The discovery of the inflammatory and toxic effects of lipopolysaccharides (LPS) by Condie et al. (1955), the identification of interferons as a factor interfering with viral replication by Isaacs and Lindenmann (1957), and the characterization of dendritic cells as potent stimulators of lymphocytes by Steinman and Witmer (1978) are only some of the main findings that contributed to the concept of innate immunity.

In contrast to the innate immune response, the adaptive immune system specifically targets and combats pathogens in the late phase of infection and generates immunological memory (Burnet, 1976). While antigen-specific receptors on lymphocytes trigger adaptive immune responses, innate immune responses against microbial pathogens are mediated by phagocytic cells such as macrophages and dendritic cells. Janeway (1989) postulated that recognition of microbial molecules by pattern recognition receptors discriminates self from invading pathogens and activates the immune system. With the discovery of Toll-like receptors as sensors for innate immune responses by Lemaitre et al. (1996) and Poltorak et al. (1998), the mechanism that triggers the activation of innate immunity has been decoded. Activation of the innate immune response initiates the secretion of proinflammatory cytokines, the activation of inflammasome complexes that trigger inflammatory cell death, and the recruitment of immune effector cells to eliminate pathogens or infected cells.

1.1.1 Pathogen recognition by PAMPs

Pathogen recognition is mediated by recognizing evolutionary conserved repetitive molecules on pathogens, termed pathogen-associated molecular patterns (PAMPs), through pattern recognition receptors (PRRs). PAMP recognition triggers PRR-induced downstream signaling pathways to fight off pathogenic invaders by activating gene expression and synthesis of proinflammatory cytokines and chemokines (Akira et al., 2006). Different classes of microbial pathogens display several different but also common PAMPs which are recognized by a range of PRRs (Figure 1) (Mogensen, 2009). As a key feature of pathogen recognition, several PRRs become stimulated at the same time through a variety of PAMPs (Akira et al., 2006). Toll-like receptors (TLRs) comprise the major class of PRRs and are transmembrane proteins localized at the cellular or endosomal membranes. Bacterial pathogens might be recognized by their unique components of the cell wall. Examples include lipoproteins, peptidoglycan, lipopolysaccharides in gram-negative bacteria, and lipoteichoic acid in gram-positive bacteria. Also flagellin proteins of the bacteria flagella and bacterial DNA containing unmethylated CpG motifs are recognized by TLRs (Hayashi et al., 2001; Hemmi et al., 2000). Similarly, β-glycans of the fungal cell wall and GPI-mucin and glycoinositol-phospholipids of protozoan parasites are sensed by TLRs (Mogensen, 2009). Viral pathogens might be recognized by TLRs via their genetic material (DNA, dsRNA, ssRNA) and surface glycoproteins. Another class of PRRs recognizes cytoplasmic PAMPs such as RIG-1-like receptors (RLRs) and NOD-like receptors (NLRs). While RLPs comprise a class of interferon-

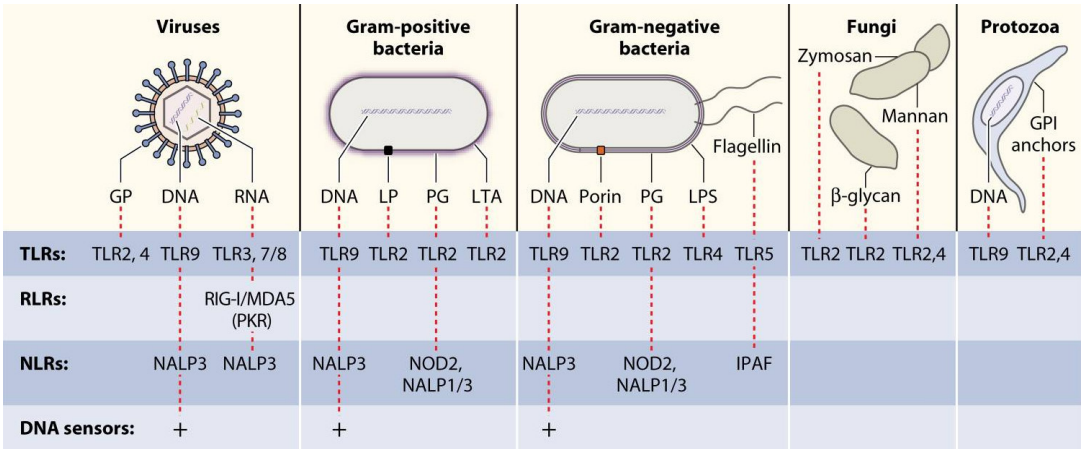

Figure 1. Pathogen recognition through pathogen-associated molecular patterns (PAMPs). Different classes of pathogens exhibit various unique but also common PAMPs recognized by a set of pattern recognition receptors (PRRs). GP: glycoproteins, LP: lipoproteins, PG: peptidoglycans, LTA: lipoteichoic acid, LPS: lipopolysaccharides, TLRs: Toll-like receptors, RLPs: RIG-1-like receptors, NLRs: NOD-like receptors. From Mogensen (2009).

inducible RNA helicases that detect cytoplasmic RNA, NLRs are innate immune receptors which sense microbial components in the cytosol, i.e. bacterial peptidoglycan fragments (Kanneganti et al., 2007; Yoneyama et al., 2004). These examples indicate that despite the pathogen diversity in nature, pathogen recognition follows relatively similar mechanisms.

1.1.2 Lipopolysaccharide – a bacterial toxin of gram-negative bacteria

The cell wall of gram-negative bacteria is composed of an inner membrane, a thin peptidoglycan layer, a periplasmic space, and an outer membrane that contains complex LPS. As a major component of the outer membrane, LPS ensures the integrity of the bacterial membrane and protects gram-negative bacteria, such as *E. coli*, *Salmonella*, and *Shigella*, from its surroundings (Papo and Shai, 2005). LPS is a bacterial endotoxin and serves as PAMP for recognizing gram-negative bacteria and triggering inflammation. High exposure of LPS may cause a range of pathological conditions including fever, septic shock, and neuroinflammation which has been shown to lead to neurodegenerative pathology under systematic exposure (Batista et al., 2019; Brown, 2019; Kell and Pretorius, 2015; Kozak et al., 1994; van der Poll et al., 2017).

LPS is an amphiphilic molecule comprising lipid A, a core domain, and the O-antigen (Figure 2). Above a critical concentration, its amphiphilic property allows for the formation of LPS micelles (Gutsmann et al., 2007). The structure of LPS can be summarized as follows (Erridge et al., 2002; Kalynych et al., 2014; Raetz and Whitfield, 2002): the O-antigen is the outermost domain of LPS and is built of repetitive O-units of three to six sugar residues. These O-units form polymers of various lengths and differ in composition and chemical linkage of their individual carbohydrate subunits for different bacteria strains. Smooth LPS exhibits full O-antigen whereas rough LPS lacks O-antigen. The O-antigen is bound to the outer core of the core domain that consists of at least three β-1,3-linked hexoses and is β-1,3-linked to a heptose of the inner core. The inner core comprises two to three heptoses attached to the base of one to three KDOs (3-Deoxy-D-*manno*-oct-2-ulosonic acid). The base is α-2,6-linked to lipid A. Lipid A is the hydrophobic anchor of LPS and contains two β-1,6-linked phosphorylated glucosamines attached to multiple β-hydroxy acyl chains with additional acyl chains attached to the β-hydroxy group. These chains vary in length between 10 and 16 carbons. The toxic property of LPS mainly originates from the lipid A portion that is one of the most potent PAMPs known (Akira et al., 2006; Park et al., 2009; Trent et al., 2006). Structural differences in lipid A

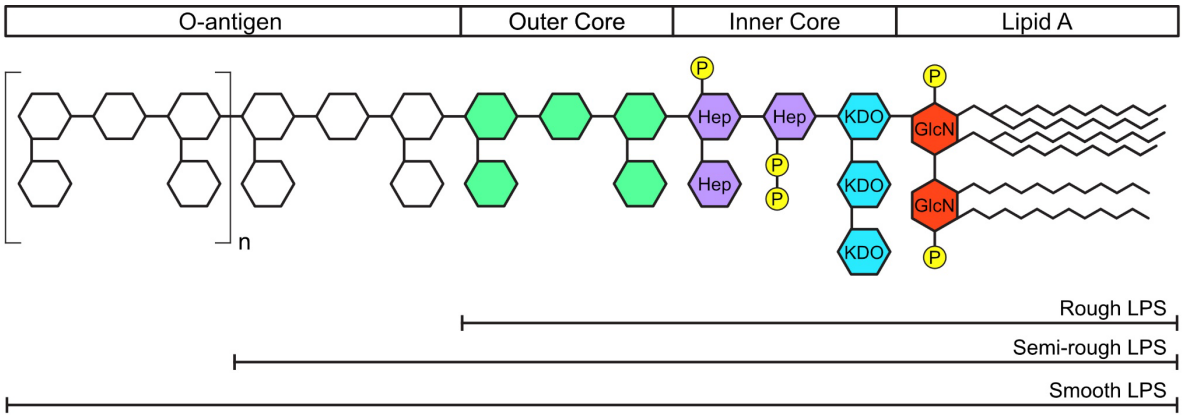

Figure 2. General structure of lipopolysaccharide (LPS). LPS consists of lipid A, an inner and outer core, and the O-antigen. Lipid A is built of two phosphorylated (P, yellow) glucosamines (GlcN, red) and several acyl chains. The inner core comprises three KDOs (3-Deoxy-D-manno-oct-2-ulosonic acid, cyan) and two to three heptose (purple) that may be phosphorylated with phosphate, pyrophosphate, 2-aminoethylphosphate and 2-aminoethylpyrophosphate (P, yellow). The outer core comprises at least three hexoses (green). The O-antigen is built of repetitive O-units of three to six sugar residues (white). Presence and length of the O-antigen define its classification into rough, semi-rough, and smooth LPS. Adapted from Page et al. (2022).

and LPS determine the pathogenicity of a bacterial strain (Backhed et al., 2003). LPS detached from the bacteria, e.g., during replication, as result of death or lysis, or through secretion via bacterial outer membrane vesicles (Kulp and Kuehn, 2010; Page et al., 2022), activates cell surface Toll-like receptor 4 (TLR4) signaling, which leads to the expression of transcription regulators and the production of cytokines and chemokines such as interleukin-1β and type-I interferons. Intracellular sensing of LPS and signaling ultimately results in the activation of the non-canonical inflammasome, the initiation of pyroptosis and cytokine release, and the clearance of intracellular bacterial pathogens by macrophages (Page et al., 2022).

1.1.3 Inflammatory and antimicrobial responses

An infection with antimicrobial pathogens leads to the induction and expression of genes involved in inflammatory responses and antimicrobial host defenses, such as pro-inflammatory cytokines, type-I interferons, and chemokines (Akira and Takeda, 2004; Akira et al., 2006). Central key players in these signaling cascades are cytosolic supramolecular inflammasome complexes that activate inflammatory caspases resulting in the processing of the pro-inflammatory cytokine interleukin-1β (IL-1β) and pyroptotic cell death (Figure 3) (Jimenez Fernandez and Lamkanfi, 2015; Martinon et al., 2002; Rathinam and Fitzgerald, 2016). In infections with microbial pathogens, Toll-like receptor (TLR) signaling induces transcription

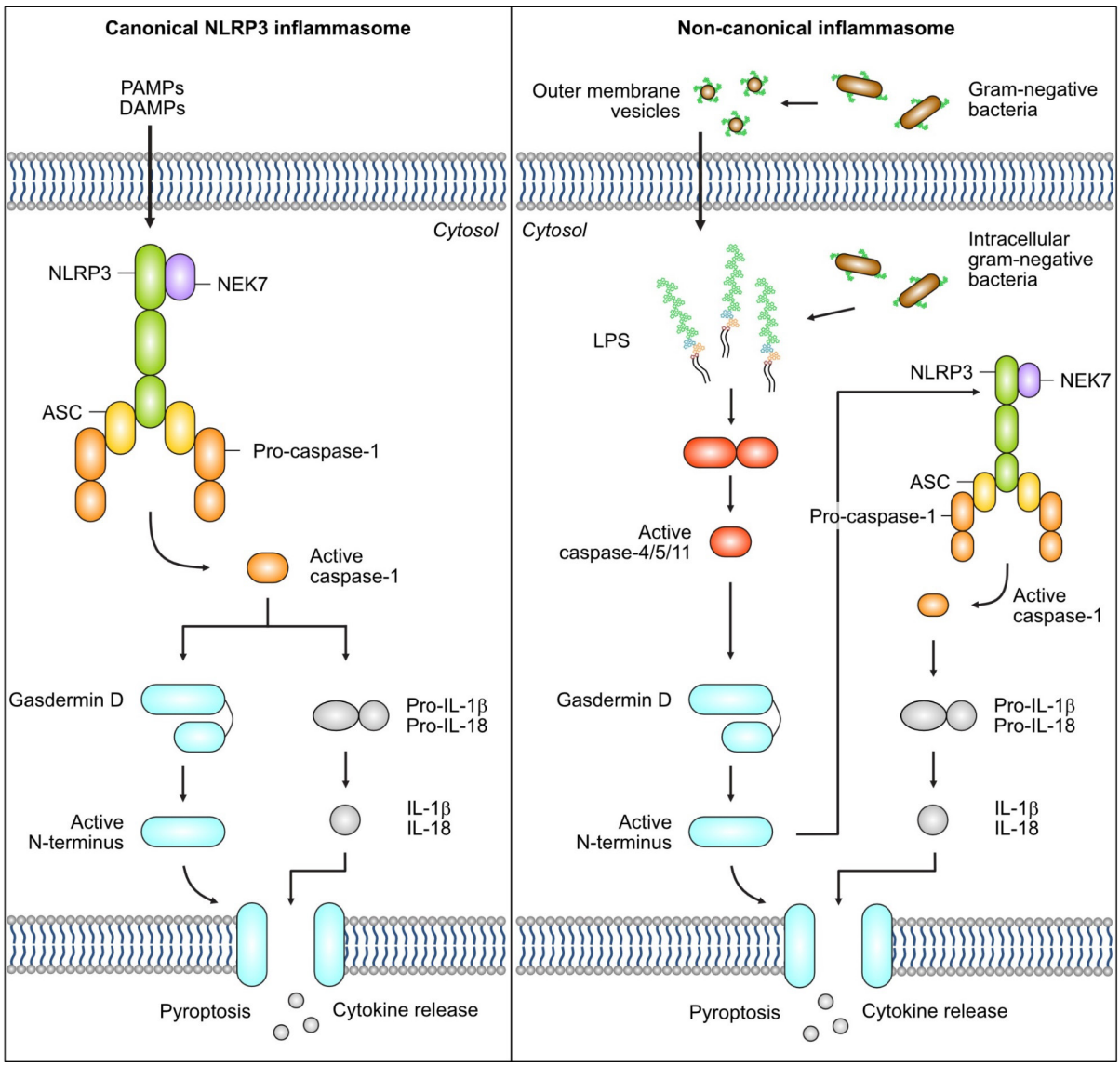

Figure 3. Canonical NLRP3 and non-canonical inflammasome pathways. Recognition of pathogen-associated patterns (PAMPs) or danger-associated molecular patterns (DAMPs) activates the canonical NLRP3 inflammasome. NEK7 is recruited and stabilizes the NLRP3 inflammasome complex. Pro-caspase-1 is recruited by ASC and active caspase-1 proteolytic cleaves pro-IL-1β and gasdermin D initiating pore complex formation and pyroptosis. Mature IL-1β is released as result of pyroptotic cell death. The non-canonical inflammasome caspases-4/5 (human) and caspase-11 (mice) sense cytosolic LPS, become active, and proteolytic cleave gasdermin D triggering pyroptosis and cytokine release via the canonical NLRP3 inflammasome caspase-1 pathway. Adapted from Man (2018) and Rathinam and Fitzgerald (2016).

of the IL-1β precursor (pro-IL-1β) that only becomes active upon proteolytic cleavage mediated by activated caspase-1. Caspase-1 is activated upon ligand sensing and assembly of several family members of canonical inflammasomes (Martinon et al., 2002). Canonical inflammasomes recognize different PAMPs and danger-associated molecular patterns (DAMPs, e.g., ATP and uric acid) through their individual NOD-like receptor (NLR) (Davis et

al., 2011; Kanneganti et al., 2007). For example, the NLRP7 inflammasome recognizes bacterial lipopeptides (Khare et al., 2012), while the NLRP3 inflammasome recognizes a wide range of PAMPs and is the best characterized family member. It comprises the NLR family member NLRP3, the adaptor protein ASC (apoptosis-associated speck-like protein containing a caspase recruitment domain), and pro-caspase-1. NLRP3 has a C-terminal leucin-rich repeat (LRR) domain sensing PAMPs, a central nucleotide binding domain (NBD or NACHT domain), and an N-terminal pyrin domain (PYD) that interacts with the N-terminal PYD of ASC, thereby recruiting its adaptor protein. The C-terminal caspase recruitment domain (CARD) of ASC interacts with the N-terminal CARD of pro-caspase-1 facilitating its autoproteolytic cleavage and activation. On one hand, active caspase-1 proteolytically cleaves accumulated pro-IL-1β resulting in the secretion of active IL-1β from the cell and the initiation of IL-1β-mediated downstream signaling (Kanneganti et al., 2007; Martinon et al., 2002; Thornberry et al., 1992). On the other hand, it proteolytically cleaves gasdermin-D (GSDMD) initiating pyroptosis. In its auto-inhibited state, the C-terminal domain (CT-GSDMD) binds to the N-terminal domain (NT-GSDMD), thus preventing the formation of membrane pores. Caspase-1-mediated cleavage allows NT-GSDMD to oligomerize and insert into the plasma membrane which results in membrane perforation and permeabilization (Devant and Kagan, 2023). Besides caspase-1, human caspase-4 and caspase-5 (or caspase-11 in mice) activated by the non-canonical inflammasome also cleave and activate GSDMD (Downs et al., 2020; Kayagaki et al., 2015). These non-canonical caspases directly sense lipopolysaccharides (LPS), presumably through several positively charged motifs in their CARD, which induces its catalytic activity (Shi et al., 2014). Active caspases of the non-canonical inflammasome further contribute to the release of cytokines via a secondary activation of the canonical NLRP3 inflammasome caspase-1 pathway (Downs et al., 2020).

The mature and active cytokine IL-1β is an essential mediator of the inflammatory response (Weber et al., 2010). Downstream signaling via various pathways leads to the activation of the transcription factors NFκB, c-Jun, c-Fos, c-Myc, and ATF2, that regulate expression of many pro-proliferative and host defense proteins, such as pro-inflammatory cytokines IL-1, IL-6 and IL-8, tumor necrosis factor α (TNF-α) and Interferon-γ (IFN-γ). In response to PAMPs, IL-1β signaling thereby mediates a large number of antimicrobial processes, including immune cell recruitment, activation, and differentiation, cell proliferation, and pathogen clearance (Oeckinghaus and Ghosh, 2009; Weber et al., 2010).

Like IL-1β, the cytokine IFN-γ plays an important role in many antimicrobial processes (Tau and Rothman, 1999). For example, it up-regulates the major histocompatibility (MHC) class I and II antigen presentation pathway, which promotes the recognition of foreign peptides from intracellular pathogens by cytotoxic T cells and accelerates CD4+ T cell activation (Boehm et al., 1997; Schroder et al., 2004). Moreover, IFN-γ stimulates macrophage-mediated clearance of pathogens by increasing their ability for pinocytosis and receptor-mediated phagocytosis, and by promoting pathogen degradation through autophagy (Page et al., 2022; Xu et al., 2007). Microbial killing is further enhanced by increasing the activity of enzymes involved in the production of reactive oxygen species (ROS) and reactive nitrogen intermediates (RNI), resulting in cellular stress and inflammatory signaling (Park et al., 2004). IFN-γ has also been shown to prime microphages in response to LPS, which enables a faster and intensified response in bacterial clearance (Jurkovich et al., 1991). At the same time, IFN-γ induces a set of antimicrobial genes to combat infections. One prominent group that is essential for IFN-mediated cell-autonomous pathogen control is the family of IFN-induced GTPases belonging to the dynamin superfamily proteins (Rafeld et al., 2021). Members of the IFN-induced GTPase family can be divided into one of the following subfamilies based on their molecular mass (Kim et al., 2012; MacMicking, 2004): 21-47 kDa immunity-related GTPases (IRGs), 65-73 kDa guanylate-binding proteins (GBPs), 72-82 kDa myxovirus (MX) resistance proteins, 200-285 kDa very large inducible GTPases (VLIGs/GVINs). In infected cells, GTPases of the IRG and GBP family promote oxidative stress responses, autophagy, membrane lysis including the disruption of pathogen-containing vacuoles, and assembly of the inflammasome complex (Feeley et al., 2017; Rafeld et al., 2021).

1.2 Guanylate-binding proteins (GBPs)

IFN-stimulated genes (ISGs) encoding antimicrobial or immune-modulating proteins are a central pillar in IFN-induced cell-autonomous immunity (Borden et al., 2007). In 1983, biochemical experiments with IFN-primed human fibroblasts led to the identification of an IFN-induced protein with a molecular mass of roughly 65 kDa (Cheng et al., 1983). In this approach, the protein bound to beads with immobilized guanine nucleotides. Hence, this protein is known as human guanylate-binding protein 1 (GBP1). Since then, the protein family of guanylate-binding proteins has been expanded, with GBP1 as the best characterized and central member in GBP-mediated immunity.

1.2.1 Members of the dynamin superfamily

Guanylate-binding proteins (GBPs) are interferon-inducible, dynamin-related GTPases that mediate cell-autonomous immunity against a wide range of microbial pathogens (Kutsch and Coers, 2021; MacMicking, 2012; Meunier and Broz, 2016; Praefcke, 2018; Santos and Broz, 2018). As members of the dynamin superfamily proteins (DSPs), they share evolutionarily conserved structural features, such as a large GTPase (LG) domain or G-domain and a helical bundle comprising a middle domain (MD) and a GTPase effector domain (GED) (Figure 4) (Praefcke and McMahon, 2004; Prakash et al., 2000a). DSPs, including GBPs, are mechano-chemical GTPases that assemble into regular oligomers and function as molecular switches controlled by nucleotide binding and hydrolysis (Daumke and Praefcke, 2016; Kutsch and Coers, 2021). GBPs share the common features of DSPs in having low nucleotide binding affinities, displaying an oligomerization-dependent increase in GTPase activity, and interacting with lipid membranes (Daumke and Praefcke, 2016; Ghosh et al., 2006; Praefcke et al., 2004; Praefcke and McMahon, 2004; Prakash et al., 2000a).

While classical dynamins localize to plasma membranes, trans-Golgi network, endosomes, caveolae, and phagosomes functioning in clathrin-mediated and non-clathrin-mediated budding events, other members are involved in mitochondrial fission (dynamin-related protein 1, Drp1) and fusion events (mitofusins and optic atrophy 1, OPA1), caveolae stabilization (Eps15 homology proteins, EHDs), ER tubule fusion (atlastins, ATLs), or plant

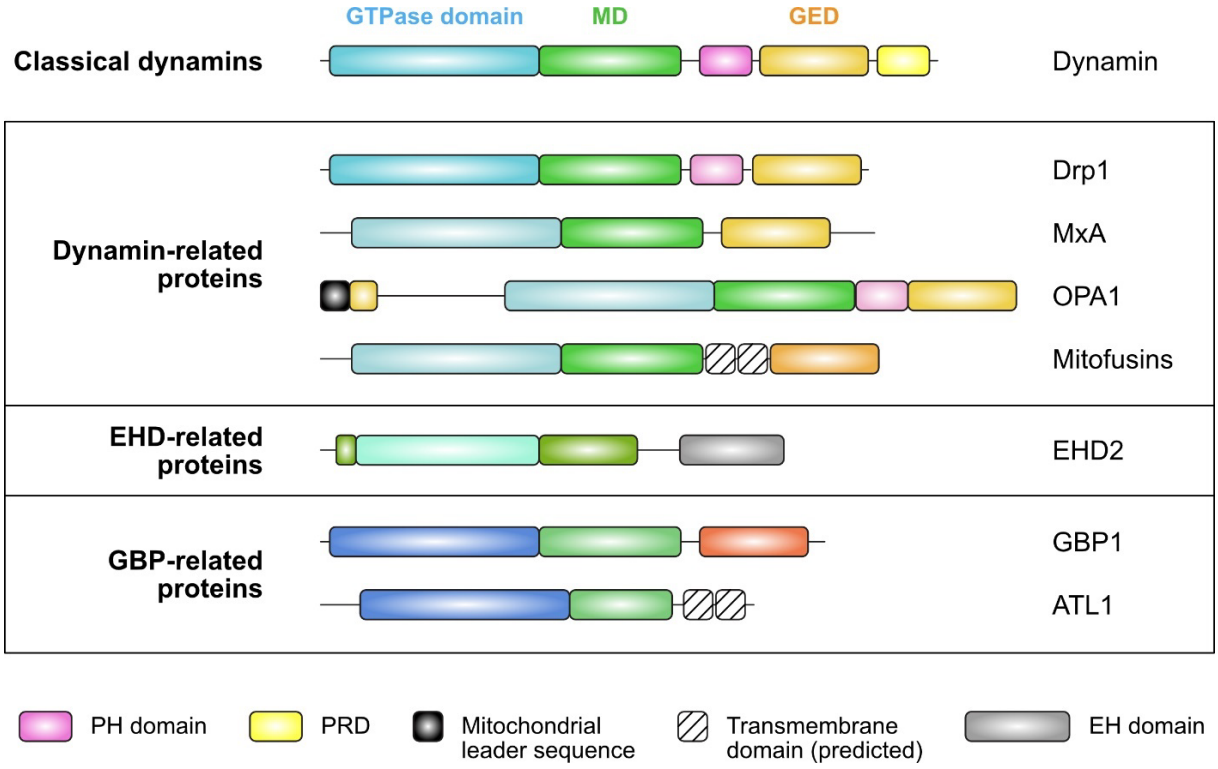

Figure 4. Domain architecture of dynamin superfamily proteins. Domains are represented by different color und different shade depending on their sequence homology. The common structure is denotated for classical dynamins comprising the GTPase domain (cyan/blue), middle domain (MD, green), and GTPase effector domain (GED, orange/red). In dynamin, the MD and GED are also referred to as stalk domains. Adapted from Praefcke and McMahon (2004).

cell cytokinesis (e.g., *Arabidopsis* dynamin-like proteins, ADLs) (Figure 5) (Hales and Fuller, 1997; Hu et al., 2009; Kang et al., 2003; Labrousse et al., 1999; Olichon et al., 2002; Orso et al., 2009; Praefcke and McMahon, 2004; Ramachandran and Schmid, 2018; Stoeber et al., 2012). The functional activities of DSPs are, however, not restricted to membrane remodeling processes only. They further include membrane-independent functions, as some members, including proteins of the GBP and Mx family, are interferon-inducible GTPases that mediate microbial resistance and showing antiproliferative activities (Figure 5) (Daumke and Praefcke, 2016; Kutsch and Coers, 2021; Pilla-Moffett et al., 2016; Ramachandran and Schmid, 2018; Staeheli et al., 1986).

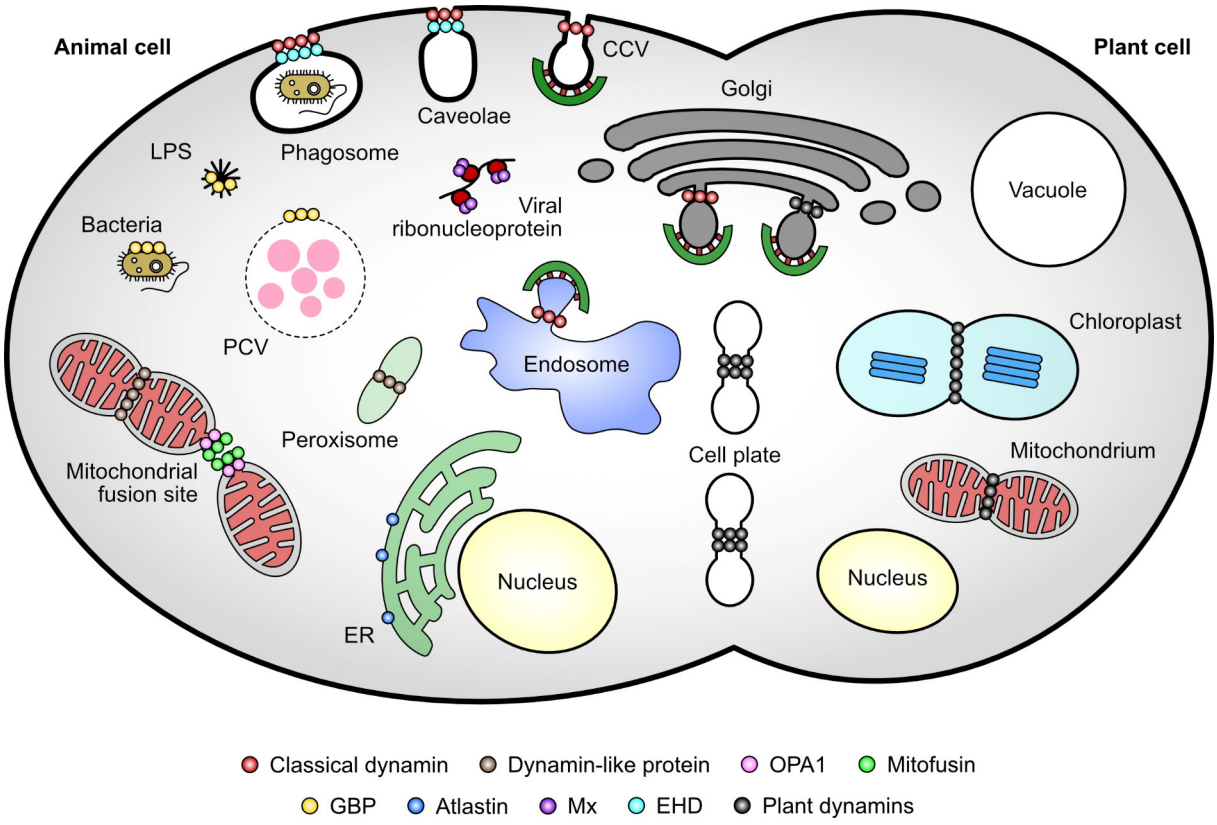

Figure 5. Cellular location and function of dynamin superfamily proteins. CCV: clathrin-coated vesicle, EHD: Eps15 homology protein, ER: endoplasmic reticulum, GBP: guanylate-binding protein, LPS: lipopolysaccharide, Mx: Myxovirus resistance protein, OPA1: optic atrophy 1, PCV: pathogen-containing vacuole. Modified from Praefcke and McMahon (2004).

1.2.2 Structure and domain architecture of GBPs

Structurally, GBPs are composed of a dynamin-related large GTPase (LG) domain that features a unique "guanine cap" around the nucleotide-binding site, a helical middle domain (MD, α7-11), and a helical GTPase effector domain (GED, α12-13). The crystal structure of full-length GBP1 describes a closed monomeric conformation (Figure 6, left) (Prakash et al., 2000a). In this conformation, the GED folds back interacting with the LG domain via a salt bridge network (Vopel et al., 2010) and a C-terminal farnesyl moiety is harbored in a hydrophobic pocket (Ji et al., 2019). In the dimeric state, GTP binding and hydrolysis lead to large structural rearrangements of the MD and, presumably, the GED (Figure 6, right) (Cui et al., 2021; Kuhm et al., 2023). GBP paralogs share an overall sequence identity of 54% to 88% (Olszewski et al., 2006). While the LG domains are most conserved, the GEDs display the

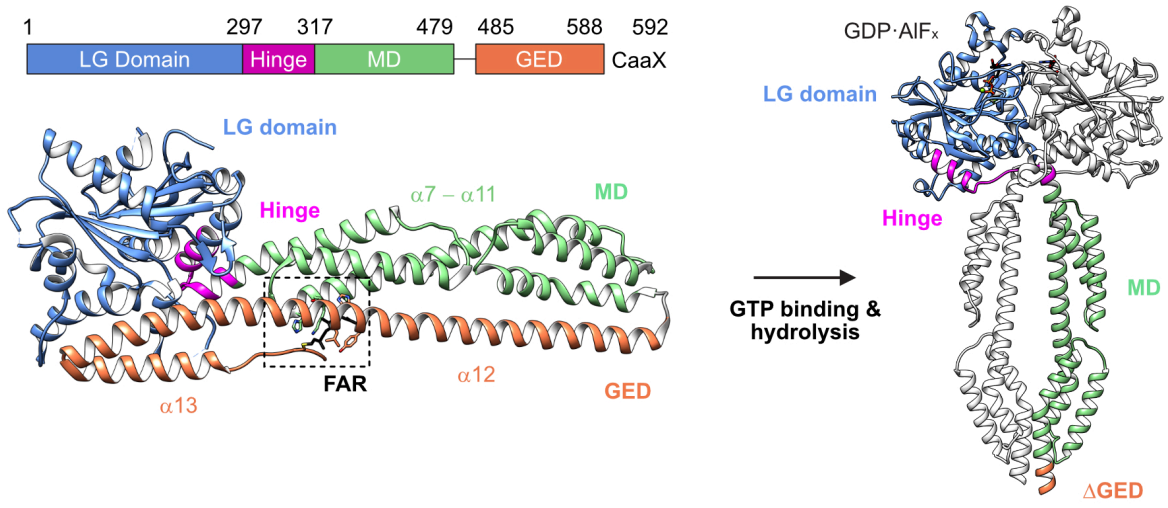

Figure 6. Crystal structure of monomeric and dimer GBP1. Left: Domain architecture of farnesylated human GBP1 (PDB 6k1z) in its nucleotide-free, monomeric state. The farnesyl moiety (black, FAR) is harbored in a hydrophobic pocket (dashed box) making it inaccessible to bind to membranes (Ji et al., 2019). Right: Domain architecture of dimeric human GBP1 (PDB 7e59) generated as SWISS-MODEL (Waterhouse et al., 2018) based on the published crystal structure of GBP5-ΔGED bound to the GTP transition state analogue GDP•AlF_x. LG: large GTPase, MD: middle domain, GED: GTPase effector domain.

greatest divergence. In contrast to dynamin, GBPs carry neither a pleckstrin homology (PH) domain nor a proline-/arginine-rich domain (PRD), which would provide additional protein interaction sites (Faelber et al., 2011; Prakash et al., 2000a).

Three of the seven human GBP members are post-translationally farnesylated (GBP1) or geranylgeranylated (GBP2 and GBP5), facilitating their membrane interaction (Britzen-Laurent et al., 2010; Olszewski et al., 2006). Covalent attachment of hydrophobic isoprenoid groups of 15-carbon (farnesyl) or 20-carbon (geranylgeranyl) to cysteines via thioether linkage is mediated by a C-terminal prenylation motif. This motif is the CaaX box and consists of the cysteine (C), which will be prenylated, two aliphatic amino acids (aa), and an amino acid that determines the type of prenylation (X). While farnesyltransferases (FTase) recognize CaaX box motifs ending in either a methionine, serine, alanine, or glutamine, geranylgeranyl-transferases I and II (GGTase I and II) recognize motifs ending in leucin (Novelli and D'Apice, 2012). Examples of other lipid anchors are the GPI anchor attached to C-terminal carboxyl groups via amide linkage and fatty acid tails through myristoylation of N-terminal glycines via amide linkage or through palmitoylation of specific cysteines via thioester linkage. Lipid anchors not only mediate membrane association but might also be involved in protein-protein interactions, e.g., through prenyl-binding domains (Kloog and Cox, 2004).

Among members of the dynamin superfamily, the LG domain is the most highly conserved region (Figure 7A). In comparison to Ras-like GTPases, LG domains of DSPs display various insertions that vary in length and position between members (Daumke and Praefcke, 2016; Niemann et al., 2001). Nucleotide-binding in the LG domain is mediated by the consensus G1-G4 motifs (Saraste et al., 1990). In GBP1, but not in other GTPase families, the ribose is additionally stabilized by a phosphate and guanine cap (Prakash et al., 2000b). These two unique features are highly flexible in the monomeric nucleotide-free state. Upon

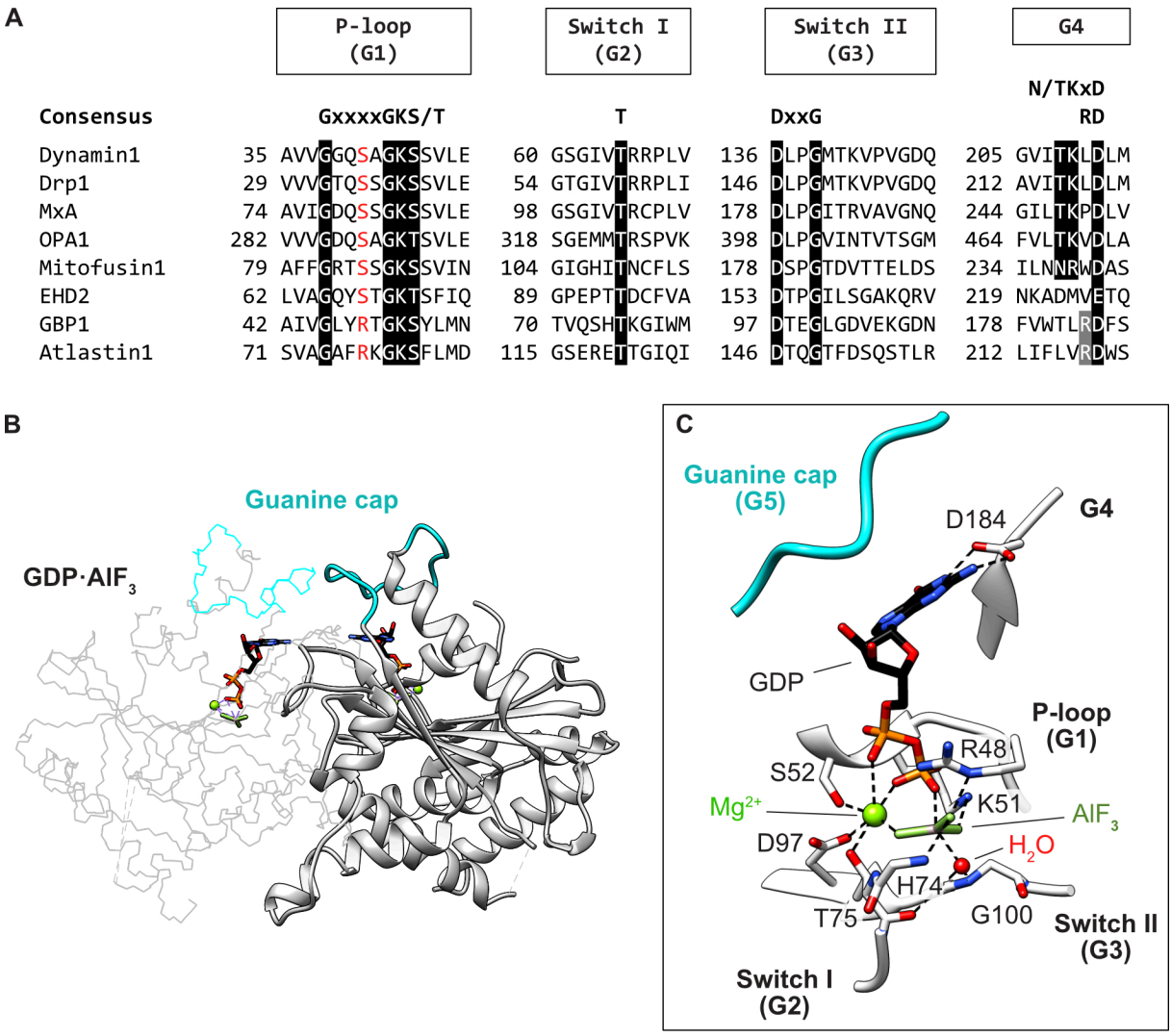

Figure 7. Dynamin superfamily proteins: GTPase domain. (A) Sequence alignment of G1-G4 motifs of selected members of the dynamin superfamily. Conserved canonical residues are highlighted in black or dark gray. The catalytic arginine and serine in the P-loop are shown in red. UniProt accession number: Q05193 (human dynamin1), O00429 (human Drp1), P20591 (human MxA), O60313 (human OPA1), Q8IWA4 (human mitofusin1), Q9NZN4 (human EHD2), P32455 (human GBP1), Q8WXF7 (human atlastin1). **(B)** Structure of the large GTPase dimer of GBP1 in complex with GDP•AlF_x (PDB 2b92). **(C)** Close view of the nucleotide binding pocket and catalytic mechanism of GBP1. Adapted from Daumke and Praefcke (2016).

GTP binding, the guanine cap becomes ordered and forms a hydrophobic pocket stabilizing the guanine base (Ghosh et al., 2006). The phosphate cap, in turn, covers the phosphate groups of GTP (Prakash et al., 2000b). Motif G1 or "P-loop" comprises the consensus GxxxxGK(S/T) and encloses the phosphate groups. Motif G2 and G3 bind the γ-phosphate and undergo nucleotide-dependent structural changes ("switch regions"). In GBP1, G2 is in the unique phosphate cap replacing the canonical switch I; G3 is located in switch II. The conserved Ser52 of the P-loop, the conserved Thr75 of G2, and the conserved Asp97 of G3 coordinate the GTPase cofactor Mg^{2+} which bridges the β- and γ-phosphate (Figure 7B, C) (Ghosh et al., 2006; Praefcke et al., 1999; Prakash et al., 2000a). As for atlastins, motif G4 comprises a conserved arginine-aspartate (RD) guanine base-binding motif in GBPs (Bian et al., 2011; Byrnes and Sondermann, 2011; Praefcke et al., 1999; Prakash et al., 2000b). The RD motif replaces the canonical (N/T)KxD of most GTPases.

1.2.3 GTPase activity of GBPs

Like other dynamin superfamily members, GBPs dimerize via a highly conserved surface across the nucleotide-binding site, the "G interface", leading to stimulation of their GTPase activity (Daumke and Praefcke, 2016; Ghosh et al., 2006). GTP binding promotes the formation of a head-to-head dimer via the G interface (Figure 7B) (Ghosh et al., 2006; Wehner et al., 2012). In-depth structural studies of GBP1 show that the phosphate cap and switch II undergo structural repositioning and are stabilized in the dimeric conformation. Both contribute to the G interface. Additional loop regions including the P-loop participate in the G interface and interact with the guanine base *in trans* (Figure 7C) (Wehner et al., 2012). In the dimeric state of GBP1, Ser73 and Thr75 of the phosphate cap position a catalytic water molecule preparing for a nucleophilic attack to cleave the phosphoanhydride bond between the γ- and β-phosphate (Ghosh et al., 2006). The catalytic Arg48 of the P-loop, termed "arginine finger", now faces toward the nucleotide binding pocket and stabilizes the negative charge of the GTP hydrolysis transition state (Ghosh et al., 2006; Praefcke et al., 2004), similar to the cation-dependent GTP hydrolysis mechanism of other DSPs (Ash et al., 2012).

GBP1 is the best characterized GBP member. Upon GTP hydrolysis, intramolecular rearrangements induce an opening of each protomer by disrupting a salt bridge network between Arg227 and Lys228 of the LG domain and four aspartates of the GED, thereby releasing the farnesyl moiety (Ince et al., 2021; Sistemich et al., 2020; Vopel et al., 2010). Time-

resolved Förster resonance energy transfer (FRET)-studies found that the open GBP1 conformation is stabilized by MD:MD interactions (Sistemich et al., 2020). Structural data of the GBP5 and GBP1 dimers showed a rotation and crossover of its MDs which is stabilized via intermolecular MD:MD interactions (Figure 6, right) (Cui et al., 2021; Kuhm et al., 2023). However, the GED is missing in these constructs and thus, there is no structural knowledge of full-length GBPs.

GBP1 and GBP3 share the unique ability to hydrolyze GTP in two consecutive cleavage steps to guanosine monophosphate (GMP). This is achieved by repositioning the nucleotide within the nucleotide-binding pocket after the first hydrolysis step (Ghosh et al., 2006; Schwemmle and Staeheli, 1994). In this conformation, the released γ-phosphate is now replaced by the β-phosphate and the same catalytic process including the same catalytic residues can be used to hydrolyze GDP to GMP. This appears to be a unique feature among DSPs (Daumke and Praefcke, 2016). While GBP2 has a significantly reduced efficiency to catalyze the second hydrolysis step, GBP5 only hydrolyzes GTP to GDP. Xavier et al. (2020) identified Gly68 in switch I, which could constitute the mechanistic differences between GBP1, GBP2, and GBP5 in GDP hydrolysis. The functional differences, however, remain unclear.

1.2.4 Oligomerization of GBPs

As stated earlier, members of the dynamin superfamily share the ability to assemble into regular oligomers, thereby functioning as mechano-chemical enzymes (Daumke and Praefcke, 2016; Praefcke and McMahon, 2004). Dynamin, for example, has been shown to assemble on membrane into helical filaments templates via the helical stalk domain (Chappie et al., 2011; Faelber et al., 2019; Faelber et al., 2011; Hinshaw and Schmid, 1995; Kong et al., 2018; Reubold et al., 2015; Takei et al., 1995). Three main interfaces in the stalk domain are described that stabilize the crisscrossed dimer and further enable the assembly of two stalk dimer *in trans*. Upon nucleotide hydrolysis, dynamin filaments employ a power stroke mechanism leading to membrane constriction and friction (Ganichkin et al., 2021; Mears et al., 2007; Morlot et al., 2010; Roux et al., 2006).

In the human GBP family, GBP1-3 and GBP5 have been shown to dimerize when bound to GTP. The GTP-binding and hydrolysis-induced open GBP1 conformation not only promotes membrane interaction and oligomerization of GBP1 dimers on lipid membranes but also facilitates self-oligomerization into soluble tubular polymers (Figure 8) (Shydlovskyi et al.,

2017; Sistemich et al., 2021; Sistemich et al., 2020). For both oligomeric states, it has been proposed that the GBP1 dimer exhibits an outstretched conformation with the LG domains facing outwards, based on low-resolution electron microscopy data (Kuhm et al., 2023; Shydlovskyi et al., 2017; Zhu et al., 2024) and by employing FRET to elucidate intra- and intermolecular changes in the distances between protein domains (Shydlovskyi et al., 2017; Sistemich et al., 2021; Sistemich et al., 2020). While the released farnesyl moiety attaches to lipid membranes stabilizing GBP1 dimers in the membrane-bound state, it is also crucial for mediating self-polymerization. As shown by Sistemich et al. (2020), GBP1 assembles into small polymeric units as soon as a critical concentration of GBP1 dimers is reached. In the initial small disk-like polymers, the farnesyl moiety is supposed to be in a hydrophobic core in the center of the disk. Cooperative GTP hydrolysis stabilizes these small polymers and promotes further assembly of larger polymeric structures. Only recently have studies focused on mechanistic and immunological relationships which show that both the membrane-bound and the polymeric GBP1 state are crucial in mediating host defense against microbial pathogens as described in detail in 1.3. Of the geranylgeranylated paralogs GBP2 and GBP5, only GBP2 can self-polymerize. However, both GBP2 and GBP5 can form mixed polymers with GBP1 (Dickinson et al., 2023). This is supported by the finding that GBP1-3 and GBP5 dimerize both as homo- and heterodimers (Kutsch et al., 2018). Homodimers of prenylated GBP1, GBP2, and GBP5 can all bind to host membranes, whereas nonprenylated members are recruited to membranes via hetero-interactions with prenylated paralogs (Britzen-Laurent et al., 2010). Structural studies of the GBP1 and GBP5 homodimers show that lateral interactions between

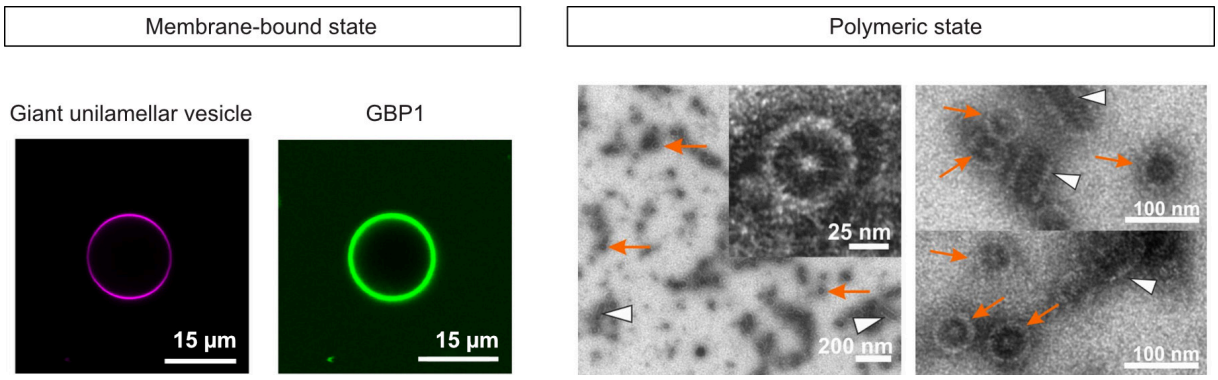

Figure 8. GBP1 oligomerization states. Left: AF-488 labeled GBP1 (green) incubated with GDP•AlF_x binds to rhodamine red labeled giant unilamellar vesicles (GUVs, magenta) (Sistemich et al., 2021). Right: GBP1 incubated with GTP polymerizes into ring-like structures (orange arrows) and tubular, elongated structures (white arrowheads) (Shydlovskyi et al., 2017).

two LG domains (G interface) and between two MDs stabilize the open conformation (Cui et al., 2021; Kuhm et al., 2023). How the oligomeric interfaces between GBP dimers are built and how nucleotide hydrolysis coordinates the higher-order GBP assemblies has remained unknown.

1.2.5 Antimicrobial activities of GBPs

GBPs are key players in innate immunity against microbial pathogens and demonstrate versatile functionality. Numerous studies show their importance, particularly in combating bacterial infections (Figure 9) (Kutsch and Coers, 2021; Rivera-Cuevas et al., 2023). On one hand, GBPs enhance the activation of the noncanonical inflammasome resulting in caspase-4-dependent pyroptosis, as shown during bacterial infections with *Legionella pneumophila*, *Salmonella typhimurium*, or *Shigella lexneri* (Bass et al., 2023; Santos et al., 2020; Wandel et al., 2020). On the other hand, GBPs activate the canonical inflammasome by means of the lytic breakdown of invading bacteria and release of pathogen-associated molecular patterns (PAMPs), as shown in *Francisella novicida* or *Toxoplasma gondii* infections (Fisch et al., 2020; Man et al., 2015; Meunier et al., 2015), or through GBP1-dependent GMP production and catabolism into uric acid, a DAMP that activates the NLRP3 inflammasome (Xavier et al., 2020). Although great progress has been made in studying GBPs' antibacterial functions, a more comprehensive molecular and mechanistic understanding of the individual role of each member in inflammatory responses is required. In this sense, GBPs also bind to and disrupt pathogen-containing vacuoles (PCVs), but how they recognize and rupture PCVs is still largely unknown (Coers, 2013; Kutsch and Coers, 2021).

Besides its antibacterial activity, GBPs convey immunity against viral pathogens. In general, GBPs interfere with the viral replication mechanism and boost type-I interferon production in response to viral PAMPs (Feng et al., 2017; Kim et al., 2012). For example, they affect viral capsid trafficking by remodeling the actin cytoskeleton, block maturation of HIV envelope proteins and impair with the activity of the RNA-dependent RNA polymerase of hepatitis C virus (HCV) (Itsui et al., 2009; Krapp et al., 2016; Zou et al., 2017). In contrast, GBP1 has been shown to be induced by HCV and to act as a pro-viral factor for the HCV life cycle (Bender et al., 2024), pointing out that the underlying antiviral mechanisms of GBPs remain subject of future research.

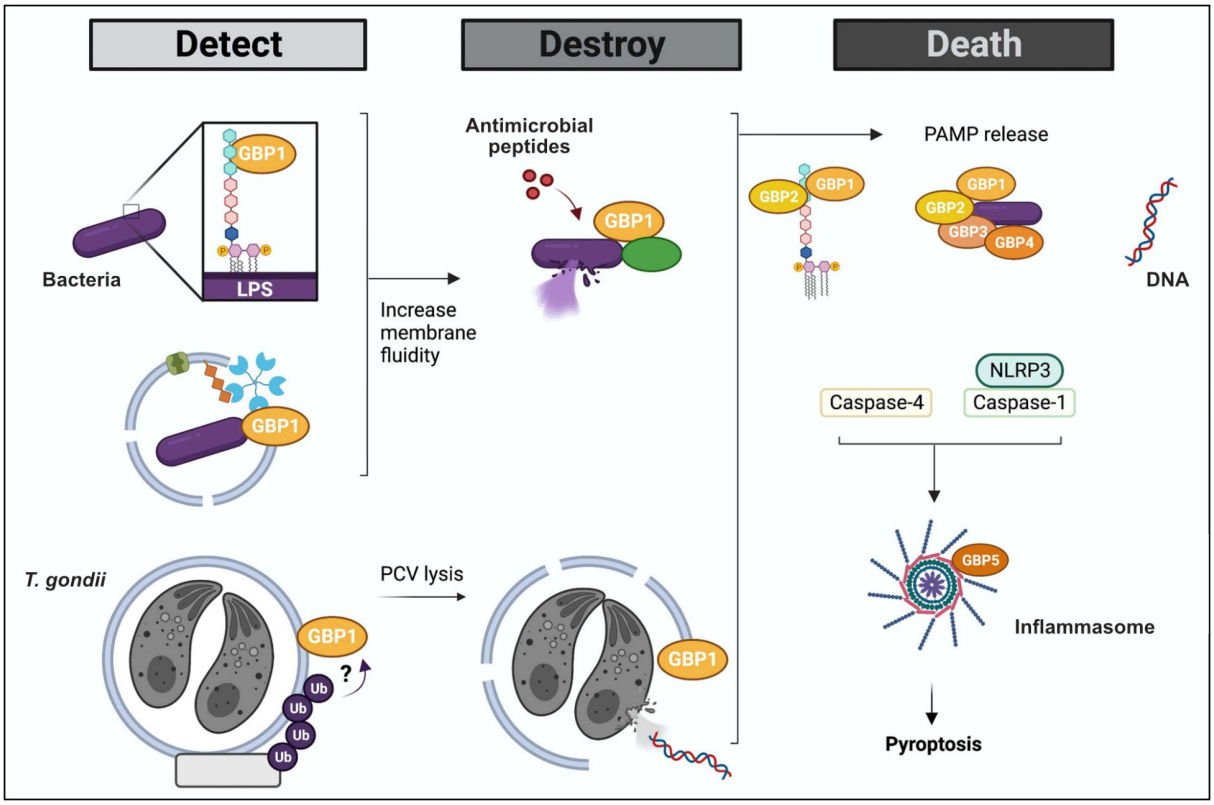

Figure 9. GBP-mediated antibacterial activities. GBPs detect cytosolic bacteria and pathogen-containing vacuoles (PCVs). This leads to an increase in membrane fluidity of intracellular bacteria making them vulnerable to antimicrobial peptides and initiates the rupture of PCVs, both leading to the release of pathogen-associated molecular patterns (PAMPs) and the formation of GBP platforms. Host defense mediated by GBPs ultimately activates inflammatory responses and triggers pyroptotic cell death. Modified from Rivera-Cuevas et al. (2023).

1.3 GBP1 fights off intracellular bacterial pathogens

Host defense against intracellular bacterial pathogens such as *Shigella* and *Salmonella* is orchestrated by GBP1, a cytosolic lipopolysaccharide (LPS) immune sensor and surfactant (Figure 10) (Kutsch et al., 2020; Santos et al., 2020; Zhu et al., 2024). As mentioned earlier, infections with gram-negative bacteria trigger caspase-4-dependent pyroptosis. Caspase-4 is an innate immune receptor for intracellular lipopolysaccharide (LPS) and becomes activated upon direct interaction with the lipid A domain of LPS via its caspase activation and recruitment domain (CARD) (Shi et al., 2014). GBP1 boosts the release of LPS from intracellular bacteria into the host cell cytosol (Goers et al., 2023). Polymerized GBP1 and GBP2 cluster and aggregate cytosolic LPS to form GBP-LPS hubs for non-canonical inflammasome activation (Dickinson et al., 2023; Kutsch et al., 2020).

GBP1 polymerization is not only required for accelerating caspase-4 activation, but also for establishing an antimicrobial microcapsule or coatomer on the surface of intracellular gram-negative bacteria (Figure 10). In this process, soluble GBP1 polymers bind to membrane attached LPS of the bacterial pathogen and rearrange into a stable protein coat encapsulating the bacterial cell. The membrane-bound GBP1 coat acts as surfactant disrupting the protective O-antigen layer of the outer membrane of gram-negative bacteria (Kutsch et al., 2020). By breaking down the integrity of the bacterial envelope, the lipid A domain of LPS becomes unmasked and accessible. As shown by Kutsch et al. (2020), GBP1-encapsulated bacteria are vulnerable to cationic antimicrobial peptides (CAMPs). Polymyxin B, for example, increases the permeability of the outer membrane and triggers bacteriolysis by interacting with the negatively charged phosphates groups of the inner core of LPS and lipid A (Acikalin et al., 2017; Moffatt et al., 2019). The O-antigen layer conveys protection against such interactions but GBP1-mediated permeabilization of the O-antigen layer cancels out its protective function (Kutsch et al., 2020). Simultaneously, permeabilization of the O-antigen layer increases the outer membrane fluidity which has been shown to block actin tail formation and to inhibit actin-based bacterial dissemination of cytosolic *S. flexneri* (Kutsch et al., 2020; Piro et al., 2017; Wandel et al., 2017).

By encapsulating bacteria, GBP1 not only causes the breakdown of the LPS barrier but also recruits other GBP paralogs and components of the inflammasome pathway to the bacterial surface which are proposed to form a platform for caspase-4 activation (Figure 10) (Santos et al., 2020; Wandel et al., 2020; Zhu et al., 2024). In contrast, Dickinson et al. (2023)

demonstrated that GBP1 coatomer formation is dispensable for acceleration of caspase-4 activation, raising the question of what function the GBP1-mediated caspase-4 recruitment to intracellular bacteria actually has. Although it is known that caspase-4 requires GBP2 and GBP5 for being recruited to the bacterial surface in HeLa cells and that GBP3 promotes caspase-4 activation (Santos et al., 2020; Wandel et al., 2020), mechanistic understanding of the hierarchical GBP network is elusive. These are just two of many unanswered questions to fully understand GBP-driven immunity. Disregarding the exact underlying molecular framework of GBP1-mediated host defense, GBP1 polymerization and coatomer formation are prerequisite for any of its antimicrobial function. This emphasizes the significant role of GBP1 oligomerization in innate immune responses and highlights the importance of having a detailed mechanistic understanding of its assembly process.

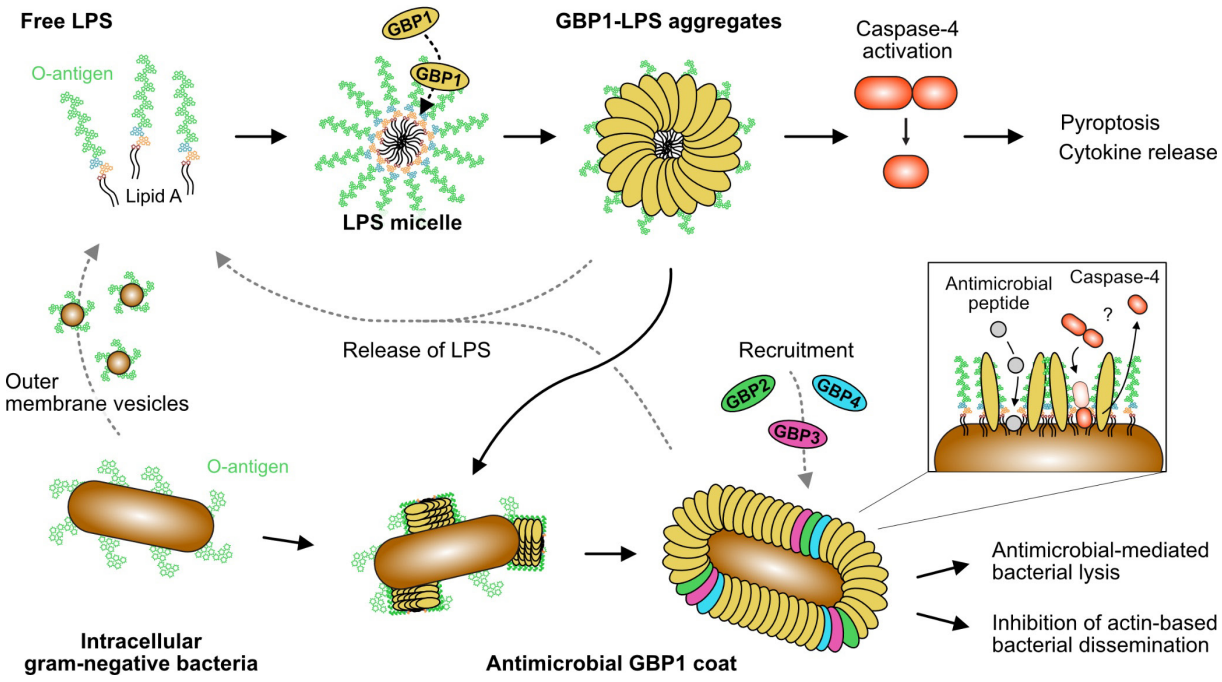

Figure 10. GBP1 oligomerization as key to cell autonomous immunity against intracellular bacterial pathogens. GBP1 oligomerization is mediated through lipopolysaccharide (LPS). GBP1-LPS hubs provide a platform for caspase-4 activation leading to pyroptosis and cytokine release. Polymeric GBP1 is required for encapsulating gram-negative bacteria in an antimicrobial GBP1 coat, thus recruiting GBP paralogs to bacterial pathogens. The GBP1 coat breaks down the integrity of the bacterial envelope, thereby 1) enhancing antimicrobial peptide activity and promoting bacterial lysis, 2) blocking actin-driven dissemination, and 3) unmasking lipid A, and, possibly, recruiting and activating caspase-4.

2 Scope of the thesis

GBP1-driven immunity against microbial pathogens has been the subject of intense research in recent decades. However, mechanistic details of the GBP1 oligomerization process have remained unclear. GBP1 is a key player in mediating host defense against intracellular bacteria such as *Shigella* and *Salmonella*. In infected cells, GBP1 assembles into soluble polymers and establishes a dense protein coat or coatomer encapsulating bacterial invaders. While GBP1 polymers promote caspase-4-dependent pyroptosis by accelerating noncanonical inflammasome activation, the GBP1 coatomer breaks down the integrity of the bacterial envelope.

Many recent studies have aimed to understand the cellular mode of action of GBP1 following infection. However, it is equally important to understand the detailed mechanism of assembly at the structural level that precedes any cellular function. Our structural knowledge of its assembly to date is limited to the insights we have gained from several monomeric and dimeric crystal structures in different nucleotide states and from initial low-resolution data on its polymeric state. Extensive biophysical studies have addressed determinants for GBP1 assembly and contributed to the structural characterization of its oligomeric states. Nevertheless, questions remain about the architecture and the interface of GBP1 within the oligomer and as to how nucleotide-dependent conformational changes facilitate assembly.

The scope of this thesis is to characterize GBP1 oligomerization structurally and biochemically to develop a model of its activation mechanism. To this end, medium-resolution structures of membrane-bound GBP1 to a simple membrane model system and soluble GBP1 polymers were obtained by cryo-electron microscopy. By combining these new and already known structural data, structure-guided mutants of the oligomeric interface and of an identified conformational rearrangement upon nucleotide hydrolysis were generated and biochemically analyzed. The physiological role of these mutants in establishing the GBP1 coatomer was tested in an *in vitro* binding assay to gram-negative pathogenic bacteria.

3 Materials and Methods

3.1 Materials

3.1.1 Instruments

Agarose Gel Electrophoresis System	Biometra, Göttingen, DE
ÄKTA Pure Protein Purification System	Cytiva, Marlborough, MA, US
Benchtop Centrifuge 5415 R	Eppendorf, Hamburg, DE
Centrifuge Avanti J-26 XP	Beckman Coulter, Krefeld, DE
Chromatography columns:	
HiLoad Superdex 200 16/600	GE Healthcare, Chicago, IL, US
Superdex 200 Increase 5/150 GL	GE Healthcare, Chicago, IL, US
HiTrap Butyl HP	GE Healthcare, Chicago, IL, US
Eppendorf Research plus pipettes	Eppendorf, Hamburg, DE
Glow discharger GloQube Plus	Quorum Technologies, Lewes, UK
HPLC 1200 LC System	Agilent Technologies, Santa Clara, CA, US
HPLC reversed-phase Hypersil ODS C18 100 x 4.6 (5 µm) column	Thermo Fisher Scientific, Waltham, MA, US
Microplate Readers:	
Infinite 200	Tecan, Männedorf, CH
Spark	Tecan, Männedorf, CH
Mini Extruder	Avanti Polar Lipids, Alabaster, US
Peristaltic Pump Reglo Analog ISM827B	Ismatec, Glattbrugg, CH
pH-Meter	Mettler-Toledo, Gießen, DE
Photometer BioPhotometer	Eppendorf, Hamburg, DE
Photometer NanoDrop 2000	Thermo Fisher Scientific, Waltham, MA, US
Plunge freezer Vitrobot Mark IV	FEI, Hillsboro, OR, US
Scales	Sartorius, Göttingen, DE
SDS-PAGE System XCell SureLock Mini-Cell	Thermo Fisher Scientific, Waltham, MA, US
Spectropolarimeter J-720	JASCO Corporation, Tokyo, JP
Thermocycler C1000 Touch	Bio-Rad, Hercules, CA, US
Transmission electron microscopes:	
Talos L120C	Thermo Fisher Scientific, Waltham, MA, US
Titan Krios G3i	Thermo Fisher Scientific, Waltham, MA, US
Ultracentrifuge Optima MAX-XP	Beckman Coulter, Krefeld, DE
Ultrasonic homogenizer SONOPLUS HD 2070	Bandelin Electronic, Berlin, DE

3.1.2 Chemicals

1,2-dioleoyl-sn-glycero-3-phospho-L-serine (18:1 DOPS)	Avanti Polar Lipids, Alabaster, US
1,2-dioleoyl-sn-glycero-3-phospho-(1'-myo-inositol-4',5'-bisphosphate) (18:1 PI(4,5)P_2)	Avanti Polar Lipids, Alabaster, US
1,2-dipalmitoyl-sn-glycero-3-phospho-ethanolamine N-(lissamine rhodamine B sulfonyl) (16:0 Liss Rhod PE)	Avanti Polar Lipids, Alabaster, US
2'/3'-O-(N-Methyl-anthraniloyl)-guanosine-5'-[(β,γ)-imido]triphosphate (mant-GMPPNP)	Jena Biosciences, Jena, DE
2'/3'-O-(N-Methyl-anthraniloyl)-guanosine-5'-diphosphate (mant-GDP)	Jena Biosciences, Jena, DE
4-(2-Hydroxyethyl)piperazine-1-ethanesulfonic acid (HEPES)	Carl Roth, Karlsruhe, DE
Acetic acid	Carl Roth, Karlsruhe, DE
Acetone	Carl Roth, Karlsruhe, DE
Acetonitrile	Carl Roth, Karlsruhe, DE
Agar-agar	Carl Roth, Karlsruhe, DE
AlexaFluor488-C5-maleimide	Thermo Fisher Scientific, Waltham, MA, US
AlexaFluor647-C2-maleimide	Thermo Fisher Scientific, Waltham, MA, US
Aluminum chloride	Sigma-Aldrich, Steinheim, DE
Ammonium sulfate	Carl Roth, Karlsruhe, DE
Ampicillin sodium salt	Carl Roth, Karlsruhe, DE
Bis(sulfosuccinimidyl)suberate (BS3)	Thermo Fisher Scientific, Waltham, MA, US
Brain Polar Lipid Extract (Porcine)	Avanti Polar Lipids, Alabaster, US
Carbenicillin disodium salt	Carl Roth, Karlsruhe, DE
Chloroform	Carl Roth, Karlsruhe, DE
Cholesterol	Avanti Polar Lipids, Alabaster, US
Coomassie brilliant blue R250	Carl Roth, Karlsruhe, DE
Dimethyl sulfoxide (DMSO)	Carl Roth, Karlsruhe, DE
Dithiothreitol (DTT)	Carl Roth, Karlsruhe, DE
Ethanol	Carl Roth, Karlsruhe, DE
Ethidiumbromid	Carl Roth, Karlsruhe, DE
Ethylenediaminetetraacetic acid (EDTA)	Carl Roth, Karlsruhe, DE
Farnesyl pyrophosphate (FPP)	Cayman Chemical, Ann Arbor, MI, US
Folch fraction I bovine brain lipids	Sigma-Aldrich, Steinheim, DE
Guanosine-5'-[(β,γ)-imido]triphosphate (GMPPNP)	Jena Biosciences, Jena, DE
Guanosine-5'-(γ-thio)-triphosphate (GTPγS)	Jena Biosciences, Jena, DE
Guanosine diphosphate (GDP)	Jena Biosciences, Jena, DE

Guanosine monophosphate (GMP)	Jena Biosciences, Jena, DE
Guanosine triphosphate (GTP)	Jena Biosciences, Jena, DE
Glycerol	Carl Roth, Karlsruhe, DE
Hydrochloric acid	Carl Roth, Karlsruhe, DE
Imidazole	Carl Roth, Karlsruhe, DE
Isopropanol	Carl Roth, Karlsruhe, DE
Isopropyl β-D-1-thiogalactopyranoside (IPTG)	Carl Roth, Karlsruhe, DE
Kanamycin sulfate	Carl Roth, Karlsruhe, DE
Lipopolysaccharides from *E. coli* O55:B5 (LPS-O55:B5)	Invivogen, San Diego, CA, US
Magnesium chloride hexahydrate	Sigma-Aldrich, Steinheim, DE
Methanol	Carl Roth, Karlsruhe, DE
Phenylmethylsulfonylfluoride (PMSF)	Carl Roth, Karlsruhe, DE
Sodium chloride	Carl Roth, Karlsruhe, DE
Sodium dodecyl sulfate (SDS)	Carl Roth, Karlsruhe, DE
Sodium fluoride	Carl Roth, Karlsruhe, DE
Sodium hydroxide	Carl Roth, Karlsruhe, DE
Tetrabutylammonium bromide (TBAB)	Sigma-Aldrich, Steinheim, DE
Tris(hydroxymethyl)aminomethane hydrochloride (Tris-HCl)	Carl Roth, Karlsruhe, DE
Uranyl acetate dihydrate	Merck, Darmstadt, DE

3.1.3 Enzymes and other reagents

2-Log DNA Ladder	NEB, Frankfurt a.M., DE
DNase I	NEB, Frankfurt a.M., DE
Restriction Endonucleases	NEB, Frankfurt a.M., DE
T4 DNA Ligase	NEB, Frankfurt a.M., DE
T4 Polynucleotide kinase	NEB, Frankfurt a.M., DE
Unstained Protein Molecular Weight Marker	Fermentas, St. Leon-Rot, DE

3.1.4 Equipment and consumables

Amicon Ultra Centrifugal Filters	Merck, Darmstadt, DE
Carbon-coated Cu300 grids	Quantifoil Micro Tools, Großlöbichau, DE
Colloidal gold beads (5 and 10 nm)	Sigma-Aldrich, Steinheim, DE
Corning 96-well Black Flat Bottom Polystyrene NBS Microplate	Corning, Corning, NY, US
Macro cell quartz glass HighPerformance, 0.1 cm	Hellma, Müllheim, DE
Ni Sepharose HP	Cytiva Sweden, Uppsala, SWE
Nunc MicroWell 96-well polystyrene plates	Sigma-Aldrich, Steinheim, DE
NuPAGE MES SDS Buffer (20X)	Thermo Fisher Scientific, Waltham, MA, US

NuPAGE MOPS SDS Buffer (20X)	Thermo Fisher Scientific, Waltham, MA, US
NuPAGE Novex 4-12% Bis-Tris	Thermo Fisher Scientific, Waltham, MA, US
QUANTIFOIL Cu300 R 1.2/1.3	Quantifoil Micro Tools, Großlöbichau, DE
UltrAuFoil Au200 R 2/2	Quantifoil Micro Tools, Großlöbichau, DE
Whatman membrane filters	Sigma-Aldrich, Steinheim, DE

3.1.5 Kits

KOD Hot Start polymerase Kit	Merck, Darmstadt, DE
innuPREP Plasmid Mini Kit 2.0	Analytik Jena, Jena, DE

3.1.6 Bacteria strains

Table 1. List of bacteria strains used in this thesis.

Bacteria strain	Genotype
E. coli BL21 (DE3)[§]	F^- *ompT* *hsd*S_B (r_B^-, m_B^-) *gal dcm* (DE3)
E. coli DH5α[§]	F^- φ80*lac*ZΔM15 Δ(*lac*ZYA-*arg*F)U169 *rec*A1 *end*A1 *hsd*R17(r_K^-, m_K^+) *pho*A *sup*E44 λ^- *thi*-1 *gyr*A96 *rel*A1

[§] Novagen, Merck, Darmstadt, DE

3.1.7 Plasmids

Table 2. List of plasmids used in this thesis for bacterial expression (pQE-80L) and co-expression (pRSFDuet-1). MCS: multiple cloning site.

Plasmid	Size	Promotor	Affinity tag	Repression module	Resistance
pQE-80L[§]	4,751 bp	T5	**MCS1**: N-term MRGS-6xHis	lacIq	ampicillin
pRSFDuet-1[†]	3,829 bp	T7	**MCS1**: N-term MGSS-6xHis **MCS2**: C-term S-tag	lacI	kanamycin

[§] Qiagen, Hilden, DE

[†] Novagen, Merck, Darmstadt, DE

3.1.8 Media and buffers

Lysogeny Broth (LB)	10 g/l	Tryptone
	5 g/l	Yeast extract
	10 g/l	NaCl
	pH adjusted to 7.0 with NaOH	
LB Agar plates	15 g/l	Agar-agar
	in Lysogeny Broth (LB)	
Terrific Broth (TB)	ordered from Carl Roth, Karlsruhe, DE	
Lysis buffer A	50 mM	Tris-HCl pH 7.9
	500 mM	NaCl
	5 mM	$MgCl_2$
	10 %	Glycerol
Lysis buffer B	50 mM	Tris-HCl pH 7.9
	500 mM	NaCl
	5 mM	$MgCl_2$
Ni-NTA wash buffer	50 mM	Tris-HCl pH 7.9
	150 mM	NaCl
	5 mM	$MgCl_2$
	10 mM	Imidazole
Ni-NTA elution buffer	50 mM	Tris-HCl pH 7.9
	150 mM	NaCl
	5 mM	$MgCl_2$
	150 mM	Imidazole
HIC buffer A	50 mM	Tris-HCl pH 7.9
	5 mM	$MgCl_2$
	2 mM	DTT
HIC buffer B	50 mM	Tris-HCl pH 7.9
	5 mM	$MgCl_2$
	1.2 M	$(NH_4)_2SO_4$
	2 mM	DTT
SEC buffer / Storage buffer	50 mM	Tris-HCl pH 7.9
	150 mM	NaCl
	5 mM	$MgCl_2$
	2 mM	DTT
Assay buffer A	50 mM	Tris-HCl pH 7.9
	150 mM	NaCl
	5 mM	$MgCl_2$
Assay buffer B	50 mM	HEPES pH 7.9
	150 mM	NaCl
	5 mM	$MgCl_2$

HPLC buffer	100 mM	Potassium phosphate buffer pH 6.5
	10 mM	Tetrabutylammonium bromide (TBAB)
	7.5% (v/v)	Acetonitrile
Farnesylation buffer	50 mM	Tris-HCl pH 7.9
	150 mM	NaCl
	5 mM	$MgCl_2$
	10 µM	$ZnCl_2$
SDS-PAGE sample buffer, 4x	250 mM	Tris-HCl pH 8.5
	100 mM	DTT
	1.6 mM	EDTA
	8 % (w/v)	SDS
	40 % (v/v)	Glycerol
	0.01 % (w/v)	Bromphenol blue
SDS-PAGE sample buffer, 5x	300 mM	Tris-HCl pH 8.5
	125 mM	DTT
	2 mM	EDTA
	10 % (w/v)	SDS
	50 % (v/v)	Glycerol
	0.01 % (w/v)	Bromphenol blue

3.1.9 Software

AlphaFold2	Jumper et al. (2021); Mirdita et al. (2022)
CDNN 2.1	Bohm et al. (1992)
CTFFIND4	Rohou and Grigorieff (2015)
Chimera v.1.16	Pettersen et al. (2004); UCSF Resource for Biocomputing, Visualization, and Informatics
ChimeraX v.1.5	Meng et al. (2023), UCSF Resource for Biocomputing, Visualization, and Informatics
Dynamo	Castano-Diez et al. (2012)
ESPript v3.0	Robert and Gouet (2014)
GCTF	Zhang (2016)
ImageJ v.1.53t	Schneider et al. (2012)
IMOD v.4.11	Kremer et al. (1996)
MotionCor2	Zheng et al. (2017)
OriginPro 2021b	OriginLab Corporation, Northampton, MA, US
Relion4.0	Kimanius et al. (2021)
SerialEM	Mastronarde (2005)
SWISS-MODEL	Waterhouse et al. (2018)
TomoBEAR	Balyschew et al. (2023)

3.1.10 Protein structures and EM maps

Table 3. List of protein structures displayed in this thesis.

Protein	PDB	Nucleotide state	Species	Method	Resolution	Reference
GBP1	1dg3	apo	Homo sapiens	X-ray diffraction	1.8 Å	Prakash et al. (2000a)
	2d4h	GMP	Homo sapiens	X-ray diffraction	2.9 Å	Ghosh et al. (2006)
	2b8w	GMP•AlF_x	Homo sapiens	X-ray diffraction	2.2 Å	Ghosh et al. (2006)
	2b92	GDP•AlF_x	Homo sapiens	X-ray diffraction	3.2 Å	Ghosh et al. (2006)
	2bc9	GMPPNP	Homo sapiens	X-ray diffraction	2.8 Å	Ghosh et al. (2006)
	8r1a	GDP•AlF_x	Homo sapiens	Electron microscopy	26.8 Å	This thesis, Weismehl et al. (2024)
GBP1: 14-3-3σ	8q4l	apo	Homo sapiens	Electron microscopy	5.1 Å	Fisch et al. (2023)
GBP5	7e5a	GDP•AlF_x	Homo sapiens	X-ray diffraction	2.5 Å	Cui et al. (2021)
Atlastin	3q5e	GDP	Homo sapiens	X-ray diffraction	3.0 Å	Byrnes and Sondermann (2011)
	4idp	GMPPNP	Homo sapiens	X-ray diffraction	2.6 Å	Byrnes et al. (2013)
Dynamin	5d3q	GDP	Homo sapiens	X-ray diffraction	1.7 Å	Anand et al. (2016)
	3zyc	GMPPNP	Homo sapiens	X-ray diffraction	2.2 Å	Chappie et al. (2011)

Table 4. List of EM maps displayed in this thesis. STA: subtomogram averaging, SPA: single particle analysis.

Protein	EMDB	Nucleotide state	Species	Method	Resolution	Reference
GBP1	18806	GDP•AlF_x	Homo sapiens	STA	26.8 Å	This thesis, Weismehl et al. (2024)
	18698	GDP•AlF_x	Homo sapiens	SPA	37.0 Å	This thesis, Weismehl et al. (2024)
	43091	GTP	Homo sapiens	STA	17.0 Å	Zhu et al. (2024)
	43153	GTP	Homo sapiens	STA	9.7 Å	Zhu et al. (2024)

3.2 Molecular Biology

3.2.1 Transformation of chemically competent *E. coli* cells

Chemically competent *Escherichia coli* bacteria were prepared according to Chung et al. (1989). Plasmids were transformed using the heat shock method according to standard procedures (Green and Sambrook, 2012). *E. coli* DH5α and BL21 (DE3) strains were used for plasmid propagation and protein expression, respectively.

3.2.2 Site-directed mutagenesis

Site-directed mutagenesis of double-stranded plasmid DNA was carried out either by QuikChange mutagenesis (Agilent Technologies) or by a non-overlapping primer approach (NEB) according to the manufacturer's instructions with the following adaptations: KOD Hot Start polymerase was used as DNA polymerase for both approaches and T4 Polynucleotide kinase, T4 DNA Ligase, and DpnI restriction endonuclease were used instead of the KLD Enzyme Mix (NEB) according to manufacturer's protocols and standard procedures (Green and Sambrook, 2012). For primer design, the QuikChange Primer Design tool (Agilent Technologies) and the NEBaseChanger tool (NEB) were used, respectively. Oligonucleotides used in this thesis are listed in Appendix A.

3.2.3 Isolation of plasmid DNA

Plasmid DNA was isolated from bacterial lysates using innuPREP Plasmid Mini Kit 2.0 (Analytik Jena) according to the manufacturer's instruction.

3.2.4 DNA sequencing

DNA sequencing was done by LGC Genomics (Berlin) using the Sanger sequencing method and the sequencing primers pQE-80L_fw (5'-CGGAT AACAA TTTCA CACAG-3') and pQE-80L_rv (3'-GGTCA TTACT GGAGT CTTG-5'). Sequencing results were analyzed using Clustal Omega (Sievers et al., 2011).

3.2.5 Expression constructs

Human GBP1 constructs were generated by QuikChange mutagenesis (point mutations D199A, D199K, M139D, M139E, and M139R) and a non-overlapping primer approach (Δ207-213, Δ207-216, and Δ207-223) using the pQE-80L-GBP1 plasmid; a kind gift from Dr. Gerrit Praefcke (G.P.). The natural variant A409G (VAR_046550) of human GBP1

(UniProtID: P32455) was used in this study. All constructs used are listed in Table 5. Human GBP1 constructs comprise an uncleavable N-terminal MRGS-His_6-tag; the human farnesyltransferase (FTase) subunit A (in multiple cloning site 1) an uncleavable N-terminal MGSS-His_6-tag.

Table 5. Expression constructs. G.P.: construct has been provided by Dr. Gerit Praefcke.

Construct	Remarks	Vector
GBP1 WT	full-length wild-type; provided by G.P.	pQE-80L
GBP1 Q577C	C-terminal Cys mutant, from Sistemich and Herrmann (2020)	pQE-80L
GBP1 Δ207-213	helix α4' variant (Gly-Ser substitution)	pQE-80L
GBP1 Δ207-216	helix α4' variant (Gly-Ser substitution)	pQE-80L
GBP1 Δ207-223	helix α4' variant (Gly-Ser substitution)	pQE-80L
GBP1 M139D	helix α3-α4' mutant	pQE-80L
GBP1 M139E	helix α3-α4' mutant	pQE-80L
GBP1 M139R	helix α3-α4' mutant	pQE-80L
GBP1 D199A	pivot point mutant	pQE-80L
GBP1 D199K	pivot point mutant	pQE-80L
GBP1 RK(227-228)EE	from Vopel et al. (2010)	pQE-80L
LG-WT	isolated Large GTPase (LG) domain of GBP1	pQE-80L
LG-Δ207-213	isolated Large GTPase (LG) domain of GBP1, helix α4' variant (Gly-Ser substitution)	pQE-80L
LG-Δ207-216	isolated Large GTPase (LG) domain of GBP1, helix α4' variant (Gly-Ser substitution)	pQE-80L
LG-Δ207-223	isolated Large GTPase (LG) domain of GBP1, helix α4' variant (Gly-Ser substitution)	pQE-80L
FTase	provided by G.P.	pRSFDuet-1

3.3 Biochemistry

3.3.1 Protein expression and purification

The expression and purification protocols described below are modified from Sistemich and Herrmann (2020).

3.3.1.1 Protein over-expression in *E. coli*

Wild-type GBP1 and all constructs generated by site-directed mutagenesis (see 3.2.2 and 3.2.5) were expressed from pQE-80L vector as N-terminal His_6-tag fusions in *E. coli* BL21 (DE3). For *in vivo* farnesylation, GBP1 constructs were co-expressed with N-terminal His_6-tagged farnesyltransferase (FTase) from pRSFDuet-1. Following bacterial transformation by heat shock, cells were plated on LB agar plates containing 100 µg/ml ampicillin or, in case of co-expression with pRSFDuet-1-FTase, 50 µg/ml kanamycin and 100 µg/ml ampicillin and incubated at 37 °C for 16-20 h. Expression cultures of 1 l TB-medium supplemented with respective antibiotics were 1:50 inoculated with a pre-inoculum in LB-medium containing the expression constructs and incubated at 37 °C and 90 rpm. Protein expression was induced by addition of 100 µM IPTG at an optical density at 600 nm ($OD_{600\,nm}$) of 0.8 absorbance units (AU). Expression cultures were grown for another 16-18 h at 20 °C. Cells were harvested by centrifugation at 4 °C and 4,000 rpm for 20 min in a JLA-8.1000 rotor. Cell pellets were either used directly for protein purification or transferred into a 50 ml falcon tube and stored at -20 °C.

3.3.1.2 Preparation of cell lysates from *E. coli*

Cell pellets were resuspended in 50 ml lysis buffer A supplemented with 10 µM DNase I and 300 µM PMSF. Resuspended cells were lysed by sonication for 2-times 2 min on ice with an amplitude of 60% and a pulse on/off time of 0.5 s. The cell suspension was then centrifuged at 4 °C and 18,000 rpm for 45 min in a JA 25.50 rotor.

3.3.1.3 Purification of non-farnesylated GBP1 constructs

Purification of non-farnesylated GBP1 constructs were performed at 4 °C. Cell lysates were subjected to immobilized metal affinity chromatography (IMAC) on a gravity flow column loaded with 2 ml Ni Sepharose HP resin. After equilibrating the column with 10 CVs lysis buffer B (lysis buffer A without glycerol) and loading the lysate, the column was washed with 5 CVs Ni-NTA wash buffer (containing 10 mM imidazole) and His-tagged protein was eluted with 5-10 CVs Ni-NTA elution buffer (containing 150 mM imidazole). Eluted protein was concentrated using a 10 kDa cut-off centrifugal filter and subjected to size exclusion

chromatography using a HiLoad 16/600 Superdex 200 prep grade column (GE Healthcare) equilibrated in SEC buffer. After SDS-PAGE analysis, GBP1 protein containing fractions were combined and concentrated using a 10 kDa cut-off centrifugal filter. The protein concentration was determined by the Lambert-Beer law. Protein samples were flash frozen in liquid nitrogen and stored at -70 °C.

3.3.1.4 Purification of farnesylated GBP1 constructs

For biochemical studies, farnesylated GBP1 constructs were purified similar to the non-farnesylated constructs (see 3.3.1.3). Cell lysates containing the co-expressed N-terminal His_6-tagged FTase were subjected to IMAC using Ni Sepharose HP resin. Following IMAC, eluted protein was concentrated using a 10 kDa cut-off centrifugal filter and buffer exchanged to HIC buffer B (containing 1.2 M $(NH_4)_2SO_4$). Farnesylated GBP1 was separated from unmodified protein and FTase by hydrophobic interaction chromatography (HIC) using a Butyl Sepharose HP (GE Healthcare) column in a step-wise decreasing salt gradient from 1.2 M $(NH_4)_2SO_4$ (HIC buffer B) to 0 M $(NH_4)_2SO_4$ (HIC buffer A) according to Sistemich and Herrmann (2020). Fractions containing farnesylated GBP1 were pooled, concentrated using a 10 kDa cut-off centrifugal filter, and subjected to size exclusion chromatography as performed for non-farnesylated GBP1.

For structural studies, *in vitro* farnesylated GBP1 was prepared by Dr. Paul Lauterjung (Ruhr-University Bochum). Non-farnesylated GBP1 was purified as described in 3.3.1.3 and farnesylation by enzymatic modification was performed using 60 µM GBP1, 1.25 µM self-prepared FTase, and 150 µM farnesyl pyrophosphate (FPP) in Farnesylation buffer in a glass vial at 4 °C overnight. FTase was purified according to Dickinson et al. (2023). Farnesylated and non-farnesylated GBP1 were separated by hydrophobic interaction chromatography (Butyl Sepharose HP, GE Healthcare), followed by a second size exclusion chromatography run in SEC buffer according to Dickinson et al. (2023).

3.3.1.5 Sodium dodecyl sulfate-polyacrylamide gel electrophoresis

Denaturing sodium dodecyl sulfate-polyacrylamide gel electrophoresis (SDS-PAGE) was used to separate and analyze proteins by molecular mass according to Laemmli (1970). Protein samples were prepared in 1x SDS-PAGE sample buffer and heated 5 min at 95 °C. Unstained Protein Molecular Weight Marker (Fermentas), 14 to 116 kDa, was loaded as reference. NuPAGE 4-12% Bis-Tris protein gels (Invitrogen) were used for electrophoresis in 1x MES or MOPS running buffer (Invitrogen). Gels were stained with Coomassie Brilliant Blue

staining solution (45% (v/v) ethanol, 10% (v/v) acetic acid, 0.3% (w/v) Coomassie Brilliant Blue R-250) and destained in MQ water.

3.3.1.6 Determination of protein concentration

Protein concentration was determined by Lambert-Beer law using the protein absorption measured at 280 nm ($A_{280\,nm}$) in a NanoDrop 2000 spectrophotometer with d = 1 cm (NanoDrop Technologies) and the molar extinction coefficient of the protein at 280 nm ($\varepsilon_{280\,nm}$). Using the ProtParam tool (Wilkins et al., 1999), $\varepsilon_{280\,nm}$ values of 45,840 $M^{-1}cm^{-1}$ for full-length GBP1 and 35,410 $M^{-1}cm^{-1}$ for the isolated LG domain (both including the N-terminal His_6-tag) were determined and used for calculations by the Lambert-Beer law:

$$c_{protein}[M] = \frac{A_{280\,nm}}{\varepsilon_{280\,nm} \times d} \qquad (eq.\,3.1)$$

3.3.2 Protein labeling with fluorescent probes

For FRET studies, the purified cysteine mutant Q577C was used to label GBP1 at its C-terminus with thiol-reactive AlexaFluor488-C5-maleimide dye (AF488, Thermo Fisher Scientific). For *in vitro* binding assays, GBP1 wild-type and mutants were labeled with AlexaFluor647-C2-maleimide dye (AF647, Thermo Fisher Scientific). Maleimide-conjugated dyes readily react with sulfhydryl groups and form a chemically stable thio-ether bond between the dye and cysteines of the protein. Labelling of GBP1-AF647 constructs was performed by Dr. Miriam Kutsch (Heinrich Heine University Düsseldorf).

As described by Sistemich and Herrmann (2020), DTT was removed from purified protein by ultrafiltration and buffer exchange to Assay buffer A. Labeling was performed at an equimolar ratio of protein and dye on ice for 10 min in order to minimize labeling of intrinsic cysteines. The labeling reaction was stopped by the addition of 2 mM DTT and unreacted dye was removed by ultrafiltration and buffer exchange to Assay buffer A. The concentration of bound dye was determined by the Lambert-Beer law using the dye absorption (A_{max}) measured at the absorption maximum (λ_{abs}) for each dye:

$$c_{dye}[M] = \frac{A_{max}}{\varepsilon_{max} \times d} \qquad (eq.\,3.2)$$

where ε_{max} is the extinction coefficient of the dye at the absorption maximum (see Table 6).

Table 6. Properties of maleimide-conjugated Alexa Fluor (AF) dyes. Data derived from Invitrogen.

Dye	MW (Da)	λ_{abs} [§] (nm)	λ_{em} [†] (nm)	ε_{max} (M^{-1} cm^{-1}) [‡]	$CF_{280\ nm}$ [*]
AF488	~721	491	516	71,000	0.11
AF647	~1250	651	671	268,000	0.03

§ longest-wavelength absorption maximum
† fluorescence maximum
‡ molar extinction coefficient at the longest-wavelength absorption maximum
* correction factor ($CF_{280\ nm} = \varepsilon_{280\ nm}/\varepsilon_{max}$)

Protein concentrations of AF labeled GBP1-Q577C were corrected for dye contribution using the correction factors $CF_{280\ nm}$ for AF488 and AF647:

$$c_{protein}\ [M] = \frac{A_{280\ nm} - A_{max} \times CF_{280\ nm}}{\varepsilon_{protein} \times d} \quad (eq.\ 3.3)$$

and the degree of labeling (DOL) was determined:

$$DOL = \frac{c_{dye}}{c_{protein}} \quad (eq.\ 3.4)$$

The DOL was typically between 0.9 and 0.95 for GBP1-Q577C-AF488 and 0.1 and 0.15 for the GBP1-AF647 constructs.

3.3.3 Liposome preparation

Lipid stocks were prepared in chloroform or chloroform/methanol (3:1 v/v) and stored at -20 °C. Liposomes were prepared from Porcine brain polar lipids (BPL, Avanti Polar Lipids) or Folch fraction I bovine brain lipids (Folch, Sigma-Aldrich) in glass tubes by drying 40 µl of a 25 mg/ml lipid stock in chloroform under an argon stream. For FRET measurements, lipid mixtures were supplemented with 0.5% (w/w) 1,2-dipalmitoyl-sn-glycero-3-phospho-ethanolamine N-(lissamine rhodamine B sulfonyl) (Liss Rhod PE, Avanti Polar Lipids). If specified, Folch lipids were supplemented with 10% (w/w) 1,2-dioleoyl-sn-glycero-3-phospho-L-serine (18:1 PS (DOPS)), 10% (w/w) 1,2-dioleoyl-sn-glycero-3-phospho-(1'-myo-inositol-4',5'-bisphosphate) (18:1 PI(4,5)P_2), or 25% (w/w) cholesterol (all Avanti Polar Lipids). Residual chloroform was removed under vacuum for 60 min. The homogenous lipid film was rehydrated in 1 ml Assay buffer A to reach a final lipid concentration of 1 mg/ml. Lipid rehydration was performed in a water bath at 55 °C for 60 min, followed by five freeze-thaw cycles. Liposomes were extruded to 0.1 µm filters using a mini extruder (Avanti Polar Lipids).

3.3.4 Liposome co-sedimentation assay

For co-sedimentation assays, 5 µM farnesylated GBP1 was mixed with 0.5 mg/ml extruded liposomes (0.1 µm, see 3.3.3) and the respective nucleotide (2 mM GTP, 500 µM GTPγS, 500 µM GMPPNP, 200 µM GDP•AlF_x, 1 mM GDP) in 40 µl Assay buffer A or Assay buffer A supplemented with 300 µM $AlCl_3$ and 10 mM NaF. Samples were incubated 1 min (GTP), 5 min (GTPγS, GMPPNP) or 10 min (apo, GDP•AlF_x, GDP) at RT. Liposomes were sedimented via ultracentrifugation for 10 min at 70,000 rpm (TLA-100, Beckman) and 20 °C. Supernatants were collected and mixed with 10 µl 5x SDS-PAGE sample buffer. Pellets were incubated with 50 µl 1x SDS-PAGE sample buffer for 30 min and resuspended. Samples were analyzed by SDS-PAGE in MES buffer (see 3.3.1.5) loading 2.0 µg protein per well.

3.3.5 FRET-based liposome binding assay

The FRET-based liposome binding assay was performed with farnesylated GBP1-Q577C-AF488 (donor, D, see 3.3.2) and liposomes supplemented with 0.5% Liss Rhod PE (acceptor, A, see 3.3.3) in Assay buffer A (apo, GTP) or Assay buffer A supplemented with 300 µM $AlCl_3$ and 10 mM NaF (GDP•AlF_x). Liposomes (0.5 mg/ml) and protein (5 µM or 0.5-20 µM) were incubated in the absence or presence of 2 mM GTP and 200 µM GDP•AlF_x, respectively. Measurements were performed in a 96-well black non-binding surface microplate (Corning) in a total volume of 100 µl using a microplate reader (Spark, Tecan). Emission spectra were recorded for $\lambda_{ex,D}$ = 495 nm (7.5 nm bandwidth) before adding nucleotides, and after 1 min (GTP) and 15 min (GDP•AlF_x) of incubation at RT. Spectra were corrected for the contributions from direct A excitation upon D excitation. FRET efficiencies (E) were calculated using the ratio between D and A emission intensities (I_D and I_A) following D excitation at $\lambda_{em,D}$ = 520 nm and $\lambda_{em,A}$ = 590 nm, respectively:

$$E = \frac{I_A}{I_D + I_A} \quad (eq. 3.5)$$

3.3.6 Circular dichroism measurements

GBP1 were dialyzed against 10 mM potassium phosphate pH 7.8, 150 mM NaF and circular dichroism (CD) spectra were recorded from 260 nm to 190 nm (1 nm bandwidth) using a Jasco J-720 spectropolarimeter at 20 °C. Samples were scanned at 2.5 µM protein concentration in quartz cuvettes with a pathlength of 0.1 cm (Hellma), a scanning speed of 100 nm/min, and a data pitch of 0.1 nm. Averages of 10 buffer-subtracted spectra were analyzed in CDNN 2.1 (Bohm et al., 1992) for secondary structure determination.

3.3.7 Polymer crosslinking assay

For crosslinking, all assay reagents and dilutions were prepared in Assay buffer B (comprising HEPES). A buffer exchange of non-farnesylated and farnesylated GBP1 stored in Assay buffer A (comprising Tris-HCl) to Assay buffer B was performed by ultrafiltration using a 10 kDa cut-off centrifugal filter. Crosslinking was carried out in a 96-well plate using 20 µM protein. For each construct, non-farnesylated and farnesylated protein were incubated without any nucleotide (apo) or with 200 µM GDP, 300 µM $AlCl_3$ and 10 mM NaF (GDP•AlF_x) for 15 min at RT. 8 µl of each sample was mixed with 1 µl of a 4 mM stock of the homobifunctional amine-to-amine crosslinker bis(sulfosuccinimidyl)suberate (BS3, Thermo Scientific) in water (20-times molar access). The crosslinking reaction was incubated for 30 min at RT and stopped by adding 1 µl 0.5 M Tris-HCl pH 7.9. After 10 min of incubation, samples were mixed with 2.5 µl 5x SDS sample buffer and analyzed by SDS-PAGE in MOPS buffer (see 3.3.1.5) loading 1.0 µg protein per well.

3.3.8 Light-scattering based polymerization assay

Polymerization of farnesylated GBP1 was monitored by measuring the apparent changes in absorbance as result of changes in light scattering over time using a microplate reader (Infinite 200, Tecan) at a wavelength of 350 nm (9 nm bandwidth). Measurements were performed at a protein concentration of 10 µM (GTP) or 20 µM (GDP•AlF_x) in 100 µl Assay buffer A or Assay buffer A supplemented with 300 µM $AlCl_3$ and 10 mM NaF. If indicated, 0.1 mg/ml to 10 mg/ml lipopolysaccharides from *E. coli* O55:B5 (LPS, Invivogen) were added before initiating polymerization. Baselines were measured over 3 min with intervals of 30 s and polymerization was then initiated by adding 1 mM GTP or 200 µM GDP. The polymerization reactions were measured over 40 min with intervals of 20 s. Signals were corrected for the contribution of protein alone (baseline).

3.3.9 Nucleotide binding assay

Nucleotide binding was analyzed using the non-hydrolysable GTP analogue N-methylanthraniloyl guanosine-5'-[(β,γ)-imido]triphosphate (mant-GMPPNP, Jena Bioscience) or mant-GDP (Jena Biosciences). Varying protein concentrations of non-farnesylated GBP1 or isolated LG domain ranging from 0.02 µM to 40 µM were prepared in a black 96-well microplate in Assay buffer A. After adding 0.5 µM mant-GMPPNP or mant-GDP to each well, fluorescence was excited at λ_{ex} = 355 nm (10 nm bandwidth) and fluorescence emission was detected at λ_{em} = 448 nm (10 nm bandwidth) in a microplate reader (Spark, Tecan).

Fluorescence was corrected for mant-nucleotides only. For each construct, averages of three independent measurements were plotted against the protein concentration. Equilibrium dissociation constants K_d were calculated in OriginPro (OriginLab Corporation) by fitting a quadratic equation to data according to Kunzelmann et al. (2005):

$$F = F_{min} + (F_{max} - F_{min}) \frac{A_0 + B_0 + K_d - \sqrt{(A_0 + B_0 + K_d)^2 - 4A_0B_0}}{2B_0} \quad (eq. 3.6)$$

where F_{min} and F_{max} denote the minimal and maximal fluorescence intensities, A_0 the increasing total protein concentration, and B_0 the constant mant-nucleotide concentration.

3.3.10 Nucleotide hydrolysis assay

The catalytic GTPase activity of non-farnesylated GBP1 and the catalytic GDPase activity of isolated LG domains were analyzed by mixing varying protein concentrations with 1 mM GTP or GDP at 37 °C in Assay buffer A. Aliquots of 2 µl were taken at defined time points, diluted 1:15 in HPLC buffer, heat-inactivated at 80 °C for 1 min, and either analyzed directly or stored at -20 °C. All reactions were performed in duplicates, end product formation was performed in triplicates. Nucleotides were separated by reversed-phase HPLC (Hypersil ODS C18, Thermo Fisher) and nucleotide composition was analyzed by integration of the nucleotide absorbance at 254 nm. Initial rates of GTP or GDP hydrolysis were obtained from linear regression. Specific activities were calculated by dividing the initial rates by protein concentration. Apparent K_d values for dimer formation and maximum catalytic activities (k_{max}) were calculated in OriginPro (OriginLab Corporation) by fitting a quadratic equation to data according Praefcke et al. (1999):

$$specific\ activity = k_{max} \frac{A_0 + \frac{K_d}{2} - \sqrt{(A_0 + \frac{K_d}{2})^2 - {A_0}^2}}{A_0} \quad (eq. 3.7)$$

3.3.11 Analytical size-exclusion chromatography

Dimer formation of non-farnesylated GBP1 and isolated LG domains were analyzed by analytical size-exclusion chromatography (Superdex 200 5/150, GE Healthcare) as described by Ince et al. (2017). Samples of 20 µM protein without nucleotide (apo) and with the addition of 200 µM GDP or GMP, 300 µM $AlCl_3$ and 10 mM NaF (GDP•AlF_x or GMP•AlF_x) were incubated at RT for at least 10 min before subjecting to analytical size-exclusion chromatography in Assay buffer A.

3.3.12 *In vitro* binding assay

All *in vitro* binding assays of GBP1 to pathogenic bacteria were performed by Dr. Miriam Kutsch (Heinrich Heine University Düsseldorf), who also wrote this section. Binding of GBP1 to bacteria was analyzed as described previously (Dickinson et al., 2023; Kutsch et al., 2020). An overnight culture of pathogenic *E. coli* (DSM1103) expressing eGFP was diluted 1:30 and grown at 37 °C under shaking at 140 rpm in 5 ml LB. After 2 hours, 3 ml bacterial culture was pelleted, washed with 1x PBS, and fixed in 4% formaldehyde in PBS, pH 7.4 for 20 min. Formaldehyde-fixed bacteria were washed twice with 1x PBS. For the *in vitro* binding assays, bacteria were diluted in Assay buffer A supplemented with 50 µM BSA and shortly centrifuged at 500x g onto the cover slide of a glass bottom 10 mm microwell dish. Wild-type and mutant GBP1-AF647 (see 3.3.2) were diluted in Assay buffer A supplemented with 50 µM BSA, mixed with GTP, and the mixture was added to and gently mixed with bacteria at t = 0 min (final concentrations: 10^5-3 x10^6 bacteria/ml, 10 µM GBP1, and 2 mM GTP). Time-lapse confocal microscopy imaging was used to visualize GBP1 binding to bacteria over time. Images were collected every 1.5 min and after 30 min, different field of views were imaged for quantification. Imaging was performed on an inverted Zeiss 880 Airyscan Laser Scanning Confocal Microscope using a Zeiss Plan-Apochromat 63×/ 1.4 oil DIC M27 objective. All images were processed with Fiji. Quantitative analysis of high content confocal microscopy images was done using the machine learning-based image analysis platform HRMAn2.0 (Fisch et al., 2021; Fisch et al., 2019b).

3.3.13 Structure analysis, sequence alignment, and model generation

Protein structures (Table 3) were analyzed in Chimera (Pettersen et al., 2004). Molecular superimposition, morphing of conformations, and preparation of figures of protein structures was performed in Chimera. EM maps (Table 4) were analyzed in ChimeraX (Meng et al., 2023). Fitting protein structures into EM maps and preparation of figures including EM maps was performed in ChimeraX. Sequence alignments were performed with Clustal Omega (Sievers et al., 2011) and ESPript (Robert and Gouet, 2014). The model of outstretched dimeric GBP1 (PDB 8r1a) was generated in Chimera as SWISS-MODEL (Waterhouse et al., 2018) based on the published crystal structure of GBP5-ΔGED (PDB 7e5a) combined with the AlphaFold2 prediction (Jumper et al., 2021; Mirdita et al., 2022) of the dimeric MD and GED of GBP1. Structural predictions of the helix α4' variants with Gly-Ser substitutions were generated with AlphaFold2.

3.4 Transmission electron microscopy

3.4.1 Negative-stain electron microscopy

For negative-stain EM analysis of membrane-bound GBP1 oligomers, 10 µM farnesylated GBP1 was reconstituted on 0.5 mg/ml liposomes in Assay buffer A supplemented with 2 mM GTP or 200 µM GDP, 300 µM $AlCl_3$ and 10 mM NaF (GDP•AlF_x) and incubated for 1 min (GTP) or 10 min (GDP•AlF_x) at RT. For negative-stain EM analysis of soluble GBP1 polymers, 10 µM farnesylated GBP1 was mixed with 200 µM GDP, 300 µM $AlCl_3$ and 10 mM NaF in Assay buffer A and incubated for 15-20 min at RT. Samples were diluted 1:10 in Assay buffer A (containing GTP or GDP•AlF_x) and 3.5 µl were applied to glow-discharged carbon-coated copper grids (QUANTIFOIL Cu300 R 1.2/1.3, Quantifoil Micro Tools), incubated for 30 s, blotted, stained with 3.5 µl 2% (w/v) uranyl acetate for 30 s, blotted again, and air-dried for at least 2 h. All samples were imaged using a Talos L120C electron microscope (Thermo Fisher Scientific) at 120 kV on a Ceta Detector.

For quantification of uniform protein coat formation, the number of gaps per GBP1-coated liposomes was assessed in a blinded experiment. For each construct (GBP1 wild-type and Δ207-223), 100 micrographs of single liposomes were collected randomly and gaps within the protein coat were counted by seven independent experimenters. Averages were calculated and the *P* values were derived by an unpaired *t*-test.

3.4.2 Cryo-electron microscopy

3.4.2.1 Grid preparation

Membrane-bound GBP1 oligomers were prepared in Assay buffer A in the presence of 200 µM GDP, 300 µM $AlCl_3$ and 10 mM NaF (GDP•AlF_x) as described in 3.4.1. Prior to plunge-freezing, 5 nm gold fiducial beads were added to the samples at 1:40 ratio. 4 µl of undiluted sample was applied on glow-discharged UltrAuFoil R 2/2 gold grids (Quantifoil Micro Tools), back-blotted for 2 s, flash-frozen in liquid ethane using a Vitrobot Mark II device (FEI), and stored under liquid nitrogen conditions. Soluble GBP1 polymers were assembled by incubating 5 µM farnesylated GBP1 with 200 µM GDP, 300 µM $AlCl_3$ and 10 mM NaF (GDP•AlF_x) in Assembly buffer A for 20-30 min at RT. 4 µl of undiluted sample was applied on glow-discharged UltrAuFoil R 1.2/1.3 gold grids (Quantifoil Micro Tools), back-blotted for 2 s, flash-frozen in liquid ethane using a Vitrobot Mark II device (FEI), and stored under liquid nitrogen conditions. Grids were screened and optimized using a Talos L120C electron microscope (Thermo Fisher Scientific) at 120 kV on a Ceta Detector.

3.4.2.2 Cryo-ET data collection

For membrane-bound GBP1 oligomers, a total set of 104 tilt series was imaged on a Titan Krios G3i electron microscope (Thermo Fisher Scientific) operated at 300 kV. Tilt series of +/- 60° were acquired at magnification of 42,000x (1.1 Å per pixel in super-resolution mode) using SerialEM with a Hybrid-STA (Sanchez et al., 2020). Frame stacks with an exposure dose of 2.8 $e^-/Å^2$ for non-zero tilted projection and 14.4 $e^-/Å^2$ for zero tilted projection were recorded on a Gatan K3 electron detector. Defocus values varied from -2.0 µm to -5.0 µm. Detailed experimental information is summarized in Appendix B.

3.4.2.3 Cryo-ET image processing and tomogram reconstruction

Image processing and tomogram reconstruction of GBP1-coated liposomes was carried out in collaboration with Xiaofeng Chu (Kudryashev Lab, Max-Delbrück-Center, Berlin). Raw images output were directly fed to TomoBEAR (Balyschew et al., 2023), a workflow engine for streamlined processing of cryo-electron tomographic data for subtomogram averaging. Briefly, the TomoBEAR pipeline was described as follows (see Figure 11): raw images were sorted according to different tilt series, MotionCor2 (Zheng et al., 2017) was used for correcting beam-induced motion, IMOD (Kremer et al., 1996) was used for generating tilt stacks, fiducial beads were detected by Dynamo (Castano-Diez et al., 2012), GCTF (Zhang, 2016) was used for defocus estimation, IMOD was then used for fiducial model refinement and tomographic

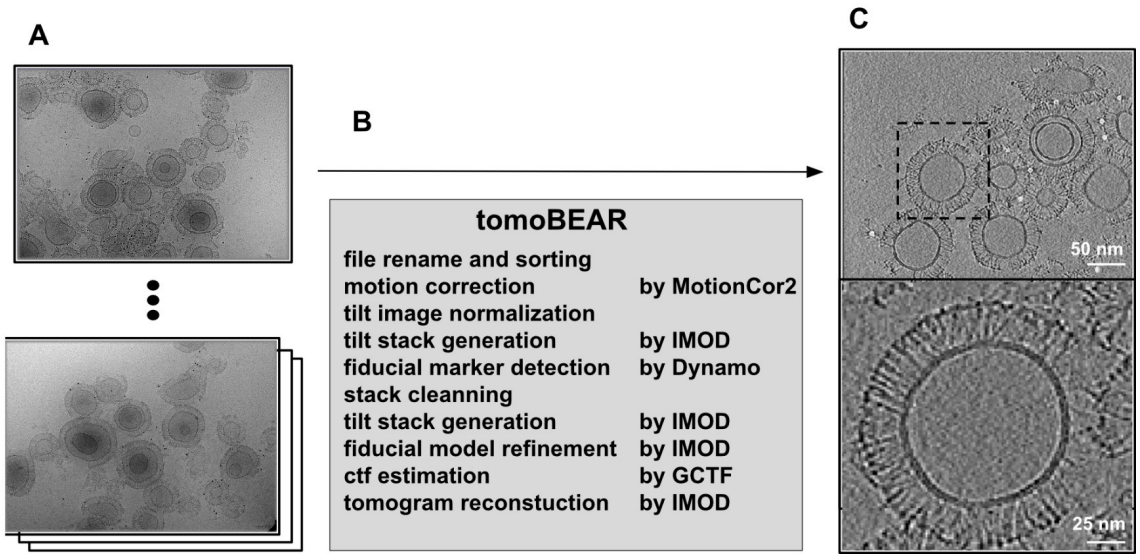

Figure 11. Cryo-ET image processing workflow. (A) Raw images output from electron microscope. **(B)** Pipeline of processing and reconstruction executed by TomoBEAR (Balyschew et al., 2023). **(C)** Snapshot of the reconstructed tomogram (upper panel) and enlarged view of the marked GBP1 covered vesicle (lower panel). Figure was prepared and provided by Xiaofeng Chu (Kudryashev Lab, Max-Delbrück-Center, Berlin).

reconstruction. Coordinates for sub-tomograms were manually generated in Dynamo by DipoleSet models to describe vesicular geometry. Each liposome was handled as a dipole with a center and a radius which could output the coordinate of the membrane surface.

3.4.2.4 Subtomogram Averaging

Subtomogram Averaging (STA) was performed by Xiaofeng Chu (Kudryashev Lab, Max-Delbrück-Center, Berlin). The STA pipeline of membrane-bound GBP1 is summarized in Appendix C. Segments were cropped and classified by Dynamo using coordinates of the membrane surface (see 3.4.2.3). Preliminary classification was executed with 70,160 segments and six classes at pixel size of 17.6 Å. Four classes with clear density of membrane and GBP1 protein were selected (46,782 segments). Selected segments were further classified into six classes at pixel size of 4.4 Å. Subsequently, a class of 6,145 segments with clear GBP1 density was selected for the Dynamo 3D refinement which resulted in a map of membrane-bound GBP1 dimers at a moderate resolution of ~26 Å. Resolution and Fourier Shell Correlation curve was computed as described by Scheres and Chen (2012).

3.4.2.5 Cryo-EM data collection

A set of 6,483 micrographs of soluble GBP1 polymers were acquired on a Titan Krios G3i electron microscope (Thermo Fisher Scientific, 300 kV) at magnification of 81,000x (0.53 Å per pixel in super-resolution mode) using EPU (Thermo Fisher Scientific). Frame stacks with an exposure dose of 1.165 $e^-/Å^2$ were recorded on a Gatan K3 electron detector using defocus values between -0.7 µm and -2.0 µm. Detailed experimental information is summarized in Appendix B.

3.4.2.6 Single particle analysis

For single particle analysis (SPA) of polymeric disks, dose-fractionated image stacks were subjected to MotionCor2 (Zheng et al., 2017) and CTFFIND4 (Rohou and Grigorieff, 2015) in Relion4.0 (Kimanius et al., 2021). An initial particle set of 101,449 particles (4.24 Å pixel size) was generated by manual and template-based particle picking in Relion4.0 followed by 2D classification rounds for cleaning. Afterwards, 3D classification using an initial reconstruction of a particle subset was performed and best classes were selected (53,452 particles). Following several rounds of 3D classification using a manual created low-pass filtered map of one planar disk lacking GED domains, a final set of 15,952 particles allowed for an initial low-resolution 3D reconstruction (~37 Å) of stacked polymeric disks without applying symmetry, displaying the general composition of its assembly. The SPA workflow for polymeric GBP1 disks is summarized in Appendix D.

4 Results

4.1 Sample preparation for cryo-electron microscopy

Highly pure protein, optimized sample conditions, and optimal conditions cryo-EM grid preparation are key aspects of any successful protein structure determination by cryo-electron microscopy (cryo-EM). This chapter deals with the purification process of His_6-tagged farnesylated human GBP1, the optimization of GBP1 coat formation on liposomes, and the screening of optimal grid conditions for cryo-EM data acquisition.

4.1.1 Protein purification of GBP1

Human GBP1 co-expressed with human farnesyltransferase (FTase) has been shown to be farnesylated *in vivo* in an *E. coli* expression system (Fres et al., 2010; Sistemich and Herrmann, 2020). Alternatively, GBP1 can be farnesylated *in vitro* by enzymatic modification using purified FTase and non-farnesylated GBP1 (Dickinson et al., 2023; Sistemich and Herrmann, 2020), both as described in 3.3.1. Farnesylated GBP1 was purified by immobilized metal affinity chromatography (IMAC) followed by hydrophobic interaction chromatography (HIC) and size exclusion chromatography (SEC). Representative results of the purification process are shown in Figure 12. As reported and validated by Fres et al. (2010) and Sistemich and Herrmann (2020), the pooled fractions of the HIC (~75 mS/cm) represent farnesylated GBP1, while non-farnesylated GBP1 together with FTase elute at reduced salt concentration (~45 mS/cm). This way, farnesylated protein was successfully purified from non-farnesylated protein.

All farnesylated GBP1 constructs used for biochemical assays and negative-stain EM analysis in this thesis were purified following the same *in vivo* farnesylation protocol. Protein used for cryo-EM studies in this thesis has been purified by my collaboration partner Dr. Paul Lauterjung (Ruhr University Bochum) according to the *in vitro* farnesylation protocol as specified in 3.3.1, in order to maximize farnesylation efficiency. For detailed biochemical studies, purified protein was labeled with fluorescence probes as described in 3.3.2

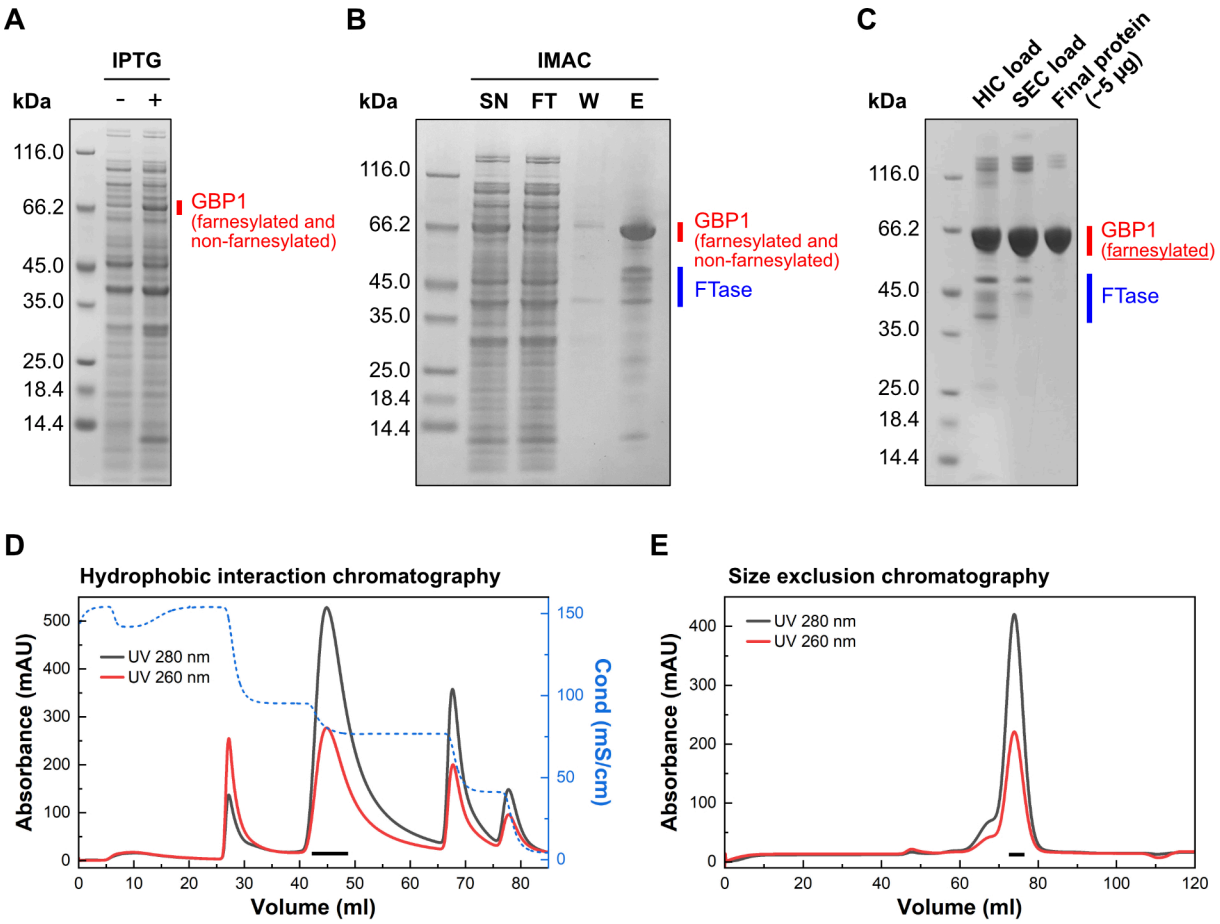

Figure 12. Protein purification of farnesylated GBP1. Representative SDS-PAGE **(A-C)** and chromatograms **(D-E)** for the *in vivo* farnesylation method by co-expression with human farnesyltransferase (FTase). **(A)** Overexpression of GBP1 upon IPTG induction in *E. coli* BL21 (DE3). **(B)** Immobilized metal affinity chromatography (IMAC) using Ni Sepharose HP resin. SN: supernatant, FT: flow-through, W: wash, E: elution. **(C)** Final product and loading controls. 5 µg final protein was loaded in the last lane. **(D)** Hydrophobic interaction chromatography (HIC) following IMAC. Elution by decreasing salt concentration ($(NH_4)_2SO_4$). Pooled fractions for size exclusion chromatography (SEC) are marked with a black line. **(E)** Size exclusion chromatography (SEC). Pooled fractions of the final protein are marked with a black line.

4.1.2 Optimization of GBP1 coat formation on liposomes

GBP1 has been shown to form a protein coat on gram-negative bacteria and artificial liposomes, the so-called coatomer (Kutsch et al., 2020; Piro et al., 2017; Shydlovskyi et al., 2017; Sistemich et al., 2021). For a structural analysis of the membrane-bound GBP1 coatomer, protein coat formation was analyzed on liposomes derived from two brain lipid mixtures (Folch extract and Brain Polar Lipid extract, BPL) using liposome co-sedimentation assays (see 3.3.3 and 3.3.4). Since the GED opening of GBP1 including the release of its farnesyl moiety strongly depends on binding and hydrolysis of GTP (Shydlovskyi et al., 2017; Sistemich et al., 2021; Sistemich et al., 2020), binding to liposomes was tested in the presence of different nucleotides (Figure 13). Sedimentation of GBP1 was observed in the presence of GTP and the GTP transition state analogue, GDP•AlF_x, but not in the presence of GDP or the non-hydrolysable GTP analogues, guanosine 5'-O-[γ-thio]triphosphate (GTPγS) and guanosine-5'-[(β,γ)-imido]triphosphate (GMPPNP). Sedimentation was not dependent on the presence of liposomes as reported previously (Fres et al., 2010; Shydlovskyi et al., 2017), suggesting the formation of non-membrane-bound, 'soluble' polymers which can also be sedimented (Figure 13).

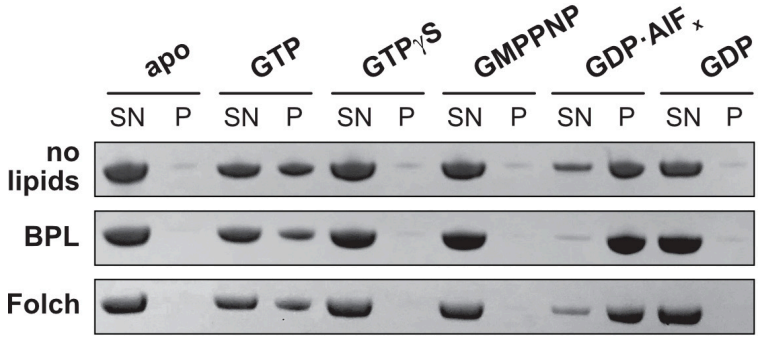

Figure 13. Liposome co-sedimentation assay. GBP1 was incubated with indicated nucleotides and respective liposomes of brain-derived lipid extracts. SN: supernatant fraction, P: pellet fraction.

To distinguish between liposome binding and liposome-independent polymer formation, a FRET-based liposome-binding assay with donor-labeled GBP1 and acceptor-labeled liposomes was employed (see 3.3.5). Prominent changes in the FRET efficiency indicating membrane binding were only observed when BPL liposomes and GDP•AlF_x were used (Figure 14A). At GBP1 concentration greater than 10 µM, the FRET signal saturated indicating full coating of the liposomes (Figure 14B).

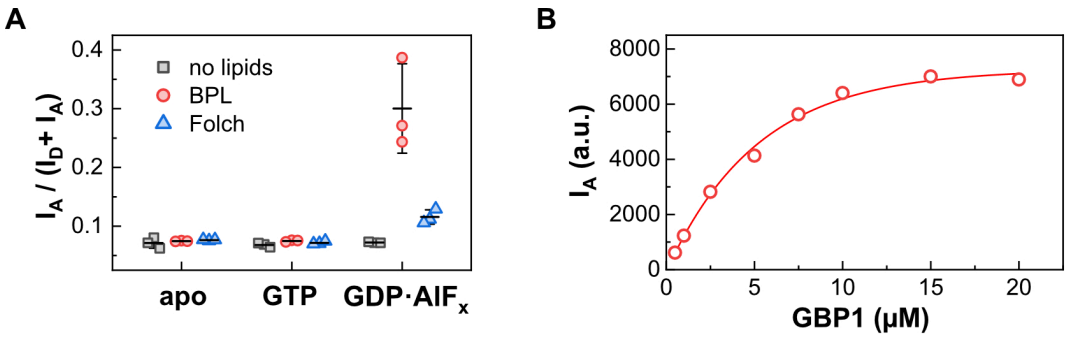

Figure 14. FRET-based liposome binding assay. (A) Ratiometric FRET efficiencies of GBP1-Q577C-AF488 (donor) incubated with indicated liposomes supplemented with Liss Rhod PE (acceptor) and indicated nucleotides. Data from three independent replicates are shown as mean ± SD. **(B)** Concentration dependency of GBP1 binding to liposomes. Acceptor intensity of varying GBP1-Q577C-AF488 (donor) concentration at constant BPL liposome concentration supplemented with Liss Rhod PE (acceptor).

Indeed, in negative-stain transmission electron microscopy (TEM, 3.4.1), a stable protein coat was only observed for BPL liposomes in the presence of GDP•AlF$_x$ (Figure 15). In rare cases, soluble polymers have been found to be attached to protein-coated BPL liposomes (Figure 16). In contrast, in the presence of liposomes constituted by Folch lipids, liposome-independent polymer formation was favored over membrane binding.

Regarding the differences in protein reconstitution between the two used brain extracts, there is no detailed information about their composition in literature or provided by the suppliers. Brain polar lipid (BPL) extract is derived from a total lipid extract by precipitation with acetone, which is not done in the Folch extraction procedure (Folch et al., 1957). Acetone precipitates phospholipids, while, for example, glycolipids and other simple lipids dissolve readily in acetone (Hanahan et al., 1951). To study the differences between Folch and BPL liposomes, acetone precipitation with the Folch extract was performed according to Hanahan et al. (1951). However, there was no significant improvement in liposome-binding with lipids

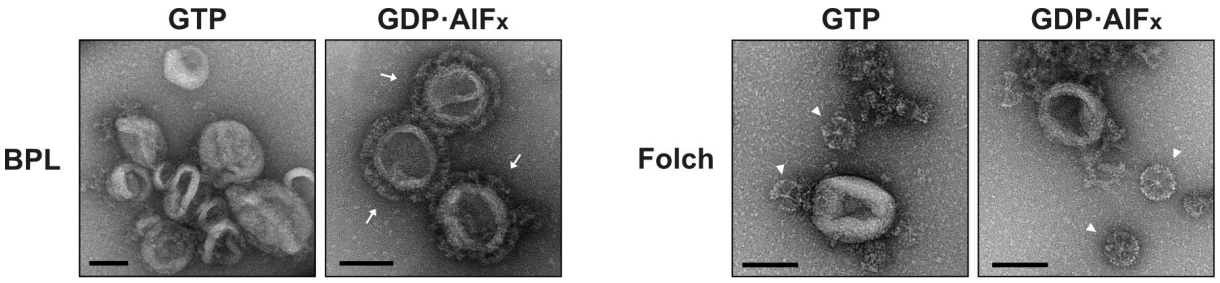

Figure 15. Negative-stain TEM of GBP1 reconstitution. Arrows indicate stable GBP1 coat, arrow heads represent soluble polymers of GBP1. Scale bars are 100 nm.

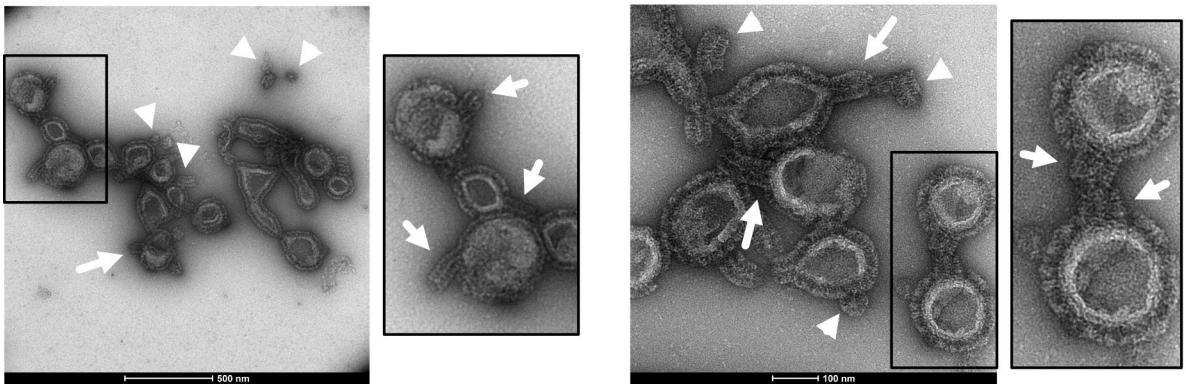

Figure 16. Rare binding events of soluble polymers to coated BPL liposomes. Oligomerization initiated with GDP•AlF_x. Arrows: attached polymers. Arrow heads: soluble polymers/disks. Scale bars as indicated.

derived from this procedure (Figure 17). Next, specific lipids were supplied to Folch liposomes and tested whether they may rescue GBP1-binding. Since GBP1 has a C-terminal polybasic motif (^{584}RRR^{586}) which is required for binding to bacteria (Kutsch et al., 2020; Piro et al., 2017), supplementation of lipids with negatively charged head groups (10% phosphatidylinositol-4,5-bisphosphate or 10% phosphatidyl-serine) was tested in the FRET-based liposome binding assay. However, this did not increase GBP1 binding (Figure 17). Finally, Folch lipids were supplemented with 25% cholesterol in order to modulate membrane fluidity and elasticity. Indeed, this approach increased membrane-binding and FRET efficiency in the Folch mixture almost to the same level as seen for BPL liposomes. This may indicate that high membrane fluidity and elasticity promote GBP1 binding to liposomes.

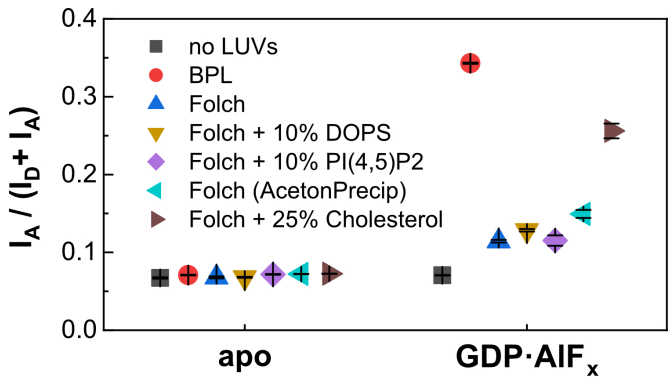

Figure 17. FRET-based liposome binding assay for probing differences between BPL and Folch lipids. Ratiometric FRET efficiencies of GBP1-Q577C-AF488 (donor) incubated with indicated liposomes supplemented with Liss Rhod PE (acceptor) and indicated nucleotides. DOPS: 1,2-dioleoyl-sn-glycero-3-phospho-L-serine. PI(4,5)P2: phosphatidylinositol-4,5-bisphosphate. AcetonPrecip: acetone precipitation. Data from three independent replicates are shown as mean ± SD.

4.1.3 Screening of optimal cryo-EM grid conditions

Having optimized the reconstitution of pure, farnesylated GBP1 on liposomes, different conditions for preparing cryo-EM grids were probed. First, GBP1-coated liposomes were applied on carbon-coated grids at the same protein concentration and buffer composition as in the oligomerization reaction (see 3.4.2.1). Although some of the liposomes clustered within the holes, these conditions were already found to be suitable for cryo-electron tomography (cryo-ET). However, during data acquisition of tilt series, the high electron dose caused the carbon of the grids to deteriorate, especially at high tilt angles, which made this data less suitable for further image analysis. Switching to UltrAuFoil R 2/2 gold grids resolved this issue and provided a cryo-ET tilt series dataset suitable for tomogram reconstruction and subtomogram averaging.

Second, cryo-EM grid conditions for soluble polymers observed in Figure 15 were optimized to acquire a single particle data set. In a first attempt, increasing protein concentrations ranging from 10 µM to 40 µM were screened on carbon-coated grids. In all tested conditions, the carbon was coated with particles and most of the holes were found empty. In cases where there were particles in the ice, clustering and preferred orientation were observed. Systematic attempts were made to reduce particle clustering and the attachment of the particles to the carbon support. This included increasing the ionic strength using NaCl concentrations up to 300 mM, increasing the acidity by lowering the pH to pH 5.0, and performing a second sample application step after blotting to saturate the carbon support first. However, no improvement was observed, and most holes remained empty, only a few showed either large protein clusters or had too few particles in it. Changing from carbon-coated grids to UltrAuFoil R 1.2/1.3 gold grids reduced the number of empty holes and improved the overall number of single particles in the holes, though partial clustering and preferred orientation persisted. These grid conditions were used for a cryo-EM single particle dataset (see exemplary micrograph in section 4.2.2).

4.2 Cryo-electron microscopy of GBP1 oligomers

GBP1 has been shown to assemble into large oligomers in solution and on lipid membranes (Kuhm et al., 2023; Shydlovskyi et al., 2017; Sistemich et al., 2021; Sistemich et al., 2020; Zhu et al., 2024), but detailed structural insights into the oligomeric states are missing. Applying cryo-ET imaging and subtomogram averaging of GBP1-coated liposomes as well as single particle cryo-EM imaging of polymeric GBP1 in solution, this section focuses on the overall architecture of GBP1 oligomers.

Conditions for sample and grid preparation were optimized as described in 4.1.2 and 4.1.3. A set of 115 cryo-ET tilt series was collected for the membrane-bound GBP1 coatomer and reconstructed into tomograms together with my collaboration partner Xiaofeng Chu (see 3.4.2.2 and 3.4.2.3). For single particle cryo-EM imaging of soluble GBP1 polymers, 6,483 micrographs were acquired as described in 3.4.2.5.

4.2.1 Overall architecture of the membrane-bound GBP1 coatomer

In the reconstructed cryo-ET volumes of BPL liposomes, the GDP•AlF_x-bound GBP1 coatomer was well recognizable (Figure 18A). The protein coat had an average height of 28.3 nm ± 1.6 nm (Figure 18B), which agrees well with the theoretical dimension of a dimeric, outstretched GBP1 dimer (~28.8 nm, Figure 18C). Subtomogram averaging of 70,160 segments picked along the liposome surface was performed by my collaboration partner Xiaofeng Chu and resulted in a map of membrane-bound GBP1 dimers at a moderate resolution of ~26 Å (Figure 19A, Appendix C). The dimension of the density corresponded to the outstretched conformation of dimeric GBP1. Although the map did not allow for a detailed molecular fitting of the GBP1 dimer, it suggested the potential oligomerization interfaces (Figure 19B). Based on the absence of density outside the dimer, the MD and GED were apparently not involved in higher order assembly. However, it cannot be excluded that the potentially existing, weak interactions between these domains may have been averaged out as a result of a high flexibility within the oligomer. In contrast, the dimeric LG domains displayed lateral contacts mediating the formation of a two-dimensional protein lattice.

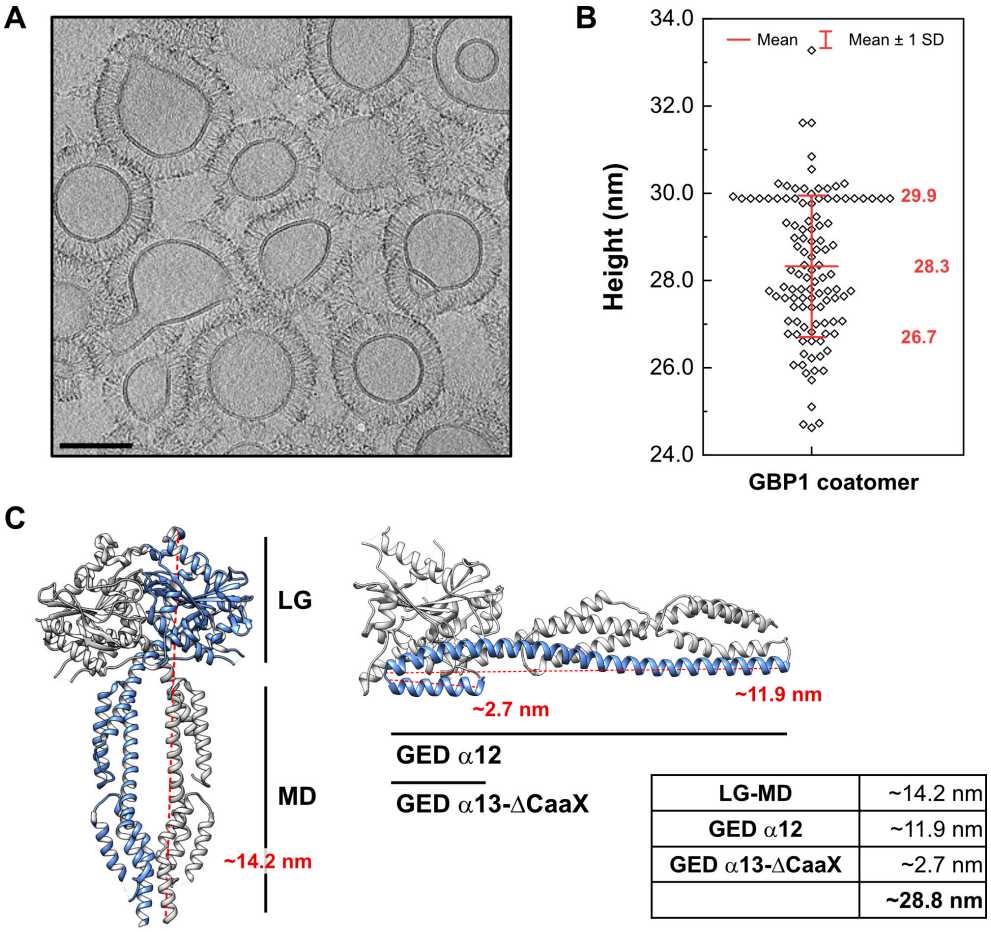

Figure 18. Analysis of the membrane-bound GBP1 coatomer. (A) Cross section of the cryo-ET volume of GBP1-coated BPL liposomes. Scale bar is 100 nm. **(B)** Quantification of the coatomer height. 22 coated liposomes at five random positions were analyzed by measuring the distance from the lipid membrane to the very top of the coatomer (n=110). Average is shown as mean ± SD. **(C)** Theoretical length of outstretched GBP1. Left: GBP5-ΔGED dimer in complex with GDP•AlF_x (PDB 7e5a), Right: GBP1 in apo state (PDB 1dg3).

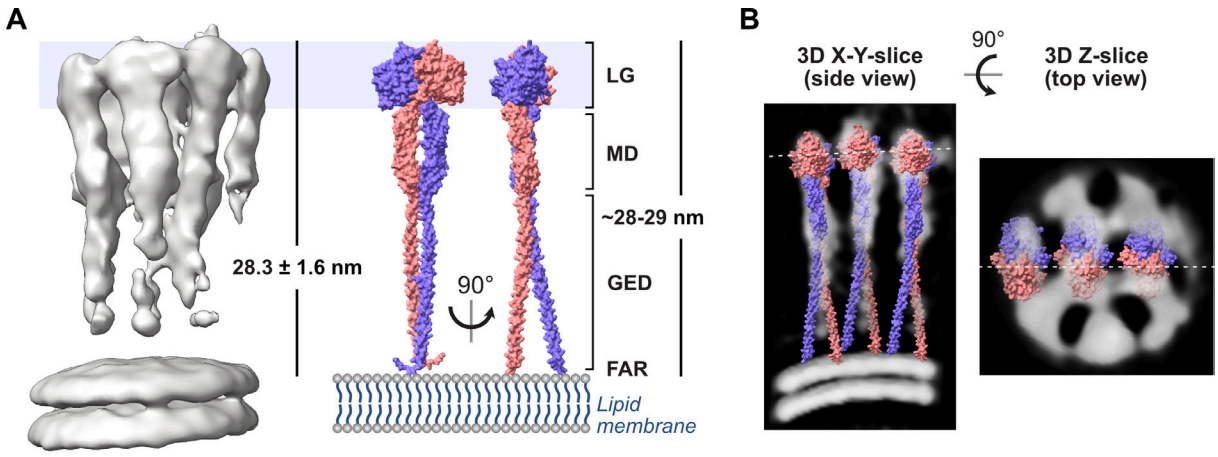

Figure 19. Architecture of the membrane-bound GBP1 coatomer. (A) Subtomogram averaging result of the GBP1 coatomer, done by Xiaofeng Chu (Max Delbrück Center). Coatomer height (n=110, mean ± SD) correlates with theoretical length of an outstretched dimeric GBP1 model, generated as SWISS-MODEL (Waterhouse et al., 2018) based on the published crystal structure of GBP5-ΔGED combined with the AlphaFold2 prediction (Jumper et al., 2021; Mirdita et al., 2022) of the dimeric MD and GED of GBP1 (see 3.3.13). **(B)** Side and top view slices of the subtomogram averaging result. Dashed lines indicate the respective slice position. The outstretched dimeric GBP1 model is fitted into the protein densities.

4.2.2 Overall architecture of soluble GBP1 polymers

In the absence of lipid membranes and presence of GDP•AlF_x, GBP1 polymerized into stable disk-like structures with an outer diameter of 58.7 nm ± 1.0 nm (Figure 20A, B) consistent with recently reported findings (Kuhm et al., 2023; Shydlovskyi et al., 2017). Aiming to obtain an overview of the polymeric assembly, single particle cryo-EM imaging was performed. Particles of polymeric disks were highly heterogeneous and allowed only for a low-resolution 3D reconstruction at a resolution of ~37 Å, which nevertheless provided a basic understanding of the discs' architecture (Figure 20C, Appendix D). 30 subunits arrange into a planar ring-like structure and show a prominent central density connecting to the outer ring via faint protein densities. The distance between the outer and inner ring was ~28 nm, corroborating with the dimension of the dimeric GBP1 model in its open outstretched conformation. In this orientation, the farnesyl moieties constitute the central ring-like density with a pore size of few nanometers in diameter, whereas the LG dimers assemble in the peripheral ring. Faint protein densities next to one LG dimer match the dimension of the MD (~8 nm) and the diffused densities between the MD and the prominent density of the C-terminal farnesyl ring match the dimensions of the GED (~15 nm), suggesting that GBP1 dimers in the outstretched conformation are the building blocks of the polymers. The model further indicates that interdimeric interfaces are established between LG domains laterally. 2D classification of short

tubular structures in side views further showed that larger oligomeric assemblies are apparently formed by stacking of planar disks (Figure 20D). The distance between two disks was ~8 nm which agrees well with the dimension of two stacked GBP1 dimers (Figure 20E). Although the largest 3D class from classification supports a stacking mechanism, minor populations within 2D classes appear offset, suggesting that at least some particles or regions have helical symmetry (Appendix D). Together, both the membrane-bound and polymeric state reveal an outstretched dimeric conformation of GBP1, and regions at the periphery of the LG domain dimer contribute to the higher-order oligomeric assembly.

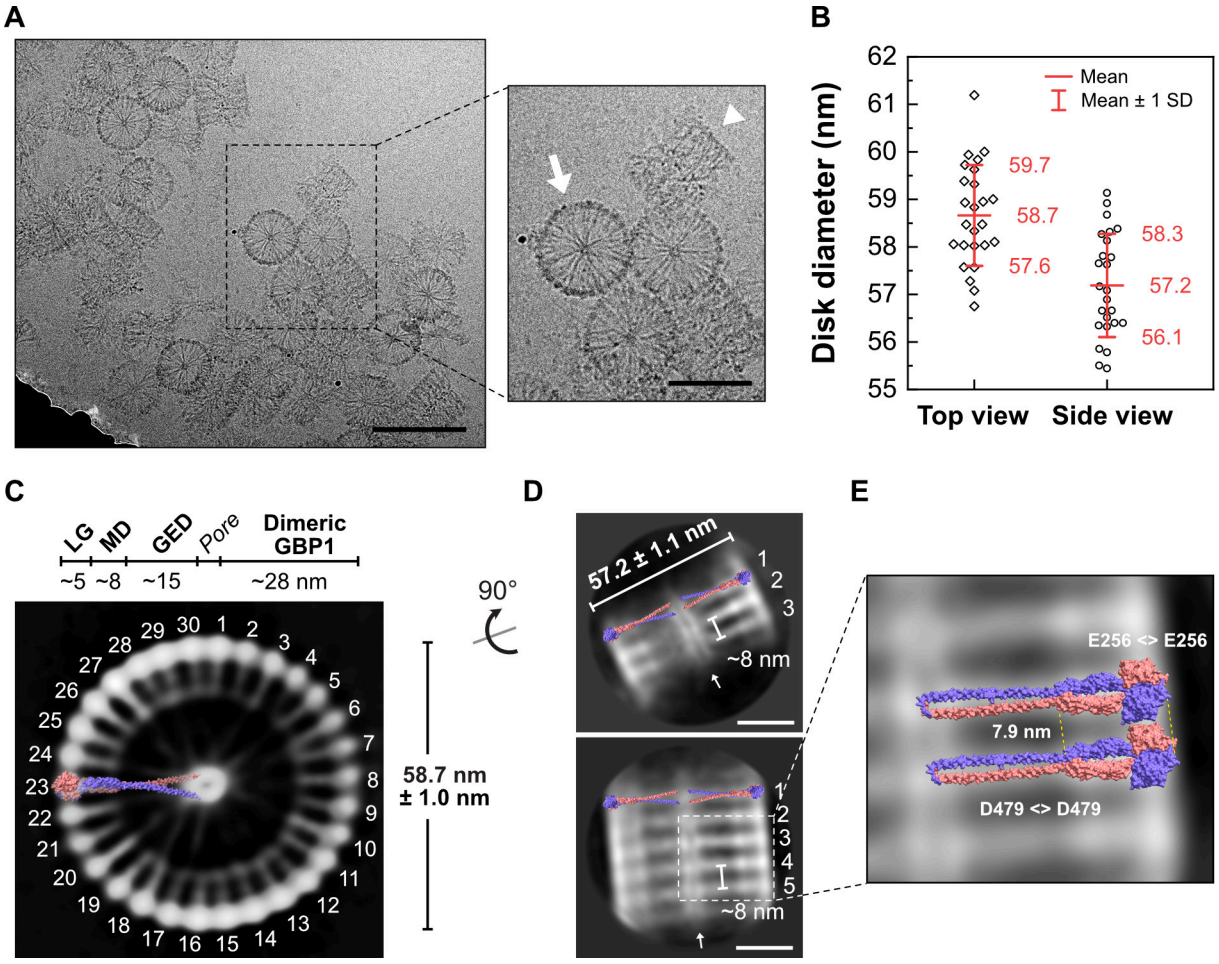

Figure 20. Architecture and analysis of soluble GBP1 polymers. (A) Cryo-EM micrograph of polymeric assembly into disk-like structures. Arrow: planar disk in top view, arrow head: stacked disks in side view. Scale bar is 100 nm. **(B)** Quantification of the diameter of disks in top view and stacks in side views (n=25). Averages are shown as mean ± SD. **(C)** Z-slice of the GBP1 polymer 3D reconstruction. Individual building blocks are labeled and the outstretched dimeric GBP1 model is fitted into the protein densities. Dimensions of individual protein domain densities are indicated and correlate with the disk diameter (n=25, mean ± SD). **(D)** 2D classes of stacked polymeric disks. The outstretched dimeric GBP1 model is placed into the protein densities. The diameter (n=25, mean ± SD) and the stack height are indicated. Top: three stacks, bottom: five stacks, arrow: middle pore. Scale bars are 20 nm. **(E)** 2D class of stacked polymeric disks modeled with the outstretched GBP1 dimer model. Distances between the LG domain and MD of two stacks were determined at Cα atoms of indicated amino acids.

4.3 The peripheral helix α4' in the LG domain mediates oligomerization

Both medium-resolution structures of the membrane-bound GBP1 coatomer and soluble GBP1 polymers obtained by cryo-electron microscopy suggested that lateral interaction between dimeric LG domains build the oligomeric interface. In this section, this oligomeric interface was biochemically characterized in a structure-function approach.

4.3.1 Re-analysis of structural transitions from the monomeric to dimeric state

To delineate the oligomerization interfaces within the GBP1 oligomer via the LG domains, previously described structural transitions from the monomeric apo to the dimeric, assembly-competent GDP•AlF_x-bound state were re-analyzed (Ghosh et al., 2006; Prakash et al., 2000b). A prominent structural rearrangement was observed for helix α4' at the distal side of the G interface that shifts by ~9 Å to avoid a steric clash with the opposing LG domain (Figure 21). As this structural transition is induced by dimerization, helix α4' was considered as suitable candidate for establishing the lateral interface between two LG domain dimers of the outstretched GBP1 conformation.

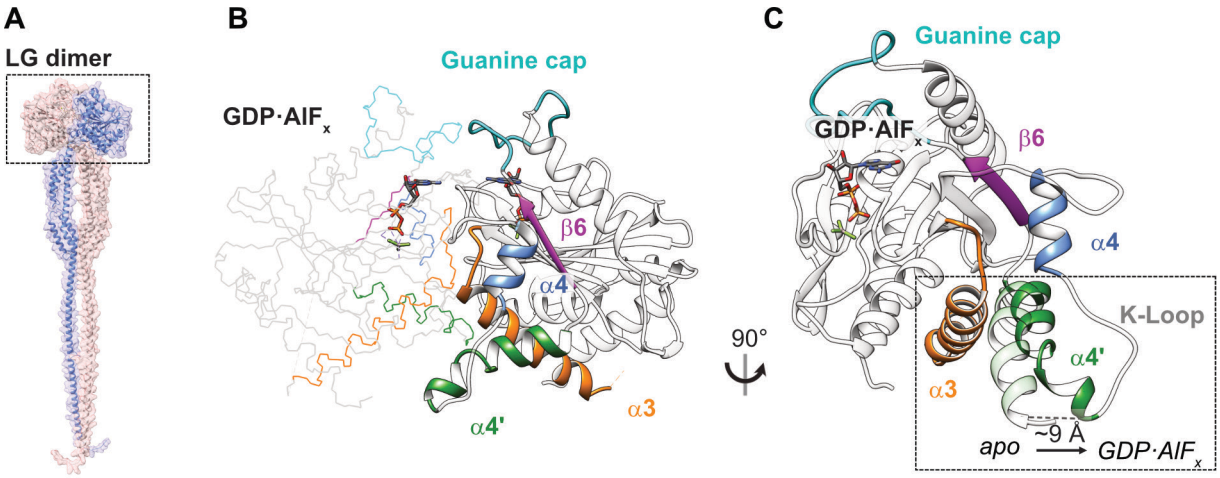

Figure 21. Structural transitions of the LG domain upon dimerization. (A) Outstretched dimeric GBP1 model (see Figure 19) with the LG dimer highlighted in the box. Structure of the **(B)** LG dimer (GDP•AlF_x-bound, PDB 2b92) and **(C)** superimposition of the GDP•AlF_x-bound (PDB 2b92) and the apo state (PDB 1dg3, transparent). The structural rearrangement of helix α4' is highlighted in the box.

4.3.2 Design of helix α4' variants with Gly-Ser substitutions

In order to probe whether the observed motion might also generate an oligomeric contact site upon dimerization, GBP1 variants in which specific parts of the protruding helix α4' were exchanged with a glycine-serine linker were designed based on structural predictions (Figure 22).

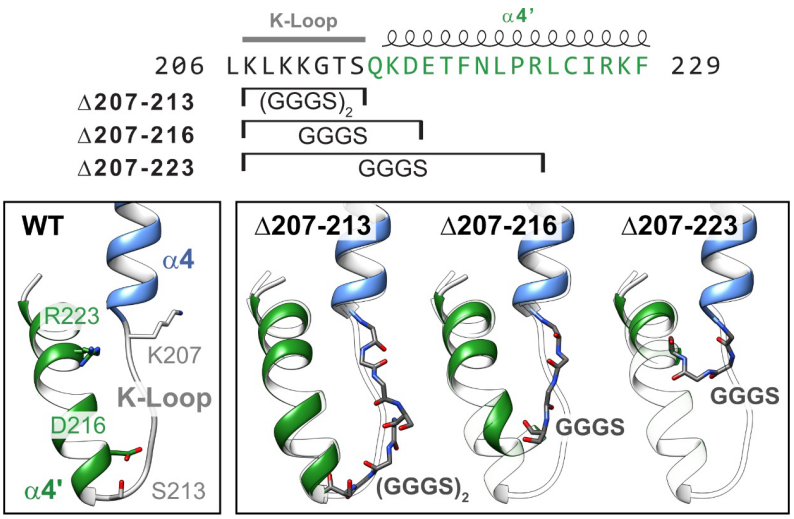

Figure 22. Design of helix α4'. Sequence of GBP1 with respective constructs marked (top). Close view of helices α4, α4', and the K-Loop with start (K207) and respective end positions (S213, D216, R223) of wild-type GBP1 (lower left), and AlphaFold2 predictions (Jumper et al., 2021; Mirdita et al., 2022) of the constructs showing the respective regions replaced by GGGS-linkers (lower right). Δ207-213 contains two GGGS repeats due to a longer distance.

Analytical size-exclusion chromatography (SEC) and circular dichroism (CD) measurements confirmed that the overall protein structure was maintained in the helix α4' variants (Figure 23). As indicated in Figure 23A, there are no significant differences in the analytical SEC profiles between the α4' mutants and the wild-type GBP1. As expected, the RK(227-228)EE mutant eluted earlier in gel filtration compared to wild-type, in line with a more extended conformation. CD measurements indicated no significant secondary structure changes of wild-type GBP1 and the α4' mutants (Figure 23B). Since only the tertiary structure is altered in GBP1 RK(227-228)EE, the spectrum and secondary structure prediction did not differ from wild-type GBP1. Hence, the three generated helix α4' constructs are suitable to use for further biochemical and structural characterization.

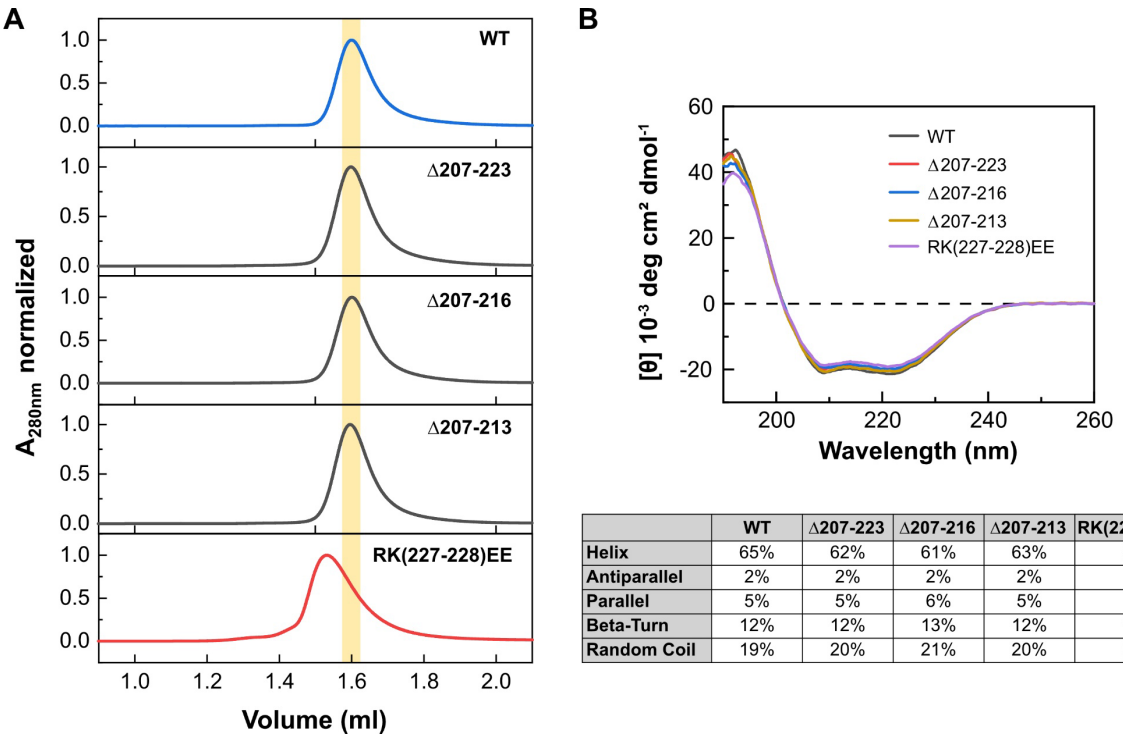

	WT	Δ207-223	Δ207-216	Δ207-213	RK(227-228)EE
Helix	65%	62%	61%	63%	58%
Antiparallel	2%	2%	2%	2%	3%
Parallel	5%	5%	6%	5%	6%
Beta-Turn	12%	12%	13%	12%	13%
Random Coil	19%	20%	21%	20%	22%

Figure 23. Helix α4' protein structure. (A) Analytical size-exclusion chromatography. Wild-type GBP1 and the open GBP1 mutant RK(227-228)EE were used as references for changes in the overall protein architecture. The peak of the monomeric wild-type GBP1 species is highlighted in yellow for comparison. **(B)** Circular dichroism. Top: CD spectra normalized according to the cell path length, protein concentration and number of amino acid residues. Bottom: Secondary-structure determination using CDNN 2.1.

4.3.3 Characterization of soluble polymer formation in the helix α4' variants

First, the ability of the three designed helix α4' variants to dimerize and polymerize was analyzed by using a crosslinking-based approach (Figure 24A, 3.3.7). Without nucleotide (apo), both non-farnesylated and farnesylated wild-type protein remained in a monomeric state. Addition of GDP•AlF_x led to dimerization of all non-farnesylated constructs, whereas farnesylated wild-type protein showed a dramatic shift toward higher molecular weight species at the top of the gel. In addition, the monomeric and dimeric states vanished for wild-type GBP1, suggesting that this species represents the crosslinked disks (Figure 20). Like wild-type, a variant with a Gly-Ser substitution of a lysine-rich loop (the K-loop) preceding helix α4' polymerized in the presence of GDP•AlF_x (construct Δ207-213), and some dimeric species were detected. When further substituting parts of helix α4', the equilibrium shifted from polymers to dimers, suggesting that GDP•AlF_x-induced polymerization, but not dimerization, was impaired. While the GBP1 Δ207-216 variant showed reduced polymer formation, polymerization of the Δ207-223 variant was mostly abolished.

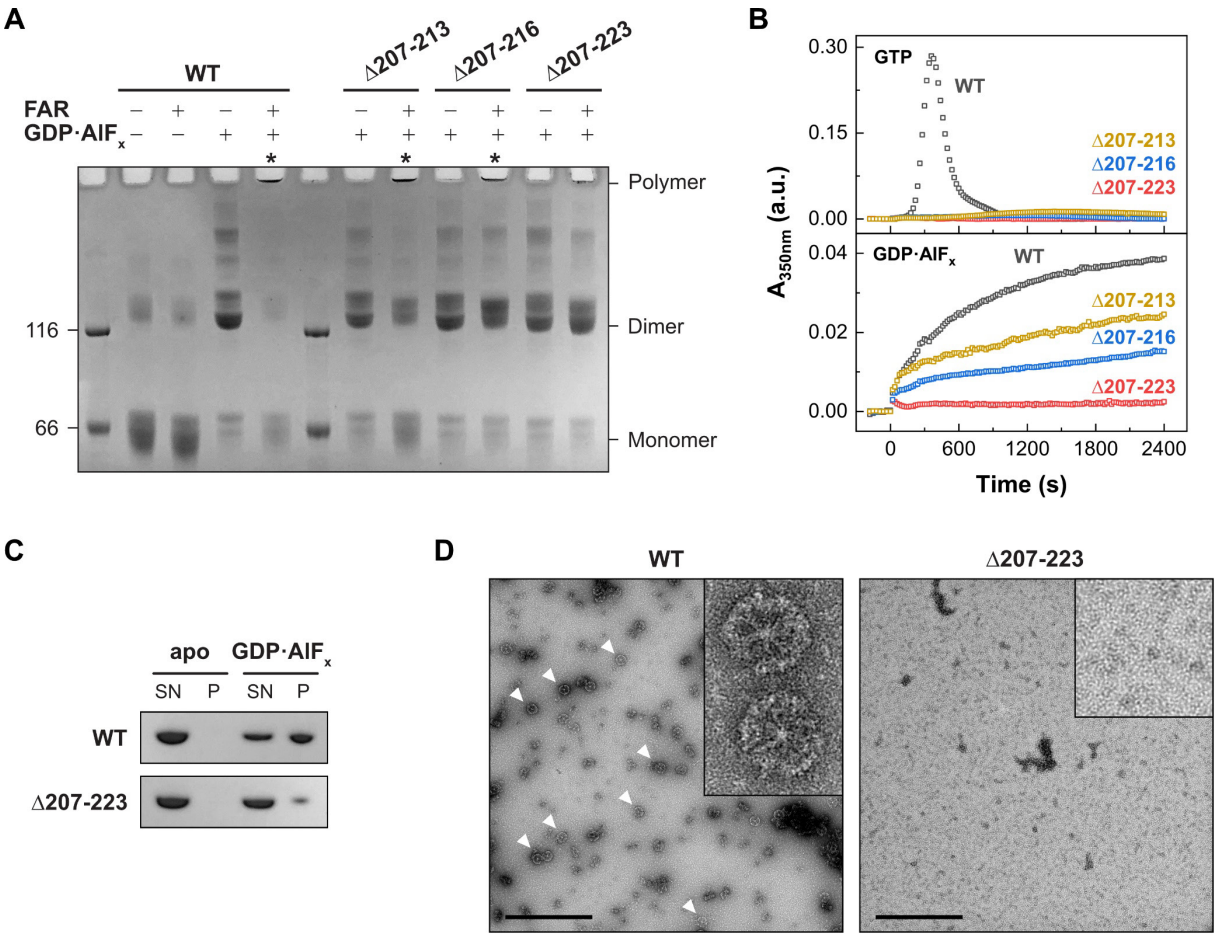

Figure 24. Polymerization-deficient helix α4' variants. (A) Crosslinking assay of helix α4' variants. The respective oligomeric states based on molecular weight are indicated. Asterisks indicate successful polymerization. FAR: farnesylated. **(B)** Light scattering-based polymerization assay of helix α4' variants. Polymerization is induced by GTP (top) and GDP•AlF$_x$ (bottom). **(C)** Sedimentation assay of oligomerization-deficient Δ207-223 mutant in the absence of lipids. SN: supernatant. P: pellet. **(D)** Negative-stain TEM of polymeric disk formation (arrow heads). Scale bars are 500 nm.

Second, using a light scattering-based approach (3.3.8), the polymerization of farnesylated GBP1 in the presence of GTP and GDP•AlF$_x$ was monitored over time. In the presence of GTP, wild-type GBP1 showed typical polymerization kinetics with an initial lag phase, which was followed by a strong increase and decrease in light scattering, due to the GTP hydrolysis-dependent assembly and disassembly of oligomeric structures (Shydlovskyi et al., 2017; Sistemich et al., 2020) (Figure 24B). In contrast, the three mutants showed only small increases in light scattering under these conditions. In the presence of GDP•AlF$_x$, farnesylated wild-type GBP1 steadily polymerized over a time span of 40 min, representing the slow formation of disk-like structures (Shydlovskyi et al., 2017) (Figure 20). In accordance with the crosslinking assay, both Δ207-213 and Δ207-216 variants polymerized in the presence of GDP•AlF$_x$, but with slower kinetics. In contrast, GBP1 Δ207-223 did not polymerize,

suggesting a crucial role of helix α4’ in oligomer formation. Sedimentation experiments and negative-stain TEM analysis further supported these findings. While wild-type GBP1 was sedimented in the presence of GDP•AlF_x, the vast majority of mutant Δ207-223 remained in the supernatant (Figure 24C). Using negative-stain TEM, polymeric disks were only observed for wild-type GBP1, but not for the GBP1 Δ207-223 mutant (Figure 24D).

4.3.4 Characterization of coatomer formation in the Δ207-223 mutant

Next, the effect of the Δ207-223 substitution on the formation of the GBP1 coatomer was investigated. In the monomeric state, helix α4’ is involved in an intramolecular LG:GED interaction via a salt bridge network between R227/K228 and the four glutamate residues 556, 563, 568, and 575 within helix α12/13 (Vopel et al., 2010) (Figure 25). To address whether the GBP1 Δ207-223 variant can adopt the open dimeric state with an accessible farnesyl moiety, liposome co-sedimentation experiments were performed and revealed that both wild-type GBP1 and the Δ207-223 variant bound to BPL liposomes (Figure 26A). This implies that the Δ207-223 variant like wild-type GBP1 has an accessible farnesyl anchor and can exist in an open dimeric conformation. Interestingly, the GBP1 Δ207-223 variant failed to establish a uniform protein coat on BPL liposomes, but rather formed protein patches on liposomes resulting in a high number of gaps within the protein coat (Figure 26B, C). This observation suggests that weaker interactions between GBP1 dimers prevent the formation of a stable protein coat. Hence, helix α4’ is not only crucial for the oligomerization of soluble GBP1 polymers, but also for the formation of a uniform and stable protein coat on membranes.

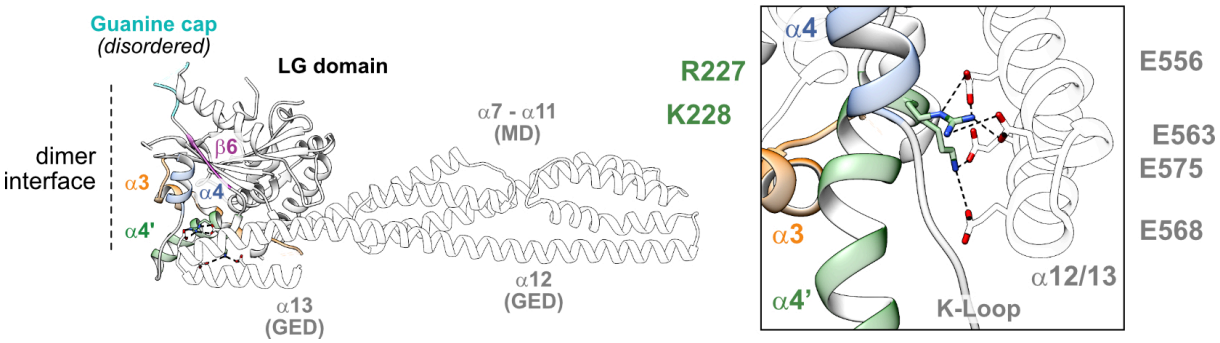

Figure 25. Intramolecular LG:GED contacts. The crystal structure of full-length GBP1 in the closed monomeric state (apo, PDB 1dg3) shows a salt bridge network between R227/K228 of helix α4’ (LG) and the four glutamate residues 556, 563, 568, and 575 of helix α12/13 (GED), stabilizing the closed conformation (Vopel et al., 2010).

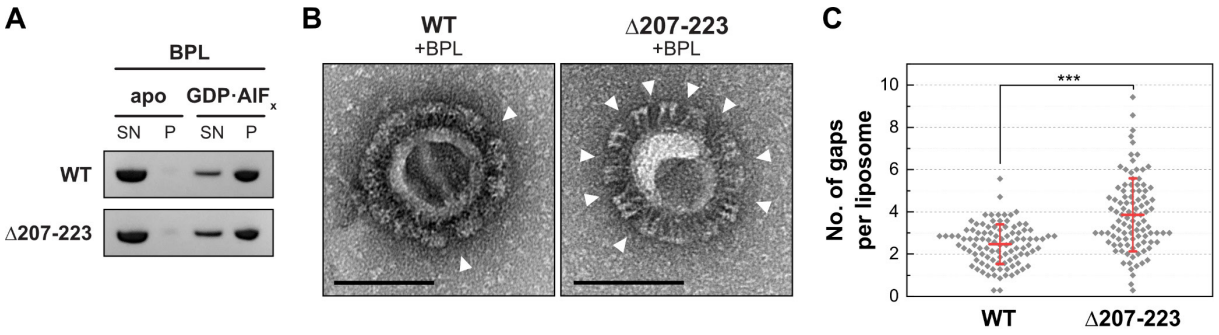

Figure 26. Coatomer formation of the polymerization-deficient Δ207-223 mutant. **(A)** Sedimentation assay in the presence of BPL liposomes. SN: supernatant. P: pellet. **(B)** Negative-stain TEM of GBP1-coated liposomes. Arrow heads indicate gaps within the patched protein coat. Scale bars are 100 nm. **(C)** Quantification of gaps within the protein coat per liposome (n=100) in negative-stain TEM micrographs in a blinded experiment. Data are averages from seven independent experimenters and are represented by mean ± SD. Significance was derived by an unpaired *t*-test. ***$P \leq 0.001$.

4.4 Helix α4' is crucial for GDP hydrolysis

Since GBP1 polymerization is dependent on GTP and GDP hydrolysis (Figure 24B) (Shydlovskyi et al., 2017), GTP binding affinities and GTPase activities were determined for the helix α4' mutants (see 3.3.9 and 3.3.10). Affinities of the helix α4' mutants for binding a non-hydrolysable, fluorescently labelled GTP analogue resembled that of wild-type GBP1 (Figure 27A). Furthermore, all helix α4' mutants retained their ability to hydrolyze GTP; however, GDP hydrolysis and thus GMP production was abolished for all of them (Figure 27B, D). Wild-type GBP1 showed a concentration-dependent increase in specific GTPase activity that can be explained with a dimerization-dependent, cooperative hydrolysis mechanism (Ghosh et al., 2006). The apparent K_d for wild-type GBP1 dimer formation was 1.9 µM with a maximum catalytic GTPase activity, k_{max} of 55.3 min^{-1}. The catalytic GTPase activity of the Δ207-223 variant was increased 1.7-fold compared to wild-type, presumably due to the lack of steric restrains within the dimer, while the apparent K_d of the mutant resembled that of wild-type (Figure 27C). Also, the GBP1 Δ207-213 and Δ207-216 variants retained a similar cooperative GTPase activity to wild-type GBP1 with a slightly reduced dimerization affinity (1.8-fold and 3.0-fold lower affinity for Δ207-216 and Δ207-213, respectively).

While full-length GBP1 cannot utilize GDP when provided as a substrate, but only from preceding GTP hydrolysis, the isolated LG domain lacking the auto-inhibiting GED shows GDP-induced dimerization and an increased GDPase activity (Ince et al., 2021). To explore why the helix α4' mutants produce less GMP than wild-type GBP1, assembly and GDPase activity of the isolated LG domains were determined (see 3.3.10 and 3.3.11). As expected, the wild-type LG domain eluted as a monomer in the absence of nucleotide (apo), but efficiently dimerized in the presence of GDP•AlF_x and GMP•AlF_x, mimicking the first and second GTP hydrolysis step, respectively (Figure 28A). Also, the α4' variants were monomeric in the apo state and dimerized in the presence of GDP•AlF_x. However, they did not form dimers in the presence of GMP•AlF_x (Figure 28A). When offering GDP as substrate, the α4' variant LG domain constructs showed a drastically reduced catalytic GDPase activity as compared to the wild-type LG (Figure 28B), even though the binding affinities toward mant-GDP resembled that of wild-type (Figure 28C). These data indicate that GTP-induced dimerization and the subsequent GTP hydrolysis is not affected by mutations in helix α4'. However, mutations in α4' promote LG dimer dissociation upon the first GTP hydrolysis step.

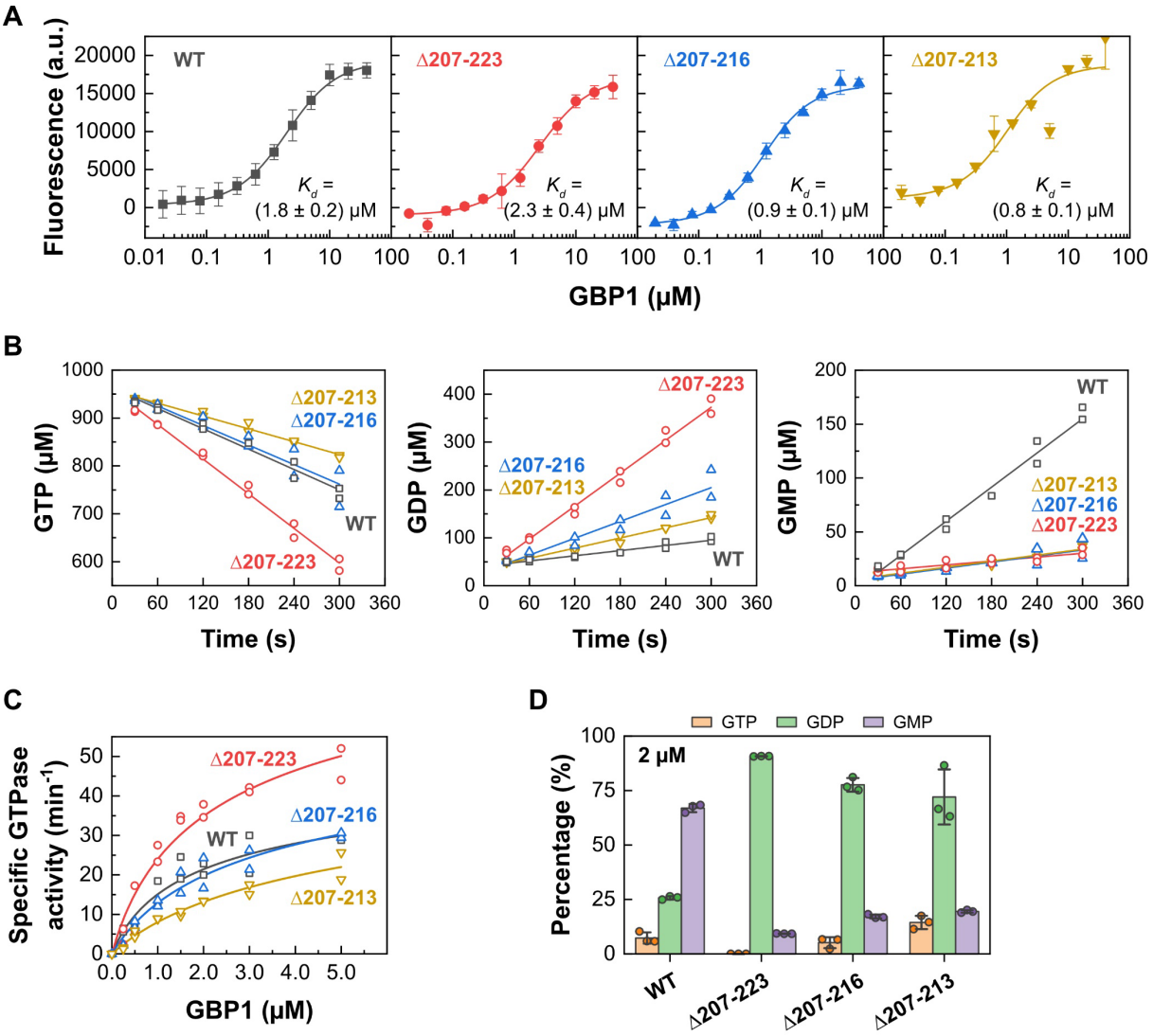

Figure 27. GTP binding affinities and GTPase activities of helix α4' variants. (A) Nucleotide binding. Fluorescence of mant-GMPPNP (0.5 µM) at varying GBP1 concentration for indicated constructs. Data points are averages from three independent experiments and are represented by mean ± SD. Equilibrium dissociation constants K_d were calculated by fitting a quadratic equation to data using eq. 3.6. WT data in Figure 27A, Figure 33C, Figure 35A are derived from the same experiments performed with all constructs in parallel and provided here for comparison. **(B)** GTP hydrolysis (left), GDP production (middle), and GMP production (right) of 2 µM wild-type GBP1 and respective helix α4' variants derived from two independent experiments. **(C)** Specific activity of cooperative GTP hydrolysis. Initial hydrolysis rates (n=2) were normalized to the protein concentration and plotted against protein concentration. Dimer dissociation constants, K_d, and maximum catalytic GTPase activities, k_{max}, were calculated by fitting a quadratic equation to data using eq. 3.7. **(D)** End product formation of GTP hydrolysis for GBP1 helix α4' constructs after 30 min (n=3, mean ± SD). WT data in Figure 27D, Figure 33B, Figure 35B are derived from the same experiments performed with all constructs in parallel and provided here for comparison.

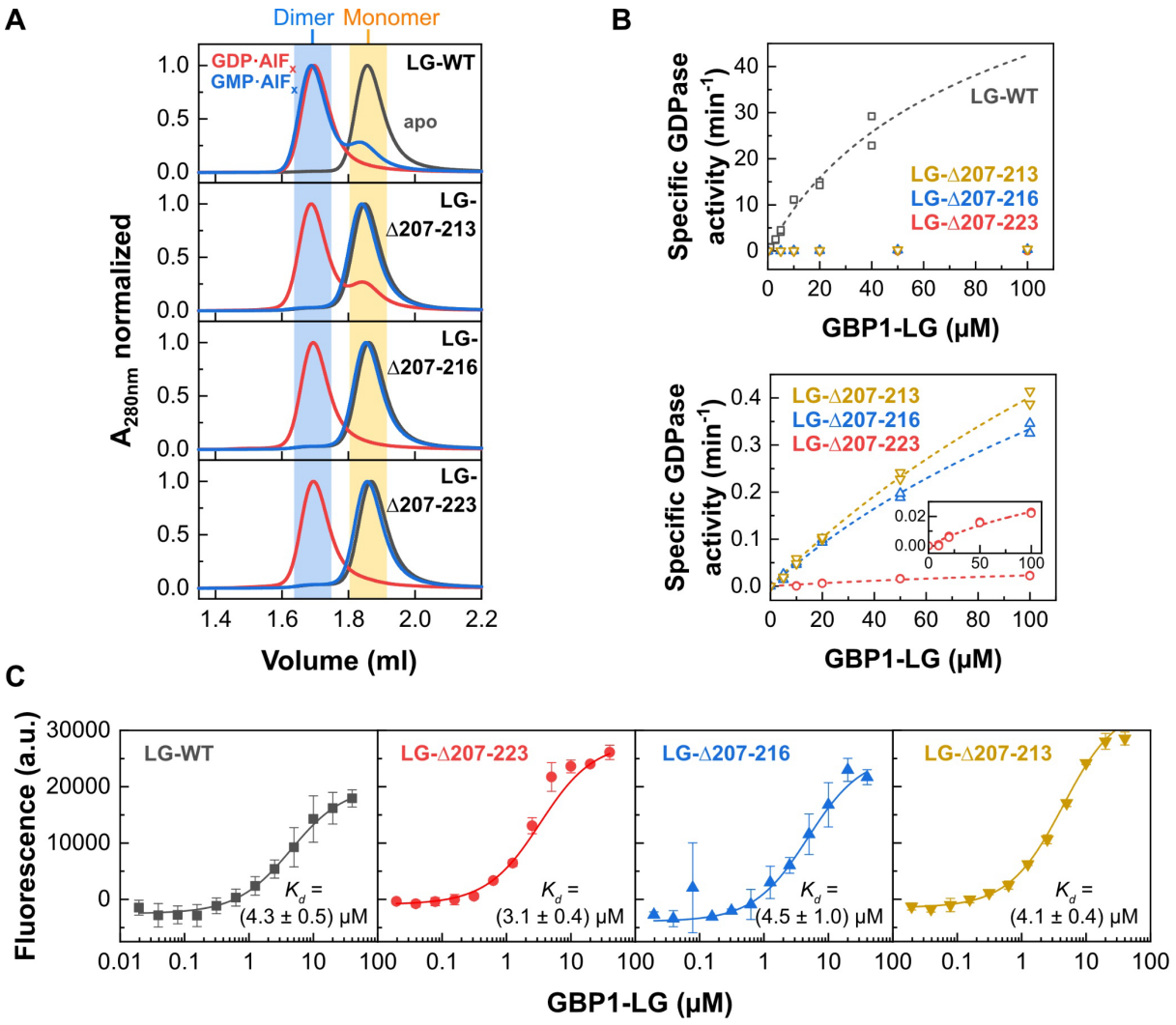

Figure 28. GDPase activities and GDP binding affinities of isolated LG domains for helix α4' variants. (A) Analytical size-exclusion chromatography of isolated LG domains. Dimeric fractions are highlighted in blue, monomeric fractions in yellow. **(B)** Specific activity of cooperative GDP hydrolysis of isolated LG domains. Initial hydrolysis rates (n=2) were normalized to the protein concentration and plotted against protein concentration. Upper panel: the dashed line represents a fit for WT using eq. 3.7 (K_d = 110 μM ± 50 μM, k_{max} = 120 min^{-1} ± 40 min^{-1}). Lower panel: dashed lines are a guide to the eye. **(C)** Nucleotide binding. Fluorescence of mant-GDP (0.5 μM) at varying GBP1 concentration for indicated isolated LG domain constructs, as described in the legend of Figure 27A.

4.5 Helix α4' is crucial for GBP1 binding to pathogenic bacteria

In fighting off bacterial invaders, GBP1 establishes a stable protein coat on the surface of bacteria (Kutsch et al., 2020; Piro et al., 2017). To characterize the biological relevance of helix α4', an *in vitro* binding assay of fluorescent labeled GBP1 to a gram-negative bacterial pathogen was performed in collaboration with Dr. Miriam Kutsch (Heinrich Heine University Düsseldorf), who performed the *in vitro* binding assays and analyses (see 3.3.12).

While wild-type GBP1 formed a stable protein coat around pathogenic *E. coli*, the mutants showed impaired capacity in encapsulating bacteria (Figure 29, Figure 30). For the Δ207-213 and Δ207-216 variants, binding to the surface of gram-negative bacteria was reduced and small protein spots on the bacterial surface instead of a continuous protein coat were observed at early time points (Figure 30). Even though the Δ207-223 variant was still able to bind to artificial liposomes (Figure 26), it completely failed to form a protein coat on pathogenic *E. coli*. Since

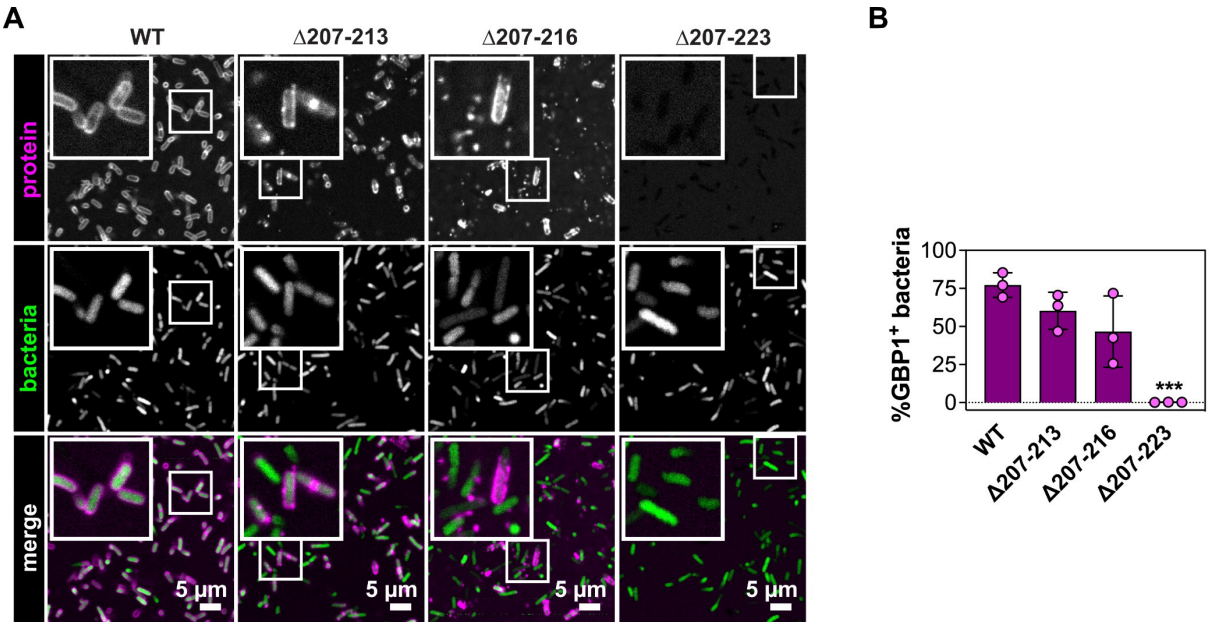

Figure 29. *In vitro* binding assay of GBP1 helix α4' variants. (A) Confocal microscopy images of fluorescent labeled wild-type GBP1 and helix α4' variants (magenta) targeting pathogenic *E. coli* (DSM1103) expressing eGFP (green). Representative WT images in Figure 29A, Figure 34C and Figure 36A are identical and derived from the same experiments performed with all constructs in parallel. **(B)** Quantification of GBP1-targeted (GBP1$^+$) bacteria in *in vitro* binding assay after 30 min. Graphs are averages from three independent experiments and are represented by mean ± SD. One-way ANOVA with Dunnett's multiple comparisons test comparing to GBP1 WT$^+$ bacteria was used, all statistically significant comparisons are shown. ***$P < 0.001$. WT data in Figure 29B, Figure 34D and Figure 36B are derived from the same experiments performed with all constructs in parallel and provided here for comparison. Experiment and analysis were performed by Dr. Miriam Kutsch (Heinrich Heine University Düsseldorf), with proteins provided by me.

the formation of soluble polymers is affected in these variants (Figure 24), not membrane binding per se, polymerization via the helix α4' interface seems to be a prerequisite for GBP1 binding to the surface of gram-negative bacterial pathogens and hence, for establishing an antimicrobial protein coat.

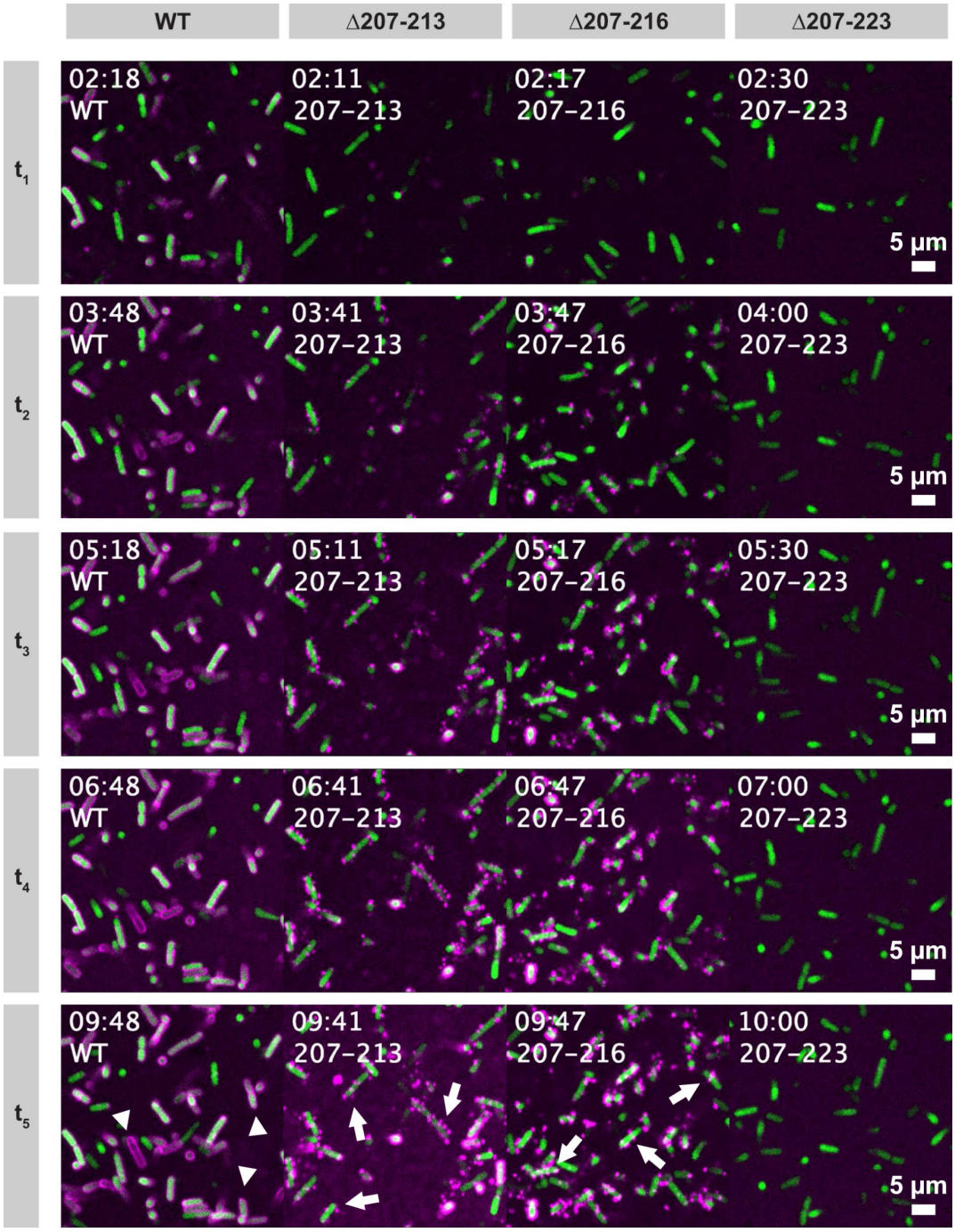

Figure 30. GBP1 binding to gram-negative bacterial pathogens over time. Time-lapse confocal microscopy of fluorescent labeled wild-type GBP1 and helix α4' variants (magenta) targeting pathogenic *E. coli* (DSM1103) expressing eGFP (green). Scale bars are 5 µm. Time points are in minutes. Arrow heads point to representative stable protein coats around bacteria; arrows point to representative single protein spots on the surface of bacteria. Experiments were performed by Dr. Miriam Kutsch (Heinrich Heine University Düsseldorf), with proteins provided by me.

4.6 A coordinated movement of helix α4' and helix α3 mediates nucleotide hydrolysis

Helix α4' has been identified to contribute to the oligomeric interface of GBP1 and undergoes structural rearrangement upon nucleotide hydrolysis, crucial for GDP hydrolysis and binding to pathogenic bacteria. This chapter focuses on how this structural rearrangement is coordinated within the LG domain and how oligomerization is related to this.

4.6.1 Re-analysis of nucleotide-dependent structural transitions

Further analyzing the nucleotide-dependent structural transitions of the GBP1 LG domain for the available nucleotide states (Ghosh et al., 2006; Prakash et al., 2000b), a coupled motion of helix α4' and the adjacent helix α3 was observed, while the latter of which contributes to the dimerization interface (Figure 31). This suggested that dimerization-dependent structural changes are coordinated between helices α3 and α4': while a coordinated α3-α4' movement was apparent upon GTP-induced dimerization from the apo to GMPPNP-bound state, helix α4' moves independently of helix α3 from the dimeric GMP•AlF_x- to the GMP-bound monomeric state. Instead, a simultaneous motion of helix α4' and the guanine cap was observed between the two states, hinting at a long-range conformational coupling of these two elements during GDP hydrolysis. Upon nucleotide release, helices α3-α4' simultaneously move back toward a closed conformation.

Analysis of these structural transitions further identified a salt bridge between Lys234 of the β6 strand and Asp199 located in helix α4, which may couple the motions of helix α4' with the guanine cap (Figure 31). This was reminiscent of a lever motion, with the salt bridge of Lys234-Asp199 acting as the pivot point.

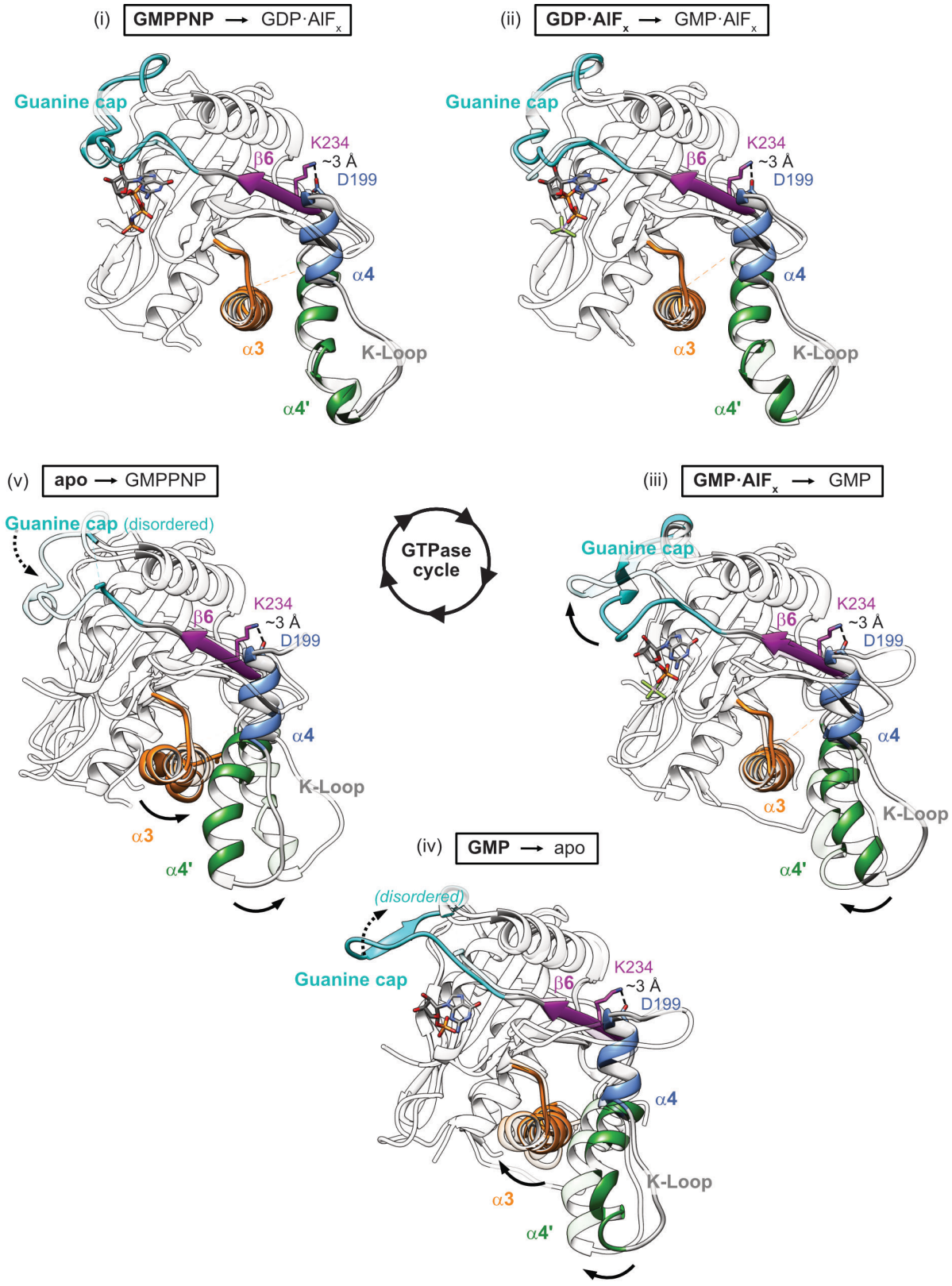

Figure 31. Nucleotide-dependent structural transitions in the GTPase cycle of GBP1. Transitions of structural elements of the GBP1 LG domain are visualized by superimposing **(i)** the GMPPNP-bound (PDB 2bc9) and GDP•AlF$_x$-bound state (PDB 2b92, transparent), **(ii)** the GDP•AlF$_x$-bound and GMP•AlF$_x$-bound state (PDB 2b8w, transparent), **(iii)** the GMP•AlF$_x$-bound and GMP-bound state (PDB 2d4h, transparent), **(iv)** the GMP-bound and apo state (PDB 1dg3, transparent), and **(v)** the apo and GMPPNP-bound state (transparent). The salt bridge between D199 and K234 is shown. Note that the guanine cap is disordered in the apo state.

4.6.2 Design and characterization of mutants interfering with the coordinated helix α3-α4' motion

Next, two mutants were designed to evaluate the hypothesis that dimerization-dependent structural changes are coordinated between helices α3 and α4'. One mutant should lock helix α4' to helix α3 in a closed state, as observed in the monomeric apo and GMP-bound states. The other mutant should lock helix α4' to helix α3 in a more open conformation, as in the dimeric GMP•AlF_x-bound, GDP•AlF_x-bound, and GMPPNP-bound conformations. For the locked state, Met139 in helix α3 was mutated into an aspartate which should form a new salt bridge to Arg223 within helix α4' (Figure 32). To stabilize helix α4' in an open state, Met139 was mutated into a glutamate which, due to its longer side chain compared to the aspartate, should introduce a greater distance between the helices. Additionally, by mutating Met139 into an arginine, a mutant was designed to unlock helix α3 and helix α4' due to repulsion with the opposing Arg223.

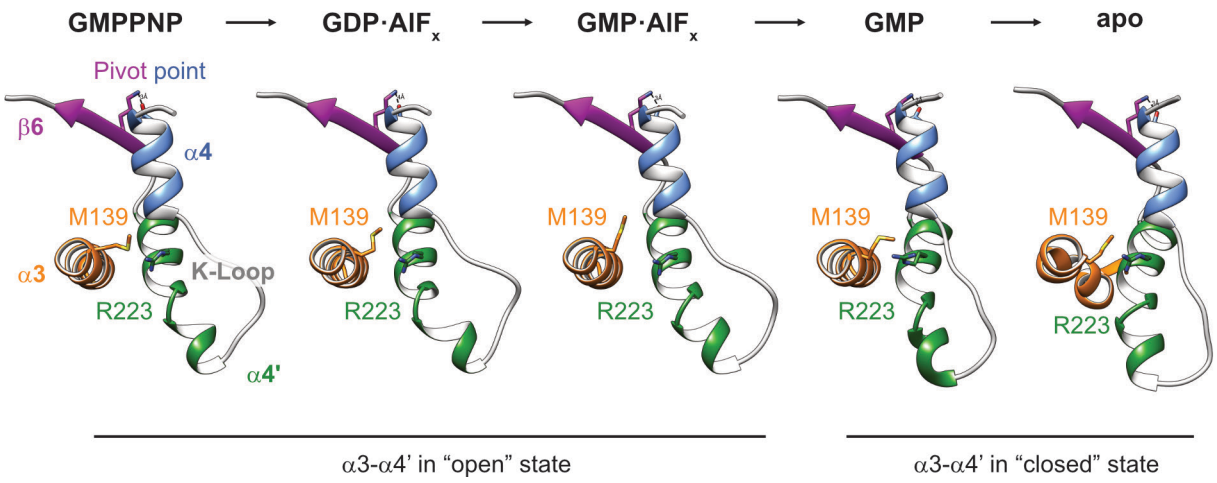

Figure 32. Coordinated helix α3-α4' movement in different nucleotide states. Structural rearrangement of helix α3 and α4' upon nucleotide hydrolysis are displayed and the salt bridge between D199 and K234 is shown (pivot point). PDB accession codes: GMPPNP (2bc9), GDP•AlF_x (2b92), GMP•AlF_x (2b8w), GMP (2d4h), apo (1dg3).

Analytical size-exclusion chromatography of the non-farnesylated mutants validated GDP•AlF_x-dependent locking of M139D in the monomeric state, while M139E was indeed able to dimerize (Figure 33A). Also, the M139R mutant dimerized, although with reduced efficiency. While all three mutants showed similar nucleotide affinities compared to the wild-type protein, GTP hydrolysis of M139D and M139E was completely abolished (Figure 33B, C);

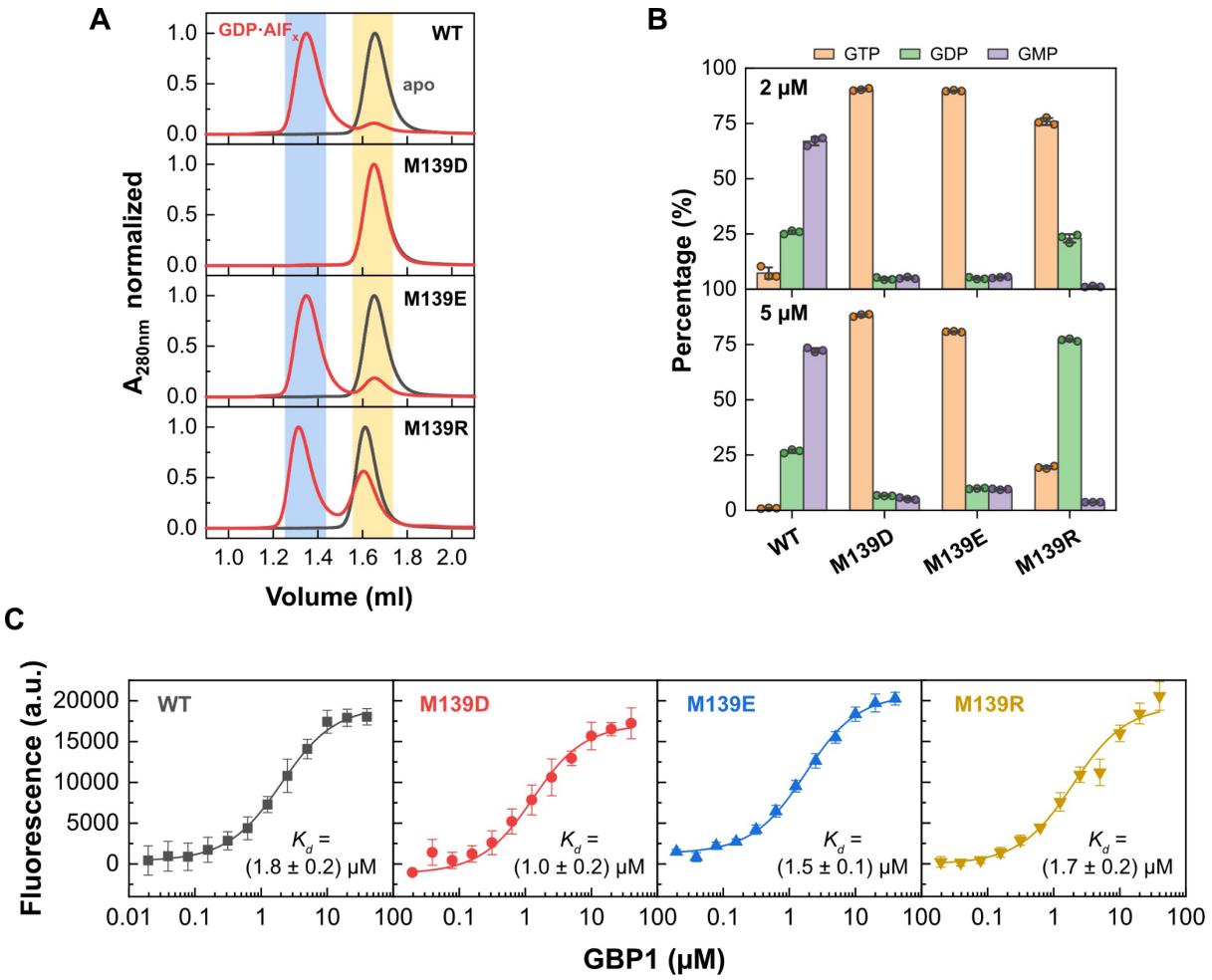

Figure 33. Characterization of mutants interfering with the coordinated helix α3-α4' motion. **(A)** Analytical size-exclusion chromatography of M139 mutants. Dimeric fractions are highlighted in blue, monomeric fractions in yellow. **(B)** End product formation of GTP hydrolysis for M139 mutants after 30 min (n=3, mean ± SD), as described in the legend of Figure 27D. **(C)** Nucleotide binding for M139 mutants. Fluorescence of mant-GMPPNP (0.5 µM) at varying GBP1 concentration for indicated constructs, as described in the legend of Figure 27A.

even though preventing the release of the GED by crosslinking to helix α4' still allowed for GTP but not GDP hydrolysis (Ince et al., 2021). The M139R mutant, however, hydrolyzed GTP but failed to hydrolyze GDP, suggesting a specific deficit in the second hydrolysis step.

Interestingly, in the farnesylated state, GDP•AlF$_x$-dependent dimerization and higher order oligomerization of the dimerization-capable mutants M139E and M139R were blocked (Figure 34A, B). Accordingly, these mutations also abolished binding to pathogenic *E. coli* and prevented the formation of a stable protein coat (Figure 34C, D). When the coordinated α3-α4' motion is hindered as in the designed Met139 mutants, it appears that farnesylated GBP1 fails

to adopt an open conformation, and thus, oligomerization and coatomer formation are prevented. A correctly coordinated α3-α4' motion is therefore required for releasing the farnesyl-stabilized GED from helix α4' (Figure 25), allowing GBP1 to fulfill its biological function in innate immunity.

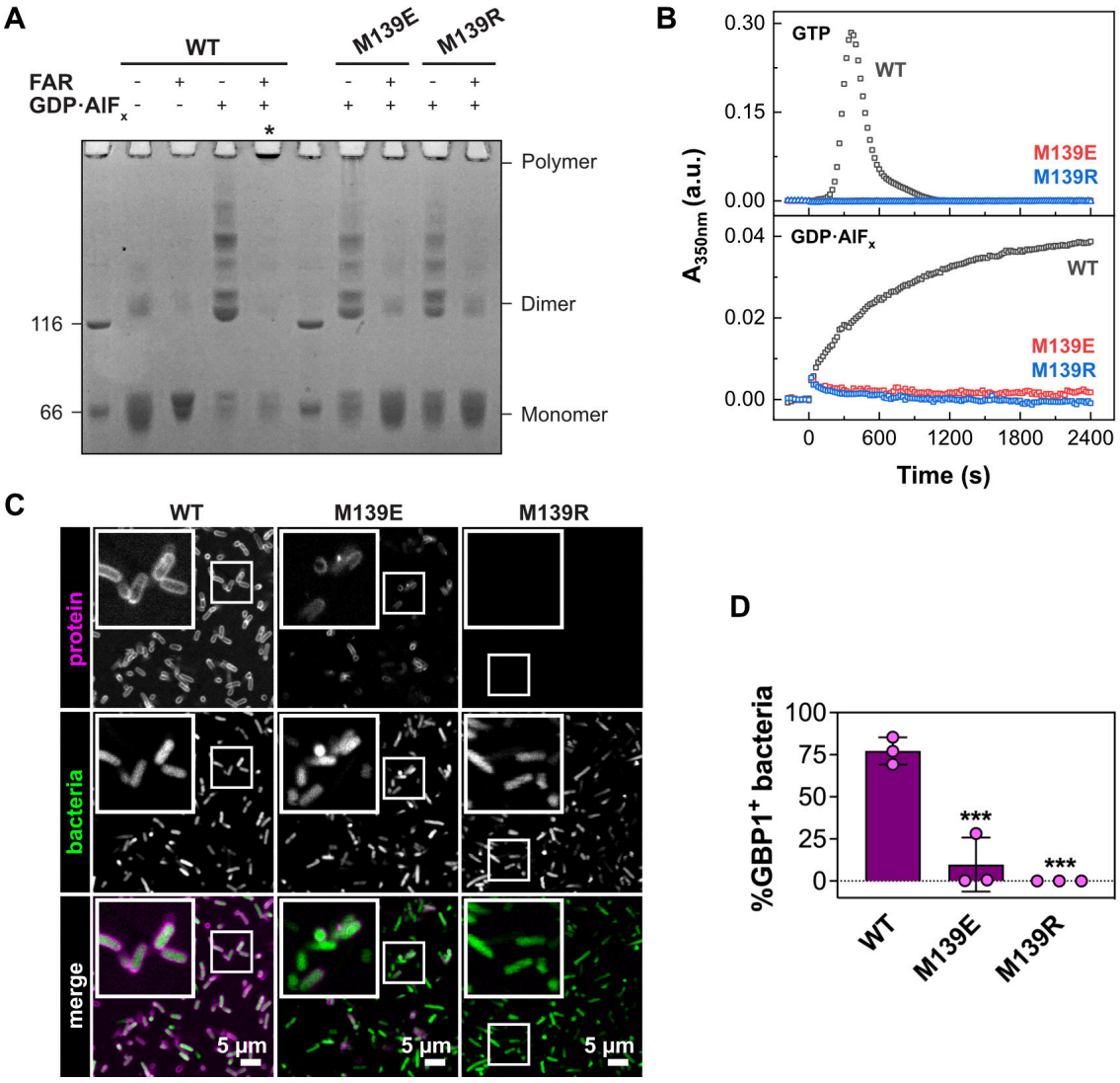

Figure 34. Oligomerization of dimerization-capable M139 mutants. (A) Crosslinking assay of M139 mutants. The respective oligomeric states based on molecular weight are indicated. Asterisks indicate successful polymerization. FAR: farnesylated. **(B)** Light scattering-based polymerization assay of M139 mutants. Polymerization is induced by GTP (top) and GDP•AlF$_x$ (bottom). WT data is the same as shown in Figure 24B and provided here for comparison. **(C)** Confocal microscopy images of wild-type GBP1 and M139 mutants targeting pathogenic *E. coli*, as described in the legend of Figure 29A. **(D)** Quantification of GBP1-targeted bacteria in *in vitro* binding assay, as described in the legend of Figure 29B. Experiment and analysis in (C) and (D) were performed by Dr. Miriam Kutsch (Heinrich Heine University Düsseldorf), with proteins provided by me.

4.6.3 Design and characterization of mutants interfering with the lever motion

To study the potential lever motion and explore a possible function of the pivot point, the salt bridge between Lys234 and Asp199 was disrupted by mutating the Asp199 to either an alanine or lysine. Although there was no significant difference in nucleotide affinity (Figure 35A), both mutations led to a dramatic reduction in GTP hydrolysis and GMP production as compared to wild-type (Figure 35B). The mutants showed strongly reduced polymerization upon GTP addition, while dimerization and polymerization for GDP•AlF_x-

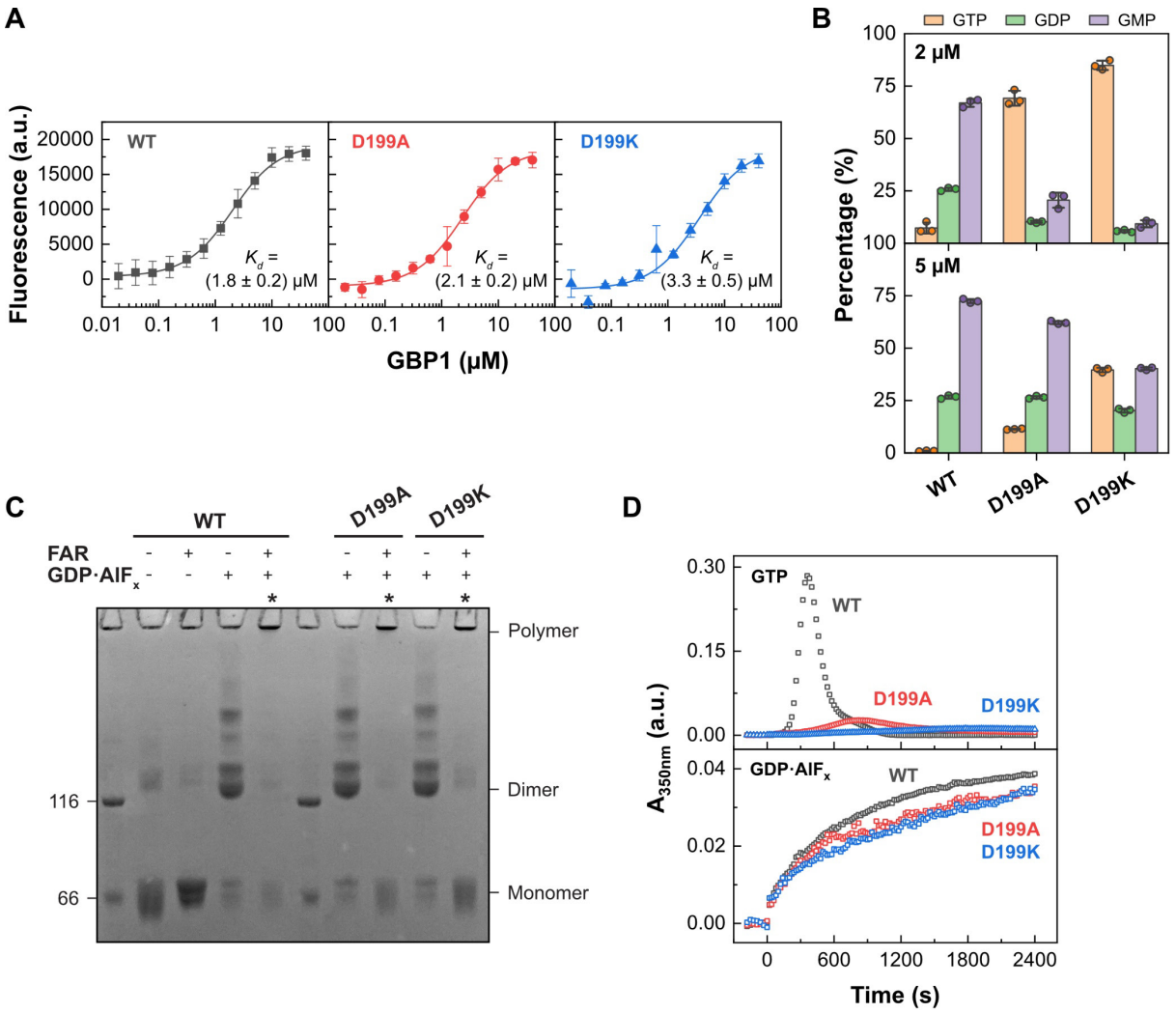

Figure 35. Characterization of mutants interfering with the lever motion. (A) Nucleotide binding for D199 mutants. Fluorescence of mant-GMPPNP (0.5 µM) at varying GBP1 concentration for indicated constructs, as described in the legend of Figure 27A. **(B)** End product formation of GTP hydrolysis for D199 mutants after 30 min (n=3, mean ± SD), as described in the legend of Figure 27D. **(C)** Crosslinking assay of D199 mutants. The respective oligomeric states based on molecular weight are indicated. Asterisks indicate successful polymerization. FAR: farnesylated. **(D)** Light scattering-based polymerization assay of D199 mutants. Polymerization is induced by GTP (top) and GDP•AlF_x (bottom). WT data is the same as shown in Figure 24B and provided here for comparison.

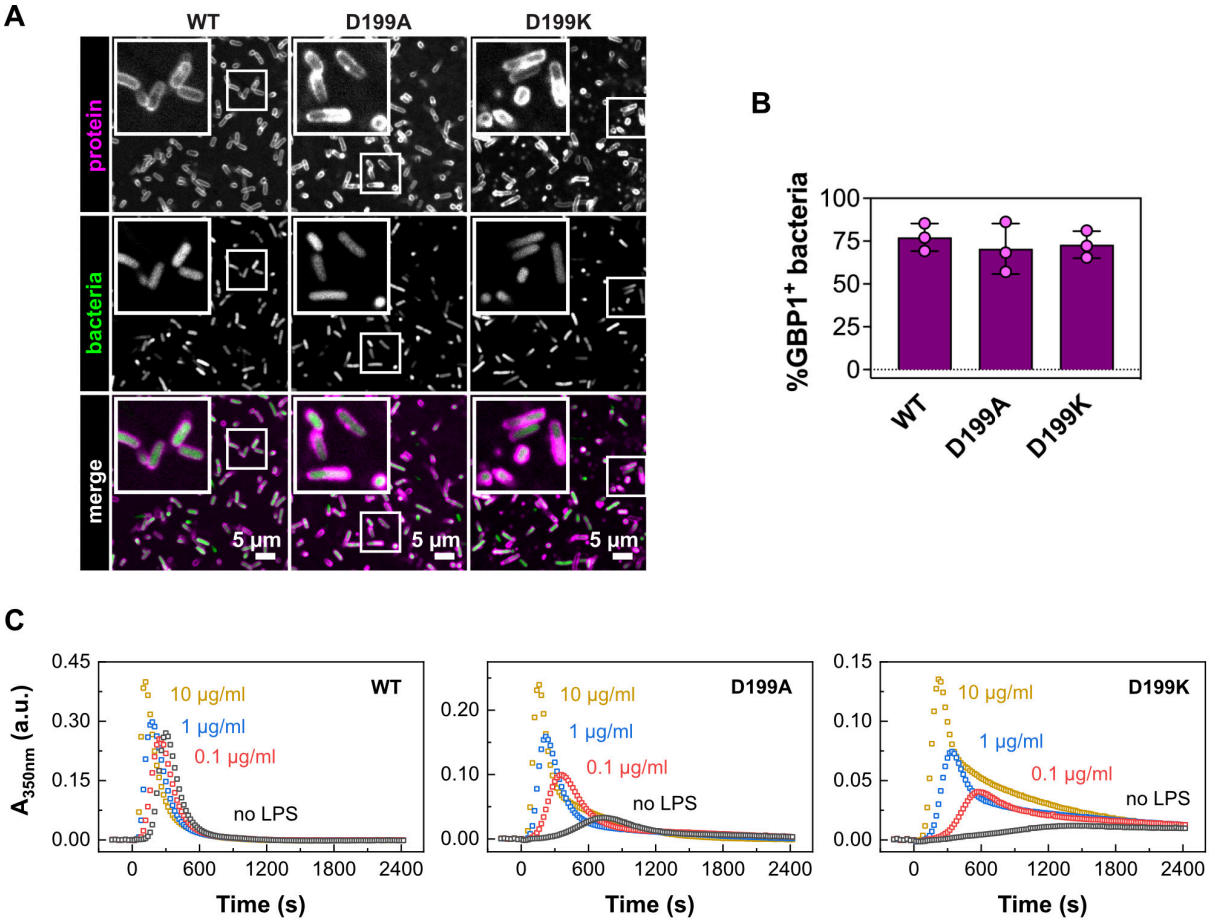

Figure 36. Oligomerization of pivot point mutants. (A) Confocal microscopy images of wild-type GBP1 and D199 mutants targeting pathogenic *E. coli*, as described in the legend of Figure 29A. **(B)** Quantification of GBP1-targeted bacteria in *in vitro* binding assay, as described in the legend of Figure 29B. Experiment and analysis in (A) and (B) were performed by Dr. Miriam Kutsch (Heinrich Heine University Düsseldorf), with proteins provided by me. **(C)** Light scattering-based polymerization assay of pivot point mutants in presence of lipopolysaccharide (LPS). Polymerization is induced by GTP and promoted by LPS.

induced assembly were not restricted (Figure 35C, D), indicating that the oligomeric interface via helix α4' can still be established. In support of this hypothesis, the pivot point mutants encapsulated pathogenic *E. coli* with similar efficiencies as wild-type GBP1, suggesting that LPS present on the bacterial surface stabilizes GBP1 oligomerization (Kutsch et al., 2020) (Figure 36A, B). In line with this observation, addition of LPS facilitated GTP-induced polymerization of the pivot point mutants in a concentration-dependent manner (Figure 36C).

Together, these findings and the published structural data suggest that the nucleotide-loading status of the LG domain coordinates movements of the guanine cap and/or helix α3-α4' via a pivot point, allowing GBP1 oligomerization.

5 Discussion

In this study, new and previously described structural data of GBP1 have been synthesized with biochemical and mechanistic experiments to characterize GBP1's biological function in innate immunity and elucidate the activation mechanism for GBP1 oligomerization. By assembling into large polymers and a membrane-bound protein coat, GBP1 plays a crucial role in the innate immune response against microbial pathogens. The peripheral helix α4' in the large GTPase (LG) domain was proven to be decisive in establishing the oligomeric interface and facilitating the formation of an antimicrobial protein coat. Results of this thesis reveal that coordinated movements of structural elements in the LG domain of GBP1 are a prerequisite for a nucleotide-driven activation mechanism allowing oligomerization and membrane binding.

In the following, the architecture of the oligomeric GBP1 building blocks is discussed in regard to published biophysical and structural data. By combining existing and new structural and functional information derived from this thesis, a model for a nucleotide-driven activation mechanism in GBP1 is proposed. In particular, the prominent role of helix α4' of the large GTPase domain is discussed. Furthermore, the importance of LPS in facilitating and stabilizing GBP1 assembly is elucidated and the role of the nucleotide-driven activation mechanism as a regulatory safeguard in GBP-mediated host defense is emphasized. To conclude, perspectives for future GBP research are discussed.

5.1 Outstretched, dimeric GBP1 as the oligomeric building block

To date, human GBP1 has been associated with various host defense processes to defeat bacterial infections. It has been shown that GBP1 oligomerization into soluble polymers boosts the release of LPS and triggers caspase-4 activation resulting in pyroptosis (Dickinson et al., 2023; Goers et al., 2023). By establishing an antimicrobial coat on intracellular gram-negative bacteria, GBP1 breaks down the integrity of the bacterial surface, which promotes antimicrobial peptide-mediated lysis, blocks actin-driven dissemination, and might provide a platform for caspase-4 activation (Kutsch et al., 2020; Piro et al., 2017; Santos et al., 2020; Wandel et al., 2017; Zhu et al., 2024). On a structural level, monomeric GBP1 exhibits a closed auto-inhibited state and shows no antimicrobial activity. Its decisive role in mediating innate immune responses to fight off invading cytosolic bacteria relies on its ability to form large protein

assemblies. However, structural insights into the architecture of these macromolecular complexes are missing and it has not yet been examined how single building blocks interact with each other and stabilize the oligomeric conformation.

What is structurally known about GBP1? After the crystal structure of monomeric full-length GBP1 was described (Prakash et al., 2000a), structural investigations of the isolated large GTPase (LG) domain of GBP1 revealed for the first time its dimeric conformation in different nucleotide-loading states (Ghosh et al., 2006). A deeper understanding of how GBP1 dimerizes and forms oligomers was achieved through a set of elaborated FRET experiments and the previous observation of soluble GBP1 polymers in negative-stain transmission electron microscopy (Ince et al., 2017; Shydlovskyi et al., 2017; Sistemich et al., 2021; Sistemich et al., 2020). The focus of these experiments was mainly set on the GTP hydrolysis-dependent conformational changes in GBP1 and its membrane-binding ability. The GED which in the nucleotide-free monomer is bound to the LG domain was shown to prevent dimerization via the G interface (Vopel et al., 2010). Together, a model for GBP1's oligomerization mechanism was proposed in which GBP1 cycles between a closed and open conformation and the opened GBP1 dimer is incorporated in the polymer. The crystal structure of the GBP5 dimer lacking the GED (GBP5-ΔGED) extended this model by showing that the MDs undergo large structural rearrangements and dimerize in a crisscrossed fashion forming another dimerization interface (Cui et al., 2021). Cryo-EM studies on full-length GBP1 underpinned this crisscrossed dimeric conformation (Kuhm et al., 2023). However, due to high flexibility of the GED further information on the full-length dimeric conformation could not be obtained. Based on these new findings, a model for GBP1's oligomerization mechanism evolved but was still missing important features: what is the architecture of GBP1's oligomeric states? How are they stabilized and what part of GBP1 contributes to the oligomeric interface?

In this work, structures for both the membrane-bound and polymeric state were obtained by cryo-electron microscopy. The results of cryo-ET data presented here demonstrate that human GBP1 binds to lipid membranes in an open, outstretched conformation (Figure 19). Within the coatomer, the overall shapes of the LG domain and MD match well with the recently published crystal structure of the GBP5 dimer (Cui et al., 2021) and the cryo-EM structure of the GBP1 dimer in complex with GDP•AlF_x (Kuhm et al., 2023). In both dimeric structures, the MDs move by 30° via the hinge region and cross each other. In relation to the data presented here, this suggests that the coatomer is comprised of dimeric building blocks with crisscrossed MDs that are extended by elongated GEDs. The GEDs extend in parallel toward the membrane

surface, allowing the C-terminal farnesyl moiety to insert into the lipid bilayer. The observed conformation is in accordance with the theoretical dimension of outstretched GBP1 and with previous biophysical and structural studies predicting an upright orientation of GBP1 on membranes (Sistemich et al., 2021), and within soluble polymers (Peulen et al., 2023; Shydlovskyi et al., 2017; Sistemich et al., 2020). In the absence of lipid membranes, outstretched GBP1 dimers polymerize into planar disk-like structures of 30 building blocks (Figure 20). Polymeric disks, in turn, might stack into larger tubular structures, as also reported recently (Shydlovskyi et al., 2017; Sistemich et al., 2020). The observed preference of membrane-independent oligomerization for Folch liposomes versus BPL may reflect the consumption of soluble oligomers at the expense of coatomers in the presence of BPL liposomes. Together with the observed rare binding events of GBP1 polymers to BPL liposomes (Figure 16), these findings might correlate with a recent model by Kutsch et al. (2020) proposing that GBP1 must assemble into soluble oligomers first, in order to "drill" into the O-antigen layer of gram-negative bacteria, bind to the bacterial outer membrane, and establish a stable protein coat.

Results of this thesis demonstrate that these oligomeric structures are stabilized via lateral interactions of the LG domains between two dimeric GBP1 building blocks. In the monomeric state, this newly identified interface is blocked by the GED suggesting an auto-inhibiting mechanism in which the GED prevents both the formation of the G interface and the oligomer interface. Based on what is known from the previous literature and the here described new insights, the model of GBP1 oligomerization could be extended as follows (Figure 37): monomeric GBP1 is in an auto-inhibited state. GTP binding triggers the formation of dimers via the G interface which further assemble into oligomeric building blocks. The oligomeric

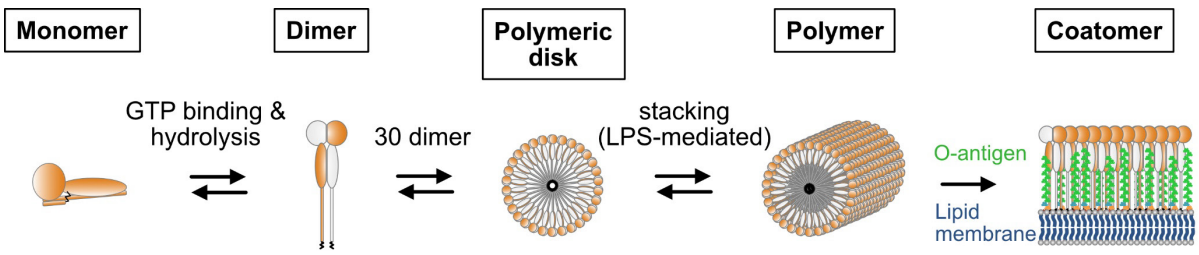

Figure 37. Model of GBP1 oligomerization. Monomeric GBP1 is auto-inhibited and adapts an open, outstretched dimeric conformation upon GTP binding and hydrolysis. Activated dimers assemble into a soluble 30-mer with the LG domains facing outwards and the farnesyl moieties in the center. Mediated by LPS, polymeric disks stack into polymeric structures. GBP1 polymers bind to lipid membranes and establish a dense protein coat which is stabilized by LPS on the surface of gram-negative bacteria.

building blocks are outstretched dimers that form upon GTP hydrolysis. They assemble into a soluble 30-mer, the polymeric disk. These disks are the building blocks for macromolecular structures. Assembly of polymers and the membrane-bound coatomer is mediated by interactions between two LG domain dimers and is facilitated and stabilized by LPS.

When we compare GBP1 to other members of the dynamin superfamily, the outstretched, dimeric GBP1 conformation with crisscrossed MD-GED is not surprising (Figure 38). For dynamin, a large-scale rearrangement of the bundle signaling element (BSE) was observed from the closed nucleotide-free to the open GTP-bound state (Anand et al., 2016; Chappie et al., 2011). The oligomeric building blocks of dynamin are crisscrossed stalk dimers; however, dimerization of the building blocks is particularly mediated through the stalk interface without involvement of the GTPase domains. The GBP1 conformations rather resemble those of the closely related atlastin family (Bian et al., 2011; Byrnes et al., 2013; Byrnes and

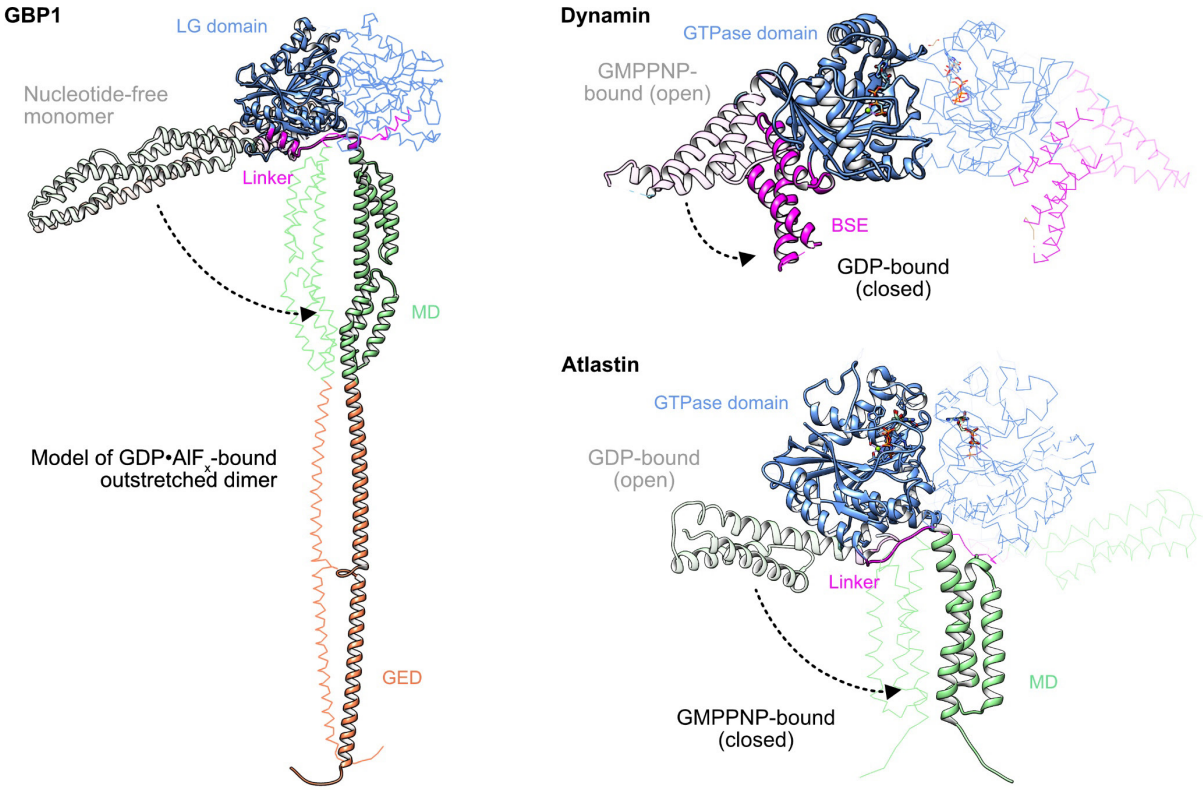

Figure 38. Structural rearrangements of dynamin superfamily proteins. Structures were superimposed on their GTPase domains. Nucleotide-free (GBP1) and open states (dynamin, atlastin) are opaque. The second protomer and the GTPase domains of the nucleotide-free (GBP1, opaque) and open states (dynamin, atlastin, both opaque) are displayed in wires. PDB-IDs: 1dg3 (GBP1, nucleotide-free), 8r1a (model of outstretched GBP1 dimer, this study), 3zyc (dynamin, GMPPNP), 5d3q (dynamin, GDP), 3q5e (atlastin, GDP), 4idp (atlastin, GMPPNP). LG: large GTPase, MD: middle domain, GED: GTPase effector domain, BSE: bundle signaling element.

Sondermann, 2011). The two GEDs of the GDP-bound atlastin dimer point away from each other while the GTPase domains establish the G interface. This is reminiscent of the dimeric full-length GBP1 model in complex with GMPPNP (Ghosh et al., 2006). In the GMPPNP-bound state, the GEDs of atlastin move from a rather horizontal position (open state) to a vertical position (closed state) and cross over via a linker region upon nucleotide binding and hydrolysis (Byrnes et al., 2013). This parallel conformation of the GEDs forms a new dimeric interface, as also shown in the GBP5 and GBP1 structures (Cui et al., 2021; Kuhm et al., 2023). Using small-angle X-ray scattering experiments (SAXS), Cui et al. (2021) proposed a conserved dimeric assembly for GBPs in which the GEDs fold back to the LG domain of the opposing protomer. Cryo-ET data presented here suggest an elongated dimer with outstretched GEDs which is contradictory to this model, but it is supported by cryo-EM data of the GBP1 dimer in which the GEDs are disordered (Kuhm et al., 2023). As shown by Peulen et al. (2023), nucleotide-free GBP1 has a high intrinsic flexibility, particularly in the absence of a farnesyl anchor. Together with SAXS data presented in the mentioned study, this raises the question of whether GBPs might form additional transient intermediate structures not directly accessible to structural analyses.

Parallel studies to this work on soluble GBP1 polymers and the coatomer further support the model of outstretched GBP1 as the oligomeric building block (Kuhm et al., 2023; Zhu et al., 2024). In both studies, the high flexibility of GBP1 building blocks prevented high resolution information of its assemblies, as is the case in the oligomeric structures described here. While Kuhm et al. (2023) used a similar approach with a simple membrane model system and the GTP hydrolysis state analogue GDP•AlF_x, Zhu et al. (2024) studied the coatomer on genetically modified *Salmonella* minicells and the natural substrate GTP. In this approach, the authors propose a dynamic GBP1 dimer model with monomeric GBP1 as building blocks (Figure 39). Unlike in this thesis, Zhu et al. (2024) performed STA with a tight dimeric and monomeric mask focusing on a single building block molecule. The membrane-bound structure described here used a rather wide mask to display the overall architecture of the coatomer with several building blocks present. This approach allowed general conclusions on how GBP1 building blocks interact with each other but might omit information on a single building block level. However, the outstretched dimer model of this thesis matches very well with the proposed monomeric map described by Zhu et al. (2024). Based on the presented data, it is thus more likely that dimeric rather than monomeric GBP1 are the oligomeric building blocks. Nevertheless, their dimeric map indicated an orientation of GBP1 different from that described

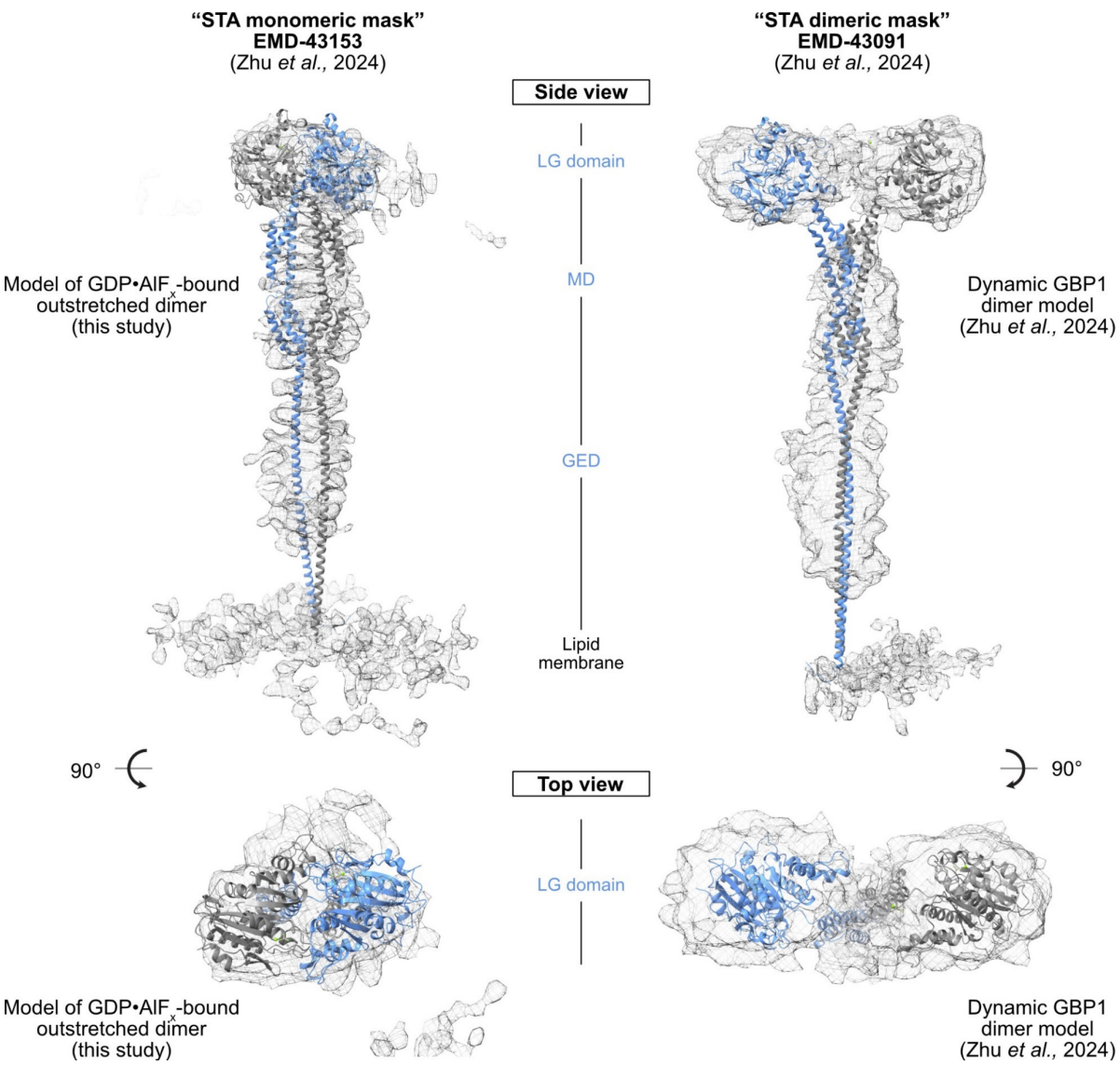

Figure 39. Comparison of GBP1 coatomer models. Subtomogram averaging maps by Zhu et al. (2024) using a "monomeric" and "dimeric" mask are shown. Left: The model of the outstretched dimer of this thesis was fitted into the density of their monomeric map. Right: Protomers of the outstretched dimer model were fitted separately into the dimeric map resembling the dynamic GBP1 dimer model by Zhu et al. (2024). Note that the MDs and GEDs clash in this fit.

here: while MDs and GEDs might still interact, the LG domains point in opposite direction (Figure 39). It is uncertain if these observations are simply the result of different subtomogram averaging strategies and limited resolution, or if they arose from the different sample conditions. The use of *Salmonella* minicells and GTP as natural substrate could have provided a more native glimpse at the dynamics of the GBP1 coatomer. It might describe possible rearrangements in the oligomeric building blocks following GTP hydrolysis/assembly. This

would resemble the structural rearrangements in the hydrolysis-dependent powerstroke of dynamin during membrane fission events (Chappie et al., 2011; Ganichkin et al., 2021). However, the available data do not yet allow any conclusions to be drawn about biological relevance. Hence, high-resolution structural details on such a dynamic macro-molecular machine remain the subject of future research.

5.2 Nucleotide-driven activation mechanism in GBP1

The cryo-ET and cryo-EM structures of membrane-bound and polymeric GBP1 obtained in this thesis not only revealed outstretched, dimeric GBP1 as the oligomeric building block, but also provided first insights in the oligomeric interface between peripheral regions of the LG domain dimer. In this study, helix α4' has been identified to contribute to this interface. It has further been shown that helix α4' participates in nucleotide-dependent coordinated movements in the LG domain. The here presented data and the available structural and functional information of GBP1 thus provide the molecular basis for a nucleotide-driven activation mechanism governing the motions of helix α4', helix α3, the guanine cap, and the GED, thereby coordinating the nucleotide-loading state with oligomerization and membrane binding (Figure 40).

Nucleotide-free GBP1 exists in an auto-inhibited, monomeric form where the GED is locked to helix α4' in a closed conformation and the farnesyl moiety is inaccessible (Ji et al., 2019; Prakash et al., 2000a). The guanine cap is in an open conformation, whereas helix α4' is in a locked conformation, thereby blocking the G interface in the LG domain (Prakash et al., 2000a). GTP-binding to GBP1 induces a simultaneous closing of the guanine cap and a coordinated opening of helix α3-α4', like a forward lever motion via the identified pivot point in the LG domain. These conformational changes allow for LG domain dimerization and GTPase activation (Ghosh et al., 2006; Prakash et al., 2000b; Wehner et al., 2012). At the same time, helix α4' pushes the GED away from the LG domain thereby releasing the farnesyl moiety from its pocket and facilitating the crisscross arrangements of the stalks (Cui et al., 2021; Ghosh et al., 2006; Ince et al., 2021; Kuhm et al., 2023; Sistemich et al., 2020; Vopel et al., 2010). The farnesyl moiety can insert into the membrane (Britzen-Laurent et al., 2010), while helix α4' is available to form a stable oligomeric interface via the LG domains. GTPase-induced movements of helix α4' between the GMPPNP- and GDP•AlF_x-bound X-ray structures are rather minor, yet may further promote the GTP hydrolysis-dependent oligomerization via helix

α4’ (Ghosh et al., 2006; Shydlovskyi et al., 2017). Following GDP hydrolysis, the GBP1 dimer dissociates in the GMP-bound state concomitant with an opening of the guanine cap and a partial closing of helix α4’, while helix α3 remains in an open conformation. Upon nucleotide dissociation, helix α3 and α4’ synchronously move back toward a closed conformation, which describes a backward motion of the lever arm.

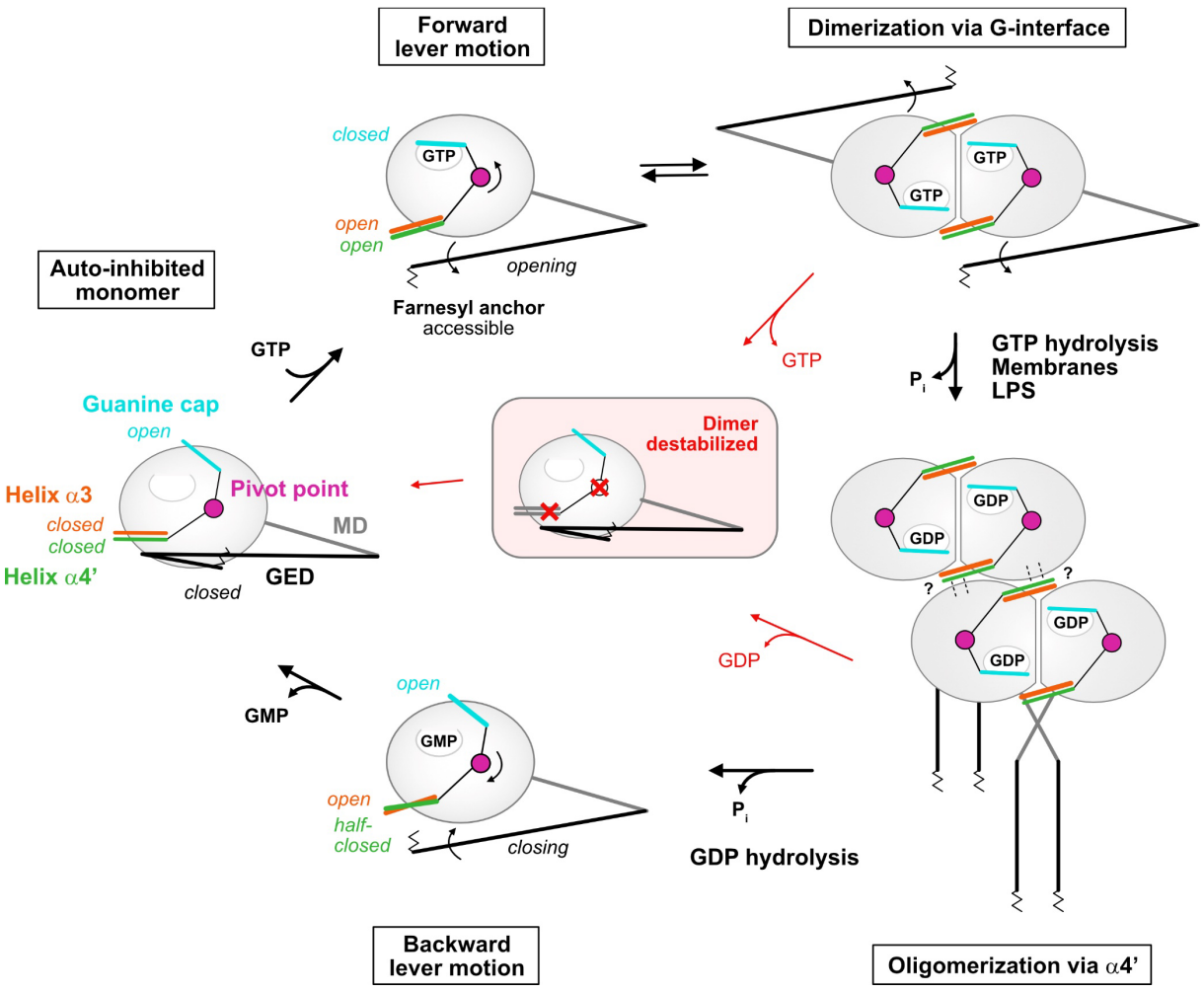

Figure 40. Model of the nucleotide-driven activation mechanism in GBP1. GTP-binding induces a simultaneous closing of the guanine cap and a coordinated opening of helix α3-α4’ via the salt bridge D199-K234 (pivot point), allowing LG dimerization and GTPase activation. Helix α4’ motion releases the GED from the LG and the farnesyl moiety becomes accessible. GBP1 dimerizes in a crisscrossed conformation and lateral LG interactions via helix α4’ build the oligomeric interface. Dimeric GBP1 in an outstretched conformation is the building block of higher-ordered assemblies. 30 dimers assemble into planar polymeric disks that stack into large soluble polymers. Polymers are required to establish a protein coat (coatomer) on bacterial pathogens. Following GDP hydrolysis, GBP1 dimers dissociate, the guanine cap opens, and helix α4’ partially closes. Upon nucleotide dissociation, helix α3 together with helix α4’ take a closed conformation. Interference with the overall lever motion or impairing the lever arms destabilizes the GBP1 dimer leading to dimer dissociation. LG: large GTPase, MD: middle domain, GED: GTPase effector domain.

By interfering with the lever motion or impairing the lever arms, the GBP1 dimer is destabilized and dissociates. It appears that in these cases the overall lever motion between the guanine cap and the combined motion of helix α4' and helix α3 is decoupled. Both helices are in proximity with the dimer interface and likely destabilize the GTP-bound GBP1 dimer, abrogating GTPase activation and thus affecting oligomerization. Impairing the lever arm, e.g., by altering helix α4' in the Δ207-223, Δ207-216, and Δ207-213 mutants, by unlocking helices α3-α4' in the M139R mutant, or by covalently locking the GED to helix α4' (Ince et al., 2021), abolishes GMP production. As these constructs interfere with the interplay between helix α4' and α3, the lever mechanism via the pivot point might still allow for GTPase activation, but the GDP-bound dimer is destabilized. Accordingly, dimer dissociation is favored over consecutive GDP hydrolysis.

5.3 The role of helix α4' of the large GTPase domain

In the proposed activation mechanism, the central role of helix α4' of the LG domain is striking. Results of this structure-function approach demonstrate its significance for the assembly of GBP1 dimers into polymeric structures and formation of a uniform protein coat on lipid membranes. In nucleotide-free GBP1, the GED folds back, interacts with parts of helix α4', and stabilizes the closed monomeric state (Figure 25). The interaction of helix α4' with the GED not only prohibits the establishment of the G interface, but also covers the newly identified oligomerization interface. Although the resolution of the presented cryo-ET and cryo-EM structures limit detailed structural analysis, the generated constructs clearly demonstrate that the oligomeric interface is formed via parts of helix α4'. Structural and biochemical data suggest that these lateral LG domain interactions observed in the membrane-bound coatomer may also stabilize interactions within soluble polymers. The oligomeric interface via helix α4' therefore appears to be uniformly structured in both GBP1's oligomeric states. Hence, helix α4' has multiple functions in the GTPase cycle of GBP1: preventing LG dimerization and GED opening in the nucleotide-free auto-inhibited state, while it promotes GED opening and allows LG domain dimerization and oligomerization in the activated state.

5.4 LPS-stabilized assembly mechanism of GBP1

As reported, polymeric GBP1 directly binds to lipopolysaccharide (LPS) and transitions into an LPS-stabilized protein coat on the bacterial surface (Kutsch et al., 2020). Severely weakening the lateral interactions via helix α4', thus abolishing its polymerization as in the Δ207-223 variant, completely prevented encapsulation of gram-negative bacteria. When restricting the assembly of higher-ordered polymers but not the formation of polymeric disks, as in the Δ207-213, Δ207-216 variants and the pivot point mutants, GBP1 still established a coatomer on pathogens. This might be explained by an LPS-stabilized assembly mechanism of higher-ordered polymers on the surface of the pathogens (Dickinson et al., 2023; Kutsch et al., 2020), which also compensates for the reduced oligomerization efficiency of the pivot point mutants. The here provided pivot point mutants can therefore contribute to the study of the O-antigen specificity of GBP1 and should be tested for their ability to encapsulate bacterial strains with different LPS compositions.

LPS facilitates and stabilizes the assembly of GBP1. This might explain the limited resolution in the cryo-ET and cryo-EM data due to high flexibility of GBP1, in particular its helical GED. To understand the complex mechanism in how GBP1 interacts with LPS more detailed *in vitro* and *in situ* biophysical and structural studies are required. It would be of interest to visualize the interaction of GBP1 polymers with lipid membranes (as shown in Figure 16) and with the O-antigen layer on artificial liposomes and bacteria. Initial data from Kuhm et al. (2023) indicate that studying LPS stabilized polymers by cryo-EM is a promising approach but requires further optimization.

5.5 The GBP activation mechanism as a regulatory safeguard

Taken together, coordinated movements in the LG domain enable dimerization via the G interface and at the same time make the oligomeric interface accessible. Hence, GBP1 displays a self-activation mechanism. In a cellular environment, such a mechanism must be tightly regulated to protect uninfected cells. Fisch et al. (2023) show that phosphorylation of GBP1 and binding of the regulatory 14-3-3σ protein to phosphorylated GBP1 control its activity and limit self-damage. Using cryo-EM, the authors demonstrate that 14-3-3σ interacts with GBP1, presumably via the GED and helix α4'. Even though the achieved resolution did not allow for detailed structural analysis, the conformation of 14-3-3σ directly blocks the

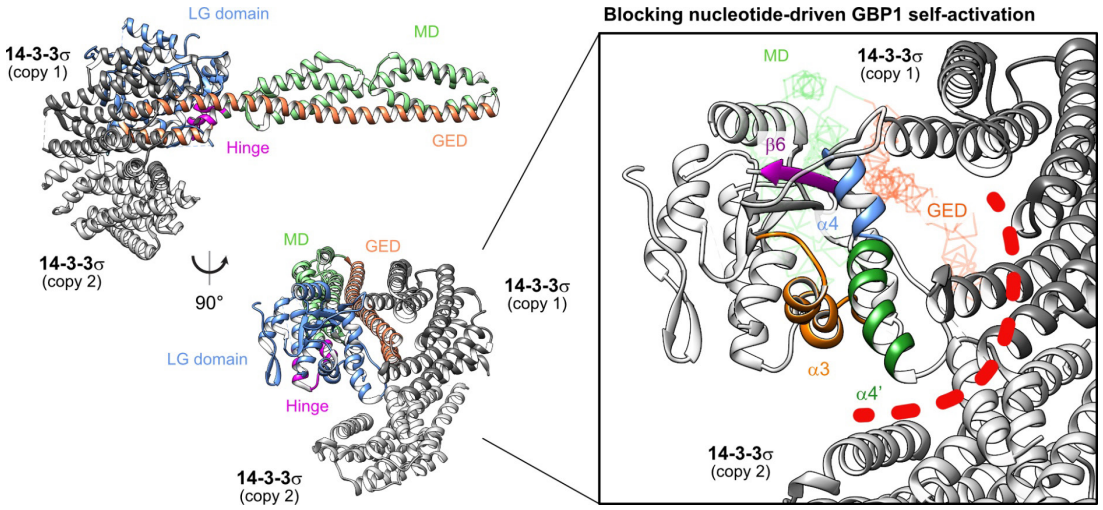

Figure 41. Regulatory 14-3-3σ protein blocks nucleotide-driven GBP1 self-activation. 14-3-3σ interacts with phosphorylated GBP1 (PDB 8q4l), presumably via GED and helix α4', and prevents coordinated movements in the LG domain (red dotted line). Note that the cryo-EM structure is a polyalanine rigid body docked model of nucleotide-free GBP1 (PDB 1f5n) and 14-3-3σ dimer (PDB 1ywt). LG: large GTPase, MD: middle domain, GED: GTPase effector domain.

opening of the GED and the establishment of both the G interface and the oligomer interface (Figure 41). In this way, GBP1 can be kept inactive by physically hindering the coordinated movements in the LG domain, thus preventing its nucleotide-driven activation. This observation further suggests that the nucleotide-driven activation mechanism of GBP1 is particularly required for releasing the GED. In contrast to the closely related atlastin protein family, the identified pivot point is highly conserved within the GBP family (Figure 42). The fact that atlastin is lacking a C-terminal GED further supports this hypothesis. GBP2, like GBP1, exists as a closed monomer in its nucleotide-free state (Cui et al., 2021). Protein structure predictions of GBP3 (AF-Q9H0R5-F1), GBP4 (AF-Q96PP9-F1), GBP6 (AF-Q6ZN66-F1), and GBP7 (AF-Q8N8V2-F1) also suggest a closed monomeric conformation with the GED attached to the LG domain (Varadi et al., 2022). GBP5 (AF-Q96PP8-F1), on the other hand, adopts an open monomeric conformation with the GED already being detached, as also shown by Kutsch et al. (2018).

It can be hypothesized that the nucleotide-driven activation mechanism of GBP1, and likely of all other members beside GBP5, might serve as a regulatory safeguard in activating GBP-mediated antimicrobial immune responses. But why does this not apply to GBP5? In contrast to GBP1-4, GBP5 does not contribute to the GBP platform on gram-negative bacteria

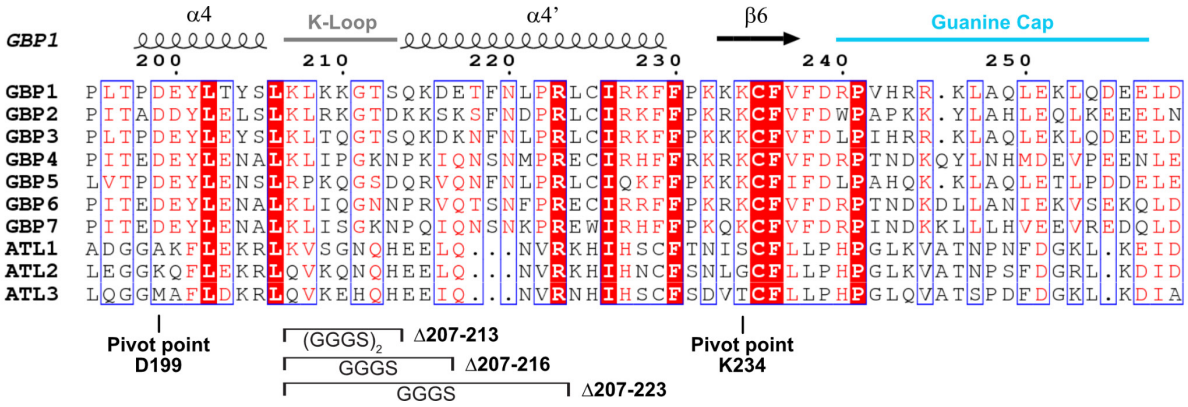

Figure 42. Sequence alignment of the intramolecular lever. Structural elements of PDB 1dg3 (GBP1) are shown. The pivot point residues and the generated helix α4' variants for GBP1 are marked. GBP: human guanylate-binding protein. ATL: human atlastin. UniProt accession numbers: P32455 (GBP1), P32456 (GBP2), Q9H0R5 (GBP3), Q96PP9 (GBP4), Q96PP8 (GBP5), Q6ZN66 (GBP6), Q8N8V2 (GBP7), Q8WXF7 (ATL1), Q8NHH9 (ATL2), Q6DD88 (ATL3).

but has been shown to be a positive regulator of the canonical NLRP3 inflammasome. In this way, GBP5 enhances caspase-1 activation in response to cytosolic LPS by linking caspase-4 activation with the activation of the NLRP3 inflammasome (see Figure 9) (Fisch et al., 2019a). It can be speculated that this unique role does not require strict structural safety measures or that a facilitated activation is beneficial in triggering immune responses upon bacterial infection.

5.6 Perspectives for future research on GBP-mediated immunity

Structural insights into GBP1's activation mechanism promote understanding of its macromolecular assemblies and their cellular function in infections. This thesis reveals the overall architecture of GBP1 building blocks in their active oligomeric states and identifies the peripheral helix α4' in the large GTPase domain to be critical for establishing the oligomeric interface. The results will make a significant contribution to the conceptualization of further studies aiming for high-resolution insights into the oligomeric interface. On this basis, more detailed questions can be addressed: is there a direct interaction between two α4' of adjacent GBP1 dimers, or does the oligomeric interface involve additional parts of the LG domain? Is this interface specific for GBP1 oligomers or can GBP1 interact with other members of the GBP family in a similar fashion? Can hetero-oligomerization via the α4' interface be a

mechanism to recruit GBP1 paralogs to the surface of bacteria as shown by Santos et al. (2020); Wandel et al. (2020); Zhu et al. (2024)? To clarify the latter aspect, the role of individual members of the membrane-bound GBP platform could be studied by using specific interface mutants, ideally in combination with structural studies on the hetero-dimeric assemblies.

Results of this work further demonstrate that nucleotide-dependent structural changes coordinate GBP1 oligomerization toward the formation of an antimicrobial protein coat. It can be speculated whether the proposed LPS-stabilized activation mechanism also plays a role for the conversion of the soluble GBP1 polymers to the membrane-bound coatomer on bacteria. Moreover, it would be relevant to gain insights into the structural dynamics of the established GBP1 coatomer during the GTPase cycle. Thus, the native function as a possible macro-molecular machine could be studied, which would shed light on what happens to outstretched GBP1 dimers once they formed the coatomer. High-resolution structures of GBP1's oligomeric states stabilized by LPS, for example, will address how these cytosolic and membrane-bound complexes contribute to the activation of the innate immune response on a molecular and mechanistic level. Particularly, it will be of interest to study the supramolecular GBP1:LPS:caspase-4 complex required for caspase-4 activation. Which moieties of GBP1 and LPS interact with each other? How does this complex recruit caspase-4? Based on the described architecture of soluble GBP1 polymers, it can be speculated that the polymers provide a platform for caspase-4 activation by facilitating the formation of LPS micelles. In this way, cytosolic lipid A could be clustered and exposed for direct interaction with caspase-4 initiating inflammatory and antibacterial responses.

Together, combining structural and mechanistic knowledge of GBP1's assemblies with its cellular functions in initiating and accelerating the innate immune response will be key for future studies to delineate the mechanisms of how GBP1 as dynamic molecular machine orchestrates GBP-mediated immunity.

6 References

Acikalin, M.Y., Gorgolewski, K.J., and Poldrack, R.A. (2017). A Coordinate-Based Meta-Analysis of Overlaps in Regional Specialization and Functional Connectivity across Subjective Value and Default Mode Networks. Front Neurosci *11*, 1.

Akira, S., and Takeda, K. (2004). Toll-like receptor signalling. Nat Rev Immunol *4*, 499-511.

Akira, S., Uematsu, S., and Takeuchi, O. (2006). Pathogen recognition and innate immunity. Cell *124*, 783-801.

Anand, R., Eschenburg, S., and Reubold, T.F. (2016). Crystal structure of the GTPase domain and the bundle signalling element of dynamin in the GDP state. Biochem Biophys Res Commun *469*, 76-80.

Ash, M.R., Maher, M.J., Mitchell Guss, J., and Jormakka, M. (2012). The cation-dependent G-proteins: in a class of their own. FEBS Lett *586*, 2218-2224.

Backhed, F., Normark, S., Schweda, E.K., Oscarson, S., and Richter-Dahlfors, A. (2003). Structural requirements for TLR4-mediated LPS signalling: a biological role for LPS modifications. Microbes Infect *5*, 1057-1063.

Balyschew, N., Yushkevich, A., Mikirtumov, V., Sanchez, R.M., Sprink, T., and Kudryashev, M. (2023). Streamlined structure determination by cryo-electron tomography and subtomogram averaging using TomoBEAR. Nat Commun *14*, 6543.

Bass, A.R., Egan, M.S., Alexander-Floyd, J., Lopes Fischer, N., Doerner, J., and Shin, S. (2023). Human GBP1 facilitates the rupture of the Legionella-containing vacuole and inflammasome activation. mBio *14*, e0170723.

Batista, C.R.A., Gomes, G.F., Candelario-Jalil, E., Fiebich, B.L., and de Oliveira, A.C.P. (2019). Lipopolysaccharide-Induced Neuroinflammation as a Bridge to Understand Neurodegeneration. Int J Mol Sci *20*.

Bender, D., Koulouri, A., Wen, X., Glitscher, M., Schollmeier, A., Fernandes da Costa, L., Murra, R.O., Carra, G.P., Haberger, V., Praefcke, G.J.K.*, et al.* (2024). Guanylate-binding protein 1 acts as a pro-viral factor for the life cycle of hepatitis C virus. PLoS Pathog *20*, e1011976.

Bian, X., Klemm, R.W., Liu, T.Y., Zhang, M., Sun, S., Sui, X., Liu, X., Rapoport, T.A., and Hu, J. (2011). Structures of the atlastin GTPase provide insight into homotypic fusion of endoplasmic reticulum membranes. Proc Natl Acad Sci U S A *108*, 3976-3981.

Boehm, U., Klamp, T., Groot, M., and Howard, J.C. (1997). Cellular responses to interferon-gamma. Annu Rev Immunol *15*, 749-795.

Bohm, G., Muhr, R., and Jaenicke, R. (1992). Quantitative analysis of protein far UV circular dichroism spectra by neural networks. Protein Eng *5*, 191-195.

Borden, E.C., Sen, G.C., Uze, G., Silverman, R.H., Ransohoff, R.M., Foster, G.R., and Stark, G.R. (2007). Interferons at age 50: past, current and future impact on biomedicine. Nat Rev Drug Discov *6*, 975-990.

Britzen-Laurent, N., Bauer, M., Berton, V., Fischer, N., Syguda, A., Reipschlager, S., Naschberger, E., Herrmann, C., and Sturzl, M. (2010). Intracellular trafficking of guanylate-binding proteins is regulated by heterodimerization in a hierarchical manner. PLoS One *5*, e14246.

Brown, G.C. (2019). The endotoxin hypothesis of neurodegeneration. J Neuroinflammation *16*, 180.

Burnet, F.M. (1976). A modification of Jerne's theory of antibody production using the concept of clonal selection. CA Cancer J Clin *26*, 119-121.

Byrnes, L.J., Singh, A., Szeto, K., Benvin, N.M., O'Donnell, J.P., Zipfel, W.R., and Sondermann, H. (2013). Structural basis for conformational switching and GTP loading of the large G protein atlastin. EMBO J *32*, 369-384.

Byrnes, L.J., and Sondermann, H. (2011). Structural basis for the nucleotide-dependent dimerization of the large G protein atlastin-1/SPG3A. Proc Natl Acad Sci U S A *108*, 2216-2221.

Castano-Diez, D., Kudryashev, M., Arheit, M., and Stahlberg, H. (2012). Dynamo: a flexible, user-friendly development tool for subtomogram averaging of cryo-EM data in high-performance computing environments. J Struct Biol *178*, 139-151.

Chappie, J.S., Mears, J.A., Fang, S., Leonard, M., Schmid, S.L., Milligan, R.A., Hinshaw, J.E., and Dyda, F. (2011). A pseudoatomic model of the dynamin polymer identifies a hydrolysis-dependent powerstroke. Cell *147*, 209-222.

Cheng, Y.S., Colonno, R.J., and Yin, F.H. (1983). Interferon induction of fibroblast proteins with guanylate binding activity. J Biol Chem *258*, 7746-7750.

Chung, C.T., Niemela, S.L., and Miller, R.H. (1989). One-step preparation of competent Escherichia coli: transformation and storage of bacterial cells in the same solution. Proc Natl Acad Sci U S A *86*, 2172-2175.

Coers, J. (2013). Self and non-self discrimination of intracellular membranes by the innate immune system. PLoS Pathog *9*, e1003538.

Cohen, S., Bigazzi, P.E., and Yoshida, T. (1974). Commentary. Similarities of T cell function in cell-mediated immunity and antibody production. Cell Immunol *12*, 150-159.

Condie, R.M., Zak, S.J., and Good, R.A. (1955). Effect of meningococcal endotoxin on the immune response. Proc Soc Exp Biol Med *90*, 355-360.

Cui, W., Braun, E., Wang, W., Tang, J., Zheng, Y., Slater, B., Li, N., Chen, C., Liu, Q., Wang, B.*, et al.* (2021). Structural basis for GTP-induced dimerization and antiviral function of guanylate-binding proteins. Proc Natl Acad Sci U S A *118*.

Daumke, O., and Praefcke, G.J. (2016). Invited review: Mechanisms of GTP hydrolysis and conformational transitions in the dynamin superfamily. Biopolymers *105*, 580-593.

Davis, B.K., Wen, H., and Ting, J.P. (2011). The inflammasome NLRs in immunity, inflammation, and associated diseases. Annu Rev Immunol *29*, 707-735.

Devant, P., and Kagan, J.C. (2023). Molecular mechanisms of gasdermin D pore-forming activity. Nat Immunol *24*, 1064-1075.

Dickinson, M.S., Kutsch, M., Sistemich, L., Hernandez, D., Piro, A.S., Needham, D., Lesser, C.F., Herrmann, C., and Coers, J. (2023). LPS-aggregating proteins GBP1 and GBP2 are each sufficient to enhance caspase-4 activation both in cellulo and in vitro. Proc Natl Acad Sci U S A *120*, e2216028120.

Downs, K.P., Nguyen, H., Dorfleutner, A., and Stehlik, C. (2020). An overview of the non-canonical inflammasome. Mol Aspects Med *76*, 100924.

Erridge, C., Bennett-Guerrero, E., and Poxton, I.R. (2002). Structure and function of lipopolysaccharides. Microbes Infect *4*, 837-851.

Faelber, K., Dietrich, L., Noel, J.K., Wollweber, F., Pfitzner, A.K., Muhleip, A., Sanchez, R., Kudryashev, M., Chiaruttini, N., Lilie, H.*, et al.* (2019). Structure and assembly of the mitochondrial membrane remodelling GTPase Mgm1. Nature *571*, 429-433.

Faelber, K., Posor, Y., Gao, S., Held, M., Roske, Y., Schulze, D., Haucke, V., Noe, F., and Daumke, O. (2011). Crystal structure of nucleotide-free dynamin. Nature *477*, 556-560.

Feeley, E.M., Pilla-Moffett, D.M., Zwack, E.E., Piro, A.S., Finethy, R., Kolb, J.P., Martinez, J., Brodsky, I.E., and Coers, J. (2017). Galectin-3 directs antimicrobial guanylate binding proteins to vacuoles furnished with bacterial secretion systems. Proc Natl Acad Sci U S A *114*, E1698-E1706.

Feng, J., Cao, Z., Wang, L., Wan, Y., Peng, N., Wang, Q., Chen, X., Zhou, Y., and Zhu, Y. (2017). Inducible GBP5 Mediates the Antiviral Response via Interferon-Related Pathways during Influenza A Virus Infection. J Innate Immun *9*, 419-435.

Fisch, D., Bando, H., Clough, B., Hornung, V., Yamamoto, M., Shenoy, A.R., and Frickel, E.M. (2019a). Human GBP1 is a microbe-specific gatekeeper of macrophage apoptosis and pyroptosis. EMBO J *38*, e100926.

Fisch, D., Clough, B., Domart, M.C., Encheva, V., Bando, H., Snijders, A.P., Collinson, L.M., Yamamoto, M., Shenoy, A.R., and Frickel, E.M. (2020). Human GBP1 Differentially Targets Salmonella and Toxoplasma to License Recognition of Microbial Ligands and Caspase-Mediated Death. Cell Rep *32*, 108008.

Fisch, D., Evans, R., Clough, B., Byrne, S.K., Channell, W.M., Dockterman, J., and Frickel, E.M. (2021). HRMAn 2.0: Next-generation artificial intelligence-driven analysis for broad host-pathogen interactions. Cell Microbiol *23*, e13349.

Fisch, D., Pfleiderer, M.M., Anastasakou, E., Mackie, G.M., Wendt, F., Liu, X., Clough, B., Lara-Reyna, S., Encheva, V., Snijders, A.P.*, et al.* (2023). PIM1 controls GBP1 activity to limit self-damage and to guard against pathogen infection. Science *382*, eadg2253.

Fisch, D., Yakimovich, A., Clough, B., Wright, J., Bunyan, M., Howell, M., Mercer, J., and Frickel, E. (2019b). Defining host-pathogen interactions employing an artificial intelligence workflow. Elife *8*.

Folch, J., Lees, M., and Sloane Stanley, G.H. (1957). A simple method for the isolation and purification of total lipides from animal tissues. J Biol Chem *226*, 497-509.

Fres, J.M., Muller, S., and Praefcke, G.J. (2010). Purification of the CaaX-modified, dynamin-related large GTPase hGBP1 by coexpression with farnesyltransferase. J Lipid Res *51*, 2454-2459.

Ganichkin, O.M., Vancraenenbroeck, R., Rosenblum, G., Hofmann, H., Mikhailov, A.S., Daumke, O., and Noel, J.K. (2021). Quantification and demonstration of the collective constriction-by-ratchet mechanism in the dynamin molecular motor. Proc Natl Acad Sci U S A *118*.

Ghosh, A., Praefcke, G.J., Renault, L., Wittinghofer, A., and Herrmann, C. (2006). How guanylate-binding proteins achieve assembly-stimulated processive cleavage of GTP to GMP. Nature *440*, 101-104.

Goers, L., Kim, K., Stedman, T.C., Canning, P.J., Mou, X., Ernst, N.H., Coers, J., and Lesser, C.F. (2023). Shigella IpaH9.8 limits GBP1-dependent LPS release from intracytosolic bacteria to suppress caspase-4 activation. Proc Natl Acad Sci U S A *120*, e2218469120.

Green, M.R., and Sambrook, J. (2012). Molecular Cloning: A Laboratory Manual, 4th edn (Cold Spring Harbor, N.Y.: Cold Spring Harbor Laboratory Press).

Gutsmann, T., Schromm, A.B., and Brandenburg, K. (2007). The physicochemistry of endotoxins in relation to bioactivity. Int J Med Microbiol *297*, 341-352.

Hales, K.G., and Fuller, M.T. (1997). Developmentally regulated mitochondrial fusion mediated by a conserved, novel, predicted GTPase. Cell *90*, 121-129.

Hanahan, D.J., Turner, M.B., and Jayko, M.E. (1951). The isolation of egg phosphatidyl choline by an adsorption column technique. J Biol Chem *192*, 623-628.

Hayashi, F., Smith, K.D., Ozinsky, A., Hawn, T.R., Yi, E.C., Goodlett, D.R., Eng, J.K., Akira, S., Underhill, D.M., and Aderem, A. (2001). The innate immune response to bacterial flagellin is mediated by Toll-like receptor 5. Nature *410*, 1099-1103.

Hemmi, H., Takeuchi, O., Kawai, T., Kaisho, T., Sato, S., Sanjo, H., Matsumoto, M., Hoshino, K., Wagner, H., Takeda, K.*, et al.* (2000). A Toll-like receptor recognizes bacterial DNA. Nature *408*, 740-745.

Hinshaw, J.E., and Schmid, S.L. (1995). Dynamin self-assembles into rings suggesting a mechanism for coated vesicle budding. Nature *374*, 190-192.

Hu, J., Shibata, Y., Zhu, P.P., Voss, C., Rismanchi, N., Prinz, W.A., Rapoport, T.A., and Blackstone, C. (2009). A class of dynamin-like GTPases involved in the generation of the tubular ER network. Cell *138*, 549-561.

Ince, S., Kutsch, M., Shydlovskyi, S., and Herrmann, C. (2017). The human guanylate-binding proteins hGBP-1 and hGBP-5 cycle between monomers and dimers only. FEBS J *284*, 2284-2301.

Ince, S., Zhang, P., Kutsch, M., Krenczyk, O., Shydlovskyi, S., and Herrmann, C. (2021). Catalytic activity of human guanylate-binding protein 1 coupled to the release of structural restraints imposed by the C-terminal domain. FEBS J *288*, 582-599.

Isaacs, A., and Lindenmann, J. (1957). Virus interference. I. The interferon. Proc R Soc Lond B Biol Sci *147*, 258-267.

Itsui, Y., Sakamoto, N., Kakinuma, S., Nakagawa, M., Sekine-Osajima, Y., Tasaka-Fujita, M., Nishimura-Sakurai, Y., Suda, G., Karakama, Y., Mishima, K.*, et al.* (2009). Antiviral effects of the interferon-induced protein guanylate binding protein 1 and its interaction with the hepatitis C virus NS5B protein. Hepatology *50*, 1727-1737.

Janeway, C.A., Jr. (1989). Approaching the asymptote? Evolution and revolution in immunology. Cold Spring Harb Symp Quant Biol *54 Pt 1*, 1-13.

Ji, C., Du, S., Li, P., Zhu, Q., Yang, X., Long, C., Yu, J., Shao, F., and Xiao, J. (2019). Structural mechanism for guanylate-binding proteins (GBPs) targeting by the Shigella E3 ligase IpaH9.8. PLoS Pathog *15*, e1007876.

Jimenez Fernandez, D., and Lamkanfi, M. (2015). Inflammatory caspases: key regulators of inflammation and cell death. Biol Chem *396*, 193-203.

Jumper, J., Evans, R., Pritzel, A., Green, T., Figurnov, M., Ronneberger, O., Tunyasuvunakool, K., Bates, R., Zidek, A., Potapenko, A.*, et al.* (2021). Highly accurate protein structure prediction with AlphaFold. Nature *596*, 583-589.

Jurkovich, G.J., Mileski, W.J., Maier, R.V., Winn, R.K., and Rice, C.L. (1991). Interferon gamma increases sensitivity to endotoxin. J Surg Res *51*, 197-203.

Kalynych, S., Morona, R., and Cygler, M. (2014). Progress in understanding the assembly process of bacterial O-antigen. FEMS Microbiol Rev *38*, 1048-1065.

Kang, B.H., Busse, J.S., and Bednarek, S.Y. (2003). Members of the Arabidopsis dynamin-like gene family, ADL1, are essential for plant cytokinesis and polarized cell growth. Plant Cell *15*, 899-913.

Kanneganti, T.D., Lamkanfi, M., and Nunez, G. (2007). Intracellular NOD-like receptors in host defense and disease. Immunity *27*, 549-559.

Kayagaki, N., Stowe, I.B., Lee, B.L., O'Rourke, K., Anderson, K., Warming, S., Cuellar, T., Haley, B., Roose-Girma, M., Phung, Q.T.*, et al.* (2015). Caspase-11 cleaves gasdermin D for non-canonical inflammasome signalling. Nature *526*, 666-671.

Kell, D.B., and Pretorius, E. (2015). On the translocation of bacteria and their lipopolysaccharides between blood and peripheral locations in chronic, inflammatory diseases: the central roles of LPS and LPS-induced cell death. Integr Biol (Camb) *7*, 1339-1377.

Khare, S., Dorfleutner, A., Bryan, N.B., Yun, C., Radian, A.D., de Almeida, L., Rojanasakul, Y., and Stehlik, C. (2012). An NLRP7-containing inflammasome mediates recognition of microbial lipopeptides in human macrophages. Immunity *36*, 464-476.

Kim, B.H., Shenoy, A.R., Kumar, P., Bradfield, C.J., and MacMicking, J.D. (2012). IFN-inducible GTPases in host cell defense. Cell Host Microbe *12*, 432-444.

Kimanius, D., Dong, L., Sharov, G., Nakane, T., and Scheres, S.H.W. (2021). New tools for automated cryo-EM single-particle analysis in RELION-4.0. Biochem J *478*, 4169-4185.

Kloog, Y., and Cox, A.D. (2004). Prenyl-binding domains: potential targets for Ras inhibitors and anti-cancer drugs. Semin Cancer Biol *14*, 253-261.

Kong, L., Sochacki, K.A., Wang, H., Fang, S., Canagarajah, B., Kehr, A.D., Rice, W.J., Strub, M.P., Taraska, J.W., and Hinshaw, J.E. (2018). Cryo-EM of the dynamin polymer assembled on lipid membrane. Nature *560*, 258-262.

Kozak, W., Conn, C.A., and Kluger, M.J. (1994). Lipopolysaccharide induces fever and depresses locomotor activity in unrestrained mice. Am J Physiol *266*, R125-135.

Krapp, C., Hotter, D., Gawanbacht, A., McLaren, P.J., Kluge, S.F., Sturzel, C.M., Mack, K., Reith, E., Engelhart, S., Ciuffi, A.*, et al.* (2016). Guanylate Binding Protein (GBP) 5 Is an Interferon-Inducible Inhibitor of HIV-1 Infectivity. Cell Host Microbe *19*, 504-514.

Kremer, J.R., Mastronarde, D.N., and McIntosh, J.R. (1996). Computer visualization of three-dimensional image data using IMOD. J Struct Biol *116*, 71-76.

Kuhm, T., Pinto, C.d.A., Gross, L., Huber, S.T., Taisne, C., Giannopoulou, E.A., Pardon, E., Steyaert, J., Tans, S.J., and Jakobi, A.J. (2023). Structural basis of membrane targeting and coatomer assembly by human GBP1. bioRxiv, 2023.2003.2028.534355.

Kulp, A., and Kuehn, M.J. (2010). Biological functions and biogenesis of secreted bacterial outer membrane vesicles. Annu Rev Microbiol *64*, 163-184.

Kunzelmann, S., Praefcke, G.J., and Herrmann, C. (2005). Nucleotide binding and self-stimulated GTPase activity of human guanylate-binding protein 1 (hGBP1). Methods Enzymol *404*, 512-527.

Kutsch, M., and Coers, J. (2021). Human guanylate binding proteins: nanomachines orchestrating host defense. FEBS J *288*, 5826-5849.

Kutsch, M., Ince, S., and Herrmann, C. (2018). Homo and hetero dimerisation of the human guanylate-binding proteins hGBP-1 and hGBP-5 characterised by affinities and kinetics. FEBS J *285*, 2019-2036.

Kutsch, M., Sistemich, L., Lesser, C.F., Goldberg, M.B., Herrmann, C., and Coers, J. (2020). Direct binding of polymeric GBP1 to LPS disrupts bacterial cell envelope functions. EMBO J *39*, e104926.

Labrousse, A.M., Zappaterra, M.D., Rube, D.A., and van der Bliek, A.M. (1999). C. elegans dynamin-related protein DRP-1 controls severing of the mitochondrial outer membrane. Mol Cell *4*, 815-826.

Laemmli, U.K. (1970). Cleavage of structural proteins during the assembly of the head of bacteriophage T4. Nature *227*, 680-685.

Lemaitre, B., Nicolas, E., Michaut, L., Reichhart, J.M., and Hoffmann, J.A. (1996). The dorsoventral regulatory gene cassette spatzle/Toll/cactus controls the potent antifungal response in Drosophila adults. Cell *86*, 973-983.

MacMicking, J.D. (2004). IFN-inducible GTPases and immunity to intracellular pathogens. Trends Immunol *25*, 601-609.

MacMicking, J.D. (2012). Interferon-inducible effector mechanisms in cell-autonomous immunity. Nat Rev Immunol *12*, 367-382.

Man, S.M. (2018). Inflammasomes in the gastrointestinal tract: infection, cancer and gut microbiota homeostasis. Nat Rev Gastroenterol Hepatol *15*, 721-737.

Man, S.M., Karki, R., Malireddi, R.K., Neale, G., Vogel, P., Yamamoto, M., Lamkanfi, M., and Kanneganti, T.D. (2015). The transcription factor IRF1 and guanylate-binding proteins target activation of the AIM2 inflammasome by Francisella infection. Nat Immunol *16*, 467-475.

Martinon, F., Burns, K., and Tschopp, J. (2002). The inflammasome: a molecular platform triggering activation of inflammatory caspases and processing of proIL-beta. Mol Cell *10*, 417-426.

Mastronarde, D.N. (2005). Automated electron microscope tomography using robust prediction of specimen movements. J Struct Biol *152*, 36-51.

Mears, J.A., Ray, P., and Hinshaw, J.E. (2007). A corkscrew model for dynamin constriction. Structure *15*, 1190-1202.

Meng, E.C., Goddard, T.D., Pettersen, E.F., Couch, G.S., Pearson, Z.J., Morris, J.H., and Ferrin, T.E. (2023). UCSF ChimeraX: Tools for structure building and analysis. Protein Sci *32*, e4792.

Menkin, V. (1944). Chemical Basis of Fever. Science *100*, 337-338.

Meunier, E., and Broz, P. (2016). Interferon-inducible GTPases in cell autonomous and innate immunity. Cell Microbiol *18*, 168-180.

Meunier, E., Wallet, P., Dreier, R.F., Costanzo, S., Anton, L., Ruhl, S., Dussurgey, S., Dick, M.S., Kistner, A., Rigard, M.*, et al.* (2015). Guanylate-binding proteins promote activation of the AIM2 inflammasome during infection with Francisella novicida. Nat Immunol *16*, 476-484.

Mirdita, M., Schutze, K., Moriwaki, Y., Heo, L., Ovchinnikov, S., and Steinegger, M. (2022). ColabFold: making protein folding accessible to all. Nat Methods *19*, 679-682.

Moffatt, J.H., Harper, M., and Boyce, J.D. (2019). Mechanisms of Polymyxin Resistance. Adv Exp Med Biol *1145*, 55-71.

Mogensen, T.H. (2009). Pathogen recognition and inflammatory signaling in innate immune defenses. Clin Microbiol Rev *22*, 240-273, Table of Contents.

Morlot, S., Lenz, M., Prost, J., Joanny, J.F., and Roux, A. (2010). Deformation of dynamin helices damped by membrane friction. Biophys J *99*, 3580-3588.

Niemann, H.H., Knetsch, M.L., Scherer, A., Manstein, D.J., and Kull, F.J. (2001). Crystal structure of a dynamin GTPase domain in both nucleotide-free and GDP-bound forms. EMBO J *20*, 5813-5821.

Novelli, G., and D'Apice, M.R. (2012). Protein farnesylation and disease. J Inherit Metab Dis *35*, 917-926.

Oeckinghaus, A., and Ghosh, S. (2009). The NF-kappaB family of transcription factors and its regulation. Cold Spring Harb Perspect Biol *1*, a000034.

Olichon, A., Emorine, L.J., Descoins, E., Pelloquin, L., Brichese, L., Gas, N., Guillou, E., Delettre, C., Valette, A., Hamel, C.P.*, et al.* (2002). The human dynamin-related protein OPA1 is anchored to the mitochondrial inner membrane facing the inter-membrane space. FEBS Lett *523*, 171-176.

Olszewski, M.A., Gray, J., and Vestal, D.J. (2006). In silico genomic analysis of the human and murine guanylate-binding protein (GBP) gene clusters. J Interferon Cytokine Res *26*, 328-352.

Orso, G., Pendin, D., Liu, S., Tosetto, J., Moss, T.J., Faust, J.E., Micaroni, M., Egorova, A., Martinuzzi, A., McNew, J.A.*, et al.* (2009). Homotypic fusion of ER membranes requires the dynamin-like GTPase atlastin. Nature *460*, 978-983.

Page, M.J., Kell, D.B., and Pretorius, E. (2022). The Role of Lipopolysaccharide-Induced Cell Signalling in Chronic Inflammation. Chronic Stress (Thousand Oaks) *6*, 24705470221076390.

Papo, N., and Shai, Y. (2005). A molecular mechanism for lipopolysaccharide protection of Gram-negative bacteria from antimicrobial peptides. J Biol Chem *280*, 10378-10387.

Park, B.S., Song, D.H., Kim, H.M., Choi, B.S., Lee, H., and Lee, J.O. (2009). The structural basis of lipopolysaccharide recognition by the TLR4-MD-2 complex. Nature *458*, 1191-1195.

Park, H.S., Jung, H.Y., Park, E.Y., Kim, J., Lee, W.J., and Bae, Y.S. (2004). Cutting edge: direct interaction of TLR4 with NAD(P)H oxidase 4 isozyme is essential for lipopolysaccharide-induced production of reactive oxygen species and activation of NF-kappa B. J Immunol *173*, 3589-3593.

Pettersen, E.F., Goddard, T.D., Huang, C.C., Couch, G.S., Greenblatt, D.M., Meng, E.C., and Ferrin, T.E. (2004). UCSF Chimera--a visualization system for exploratory research and analysis. J Comput Chem *25*, 1605-1612.

Peulen, T.O., Hengstenberg, C.S., Biehl, R., Dimura, M., Lorenz, C., Valeri, A., Folz, J., Hanke, C.A., Ince, S., Vopel, T.*, et al.* (2023). Integrative dynamic structural biology unveils conformers essential for the oligomerization of a large GTPase. Elife *12*.

Pilla-Moffett, D., Barber, M.F., Taylor, G.A., and Coers, J. (2016). Interferon-Inducible GTPases in Host Resistance, Inflammation and Disease. J Mol Biol *428*, 3495-3513.

Piro, A.S., Hernandez, D., Luoma, S., Feeley, E.M., Finethy, R., Yirga, A., Frickel, E.M., Lesser, C.F., and Coers, J. (2017). Detection of Cytosolic Shigella flexneri via a C-Terminal Triple-Arginine Motif of GBP1 Inhibits Actin-Based Motility. mBio *8*.

Poltorak, A., He, X., Smirnova, I., Liu, M.Y., Van Huffel, C., Du, X., Birdwell, D., Alejos, E., Silva, M., Galanos, C.*, et al.* (1998). Defective LPS signaling in C3H/HeJ and C57BL/10ScCr mice: mutations in Tlr4 gene. Science *282*, 2085-2088.

Praefcke, G.J., Geyer, M., Schwemmle, M., Robert Kalbitzer, H., and Herrmann, C. (1999). Nucleotide-binding characteristics of human guanylate-binding protein 1 (hGBP1) and identification of the third GTP-binding motif. J Mol Biol *292*, 321-332.

Praefcke, G.J., Kloep, S., Benscheid, U., Lilie, H., Prakash, B., and Herrmann, C. (2004). Identification of residues in the human guanylate-binding protein 1 critical for nucleotide binding and cooperative GTP hydrolysis. J Mol Biol *344*, 257-269.

Praefcke, G.J., and McMahon, H.T. (2004). The dynamin superfamily: universal membrane tubulation and fission molecules? Nat Rev Mol Cell Biol *5*, 133-147.

Praefcke, G.J.K. (2018). Regulation of innate immune functions by guanylate-binding proteins. Int J Med Microbiol *308*, 237-245.

Prakash, B., Praefcke, G.J., Renault, L., Wittinghofer, A., and Herrmann, C. (2000a). Structure of human guanylate-binding protein 1 representing a unique class of GTP-binding proteins. Nature *403*, 567-571.

Prakash, B., Renault, L., Praefcke, G.J., Herrmann, C., and Wittinghofer, A. (2000b). Triphosphate structure of guanylate-binding protein 1 and implications for nucleotide binding and GTPase mechanism. EMBO J *19*, 4555-4564.

Raetz, C.R., and Whitfield, C. (2002). Lipopolysaccharide endotoxins. Annu Rev Biochem *71*, 635-700.

Rafeld, H.L., Kolanus, W., van Driel, I.R., and Hartland, E.L. (2021). Interferon-induced GTPases orchestrate host cell-autonomous defence against bacterial pathogens. Biochem Soc Trans *49*, 1287-1297.

Ramachandran, R., and Schmid, S.L. (2018). The dynamin superfamily. Curr Biol *28*, R411-R416.

Rathinam, V.A., and Fitzgerald, K.A. (2016). Inflammasome Complexes: Emerging Mechanisms and Effector Functions. Cell *165*, 792-800.

Reubold, T.F., Faelber, K., Plattner, N., Posor, Y., Ketel, K., Curth, U., Schlegel, J., Anand, R., Manstein, D.J., Noe, F.*, et al.* (2015). Crystal structure of the dynamin tetramer. Nature *525*, 404-408.

Rivera-Cuevas, Y., Clough, B., and Frickel, E.M. (2023). Human guanylate-binding proteins in intracellular pathogen detection, destruction, and host cell death induction. Curr Opin Immunol *84*, 102373.

Robert, X., and Gouet, P. (2014). Deciphering key features in protein structures with the new ENDscript server. Nucleic Acids Res *42*, W320-324.

Rohou, A., and Grigorieff, N. (2015). CTFFIND4: Fast and accurate defocus estimation from electron micrographs. J Struct Biol *192*, 216-221.

Roux, A., Uyhazi, K., Frost, A., and De Camilli, P. (2006). GTP-dependent twisting of dynamin implicates constriction and tension in membrane fission. Nature *441*, 528-531.

Sanchez, R.M., Zhang, Y., Chen, W., Dietrich, L., and Kudryashev, M. (2020). Subnanometer-resolution structure determination in situ by hybrid subtomogram averaging - single particle cryo-EM. Nat Commun *11*, 3709.

Santos, J.C., Boucher, D., Schneider, L.K., Demarco, B., Dilucca, M., Shkarina, K., Heilig, R., Chen, K.W., Lim, R.Y.H., and Broz, P. (2020). Human GBP1 binds LPS to initiate assembly of a caspase-4 activating platform on cytosolic bacteria. Nat Commun *11*, 3276.

Santos, J.C., and Broz, P. (2018). Sensing of invading pathogens by GBPs: At the crossroads between cell-autonomous and innate immunity. J Leukoc Biol *104*, 729-735.

Saraste, M., Sibbald, P.R., and Wittinghofer, A. (1990). The P-loop--a common motif in ATP- and GTP-binding proteins. Trends Biochem Sci *15*, 430-434.

Scheres, S.H., and Chen, S. (2012). Prevention of overfitting in cryo-EM structure determination. Nat Methods *9*, 853-854.

Schneider, C.A., Rasband, W.S., and Eliceiri, K.W. (2012). NIH Image to ImageJ: 25 years of image analysis. Nat Methods *9*, 671-675.

Schroder, K., Hertzog, P.J., Ravasi, T., and Hume, D.A. (2004). Interferon-gamma: an overview of signals, mechanisms and functions. J Leukoc Biol *75*, 163-189.

Schwemmle, M., and Staeheli, P. (1994). The interferon-induced 67-kDa guanylate-binding protein (hGBP1) is a GTPase that converts GTP to GMP. J Biol Chem *269*, 11299-11305.

Shi, J., Zhao, Y., Wang, Y., Gao, W., Ding, J., Li, P., Hu, L., and Shao, F. (2014). Inflammatory caspases are innate immune receptors for intracellular LPS. Nature *514*, 187-192.

Shydlovskyi, S., Zienert, A.Y., Ince, S., Dovengerds, C., Hohendahl, A., Dargazanli, J.M., Blum, A., Gunther, S.D., Kladt, N., Sturzl, M.*, et al.* (2017). Nucleotide-dependent farnesyl switch orchestrates polymerization and membrane binding of human guanylate-binding protein 1. Proc Natl Acad Sci U S A *114*, E5559-E5568.

Sievers, F., Wilm, A., Dineen, D., Gibson, T.J., Karplus, K., Li, W., Lopez, R., McWilliam, H., Remmert, M., Soding, J.*, et al.* (2011). Fast, scalable generation of high-quality protein multiple sequence alignments using Clustal Omega. Mol Syst Biol *7*, 539.

Sistemich, L., Dimitrov Stanchev, L., Kutsch, M., Roux, A., Gunther Pomorski, T., and Herrmann, C. (2021). Structural requirements for membrane binding of human guanylate-binding protein 1. FEBS J *288*, 4098-4114.

Sistemich, L., and Herrmann, C. (2020). Purification of Farnesylated hGBP1 and Characterization of Its Polymerization and Membrane Binding. Methods Mol Biol *2159*, 67-81.

Sistemich, L., Kutsch, M., Hamisch, B., Zhang, P., Shydlovskyi, S., Britzen-Laurent, N., Sturzl, M., Huber, K., and Herrmann, C. (2020). The Molecular Mechanism of Polymer Formation of Farnesylated Human Guanylate-binding Protein 1. J Mol Biol *432*, 2164-2185.

Staeheli, P., Haller, O., Boll, W., Lindenmann, J., and Weissmann, C. (1986). Mx protein: constitutive expression in 3T3 cells transformed with cloned Mx cDNA confers selective resistance to influenza virus. Cell *44*, 147-158.

Steinman, R.M., and Witmer, M.D. (1978). Lymphoid dendritic cells are potent stimulators of the primary mixed leukocyte reaction in mice. Proc Natl Acad Sci U S A *75*, 5132-5136.

Stoeber, M., Stoeck, I.K., Hanni, C., Bleck, C.K., Balistreri, G., and Helenius, A. (2012). Oligomers of the ATPase EHD2 confine caveolae to the plasma membrane through association with actin. EMBO J *31*, 2350-2364.

Takei, K., McPherson, P.S., Schmid, S.L., and De Camilli, P. (1995). Tubular membrane invaginations coated by dynamin rings are induced by GTP-gamma S in nerve terminals. Nature *374*, 186-190.

Tau, G., and Rothman, P. (1999). Biologic functions of the IFN-gamma receptors. Allergy *54*, 1233-1251.

Thornberry, N.A., Bull, H.G., Calaycay, J.R., Chapman, K.T., Howard, A.D., Kostura, M.J., Miller, D.K., Molineaux, S.M., Weidner, J.R., Aunins, J.*, et al.* (1992). A novel heterodimeric cysteine protease is required for interleukin-1 beta processing in monocytes. Nature *356*, 768-774.

Trent, M.S., Stead, C.M., Tran, A.X., and Hankins, J.V. (2006). Diversity of endotoxin and its impact on pathogenesis. J Endotoxin Res *12*, 205-223.

van der Poll, T., van de Veerdonk, F.L., Scicluna, B.P., and Netea, M.G. (2017). The immunopathology of sepsis and potential therapeutic targets. Nat Rev Immunol *17*, 407-420.

Varadi, M., Anyango, S., Deshpande, M., Nair, S., Natassia, C., Yordanova, G., Yuan, D., Stroe, O., Wood, G., Laydon, A.*, et al.* (2022). AlphaFold Protein Structure Database: massively expanding the structural coverage of protein-sequence space with high-accuracy models. Nucleic Acids Res *50*, D439-D444.

Vopel, T., Syguda, A., Britzen-Laurent, N., Kunzelmann, S., Ludemann, M.B., Dovengerds, C., Sturzl, M., and Herrmann, C. (2010). Mechanism of GTPase-activity-induced self-assembly of human guanylate binding protein 1. J Mol Biol *400*, 63-70.

Wandel, M.P., Kim, B.H., Park, E.S., Boyle, K.B., Nayak, K., Lagrange, B., Herod, A., Henry, T., Zilbauer, M., Rohde, J.*, et al.* (2020). Guanylate-binding proteins convert cytosolic bacteria into caspase-4 signaling platforms. Nat Immunol *21*, 880-891.

Wandel, M.P., Pathe, C., Werner, E.I., Ellison, C.J., Boyle, K.B., von der Malsburg, A., Rohde, J., and Randow, F. (2017). GBPs Inhibit Motility of Shigella flexneri but Are Targeted for Degradation by the Bacterial Ubiquitin Ligase IpaH9.8. Cell Host Microbe *22*, 507-518 e505.

Waterhouse, A., Bertoni, M., Bienert, S., Studer, G., Tauriello, G., Gumienny, R., Heer, F.T., de Beer, T.A.P., Rempfer, C., Bordoli, L.*, et al.* (2018). SWISS-MODEL: homology modelling of protein structures and complexes. Nucleic Acids Res *46*, W296-W303.

Weber, A., Wasiliew, P., and Kracht, M. (2010). Interleukin-1 (IL-1) pathway. Sci Signal *3*, cm1.

Wehner, M., Kunzelmann, S., and Herrmann, C. (2012). The guanine cap of human guanylate-binding protein 1 is responsible for dimerization and self-activation of GTP hydrolysis. FEBS J *279*, 203-210.

Weismehl, M., Chu, X., Kutsch, M., Lauterjung, P., Herrmann, C., Kudryashev, M., and Daumke, O. (2024). Structural insights into the activation mechanism of antimicrobial GBP1. The EMBO Journal *43*, 615-636.

Wilkins, M.R., Gasteiger, E., Bairoch, A., Sanchez, J.C., Williams, K.L., Appel, R.D., and Hochstrasser, D.F. (1999). Protein identification and analysis tools in the ExPASy server. Methods Mol Biol *112*, 531-552.

Xavier, A., Al-Zeer, M.A., Meyer, T.F., and Daumke, O. (2020). hGBP1 Coordinates Chlamydia Restriction and Inflammasome Activation through Sequential GTP Hydrolysis. Cell Rep *31*, 107667.

Xu, Y., Jagannath, C., Liu, X.D., Sharafkhaneh, A., Kolodziejska, K.E., and Eissa, N.T. (2007). Toll-like receptor 4 is a sensor for autophagy associated with innate immunity. Immunity *27*, 135-144.

Yoneyama, M., Kikuchi, M., Natsukawa, T., Shinobu, N., Imaizumi, T., Miyagishi, M., Taira, K., Akira, S., and Fujita, T. (2004). The RNA helicase RIG-I has an essential function in double-stranded RNA-induced innate antiviral responses. Nat Immunol *5*, 730-737.

Zhang, K. (2016). Gctf: Real-time CTF determination and correction. J Struct Biol *193*, 1-12.

Zheng, S.Q., Palovcak, E., Armache, J.P., Verba, K.A., Cheng, Y., and Agard, D.A. (2017). MotionCor2: anisotropic correction of beam-induced motion for improved cryo-electron microscopy. Nat Methods *14*, 331-332.

Zhu, S., Bradfield, C.J., Maminska, A., Park, E.S., Kim, B.H., Kumar, P., Huang, S., Kim, M., Zhang, Y., Bewersdorf, J.*, et al.* (2024). Native architecture of a human GBP1 defense complex for cell-autonomous immunity to infection. Science *383*, eabm9903.

Zou, Z., Meng, Z., Ma, C., Liang, D., Sun, R., and Lan, K. (2017). Guanylate-Binding Protein 1 Inhibits Nuclear Delivery of Kaposi's Sarcoma-Associated Herpesvirus Virions by Disrupting Formation of Actin Filament. J Virol *91*.

7 Appendix

Appendix A List of oligonucleotides

Appendix Table A. List of oligonucleotides used in this thesis for site-directed mutagenesis (see 3.2.2).

Oligonucleotide	Nucleotide sequence (5'-3')
Δ207-213_fw	A GGT GGA GGT AGT CAA AAA GAT GAA ACT TTT AAC C
Δ207-213_rv	GA TCC ACC GCC CAG GGA GTA TGT CAG GTA C
Δ207-216_fw	GGC GGA GGT TCT GAA ACT TTT AAC CTG CCC
Δ207-216_rv	AGA ACC TCC GCC CAG GGA GTA TGT CAG GTA C
Δ207-223_fw	GGT TCT CTC TGT ATC AGG AAG TTC TTC
Δ207-223_rv	TCC GCC CAG GGA GTA TGT CAG GTA C
M139D_fw	GGA ACC ATC AAC CAG CAG GCT GAT GAC CAA CTG TAC TAT GTG ACA
M139D_rv	TGT CAC ATA GTA CAG TTG GTC ATC AGC CTG CTG GTT GAT GGT TCC
M139E_fw	GGA ACC ATC AAC CAG CAG GCT GAG GAC CAA CTG TAC TAT
M139E_rv	ATA GTA CAG TTG GTC CTC AGC CTG CTG GTT GAT GGT TCC
M139R_fw	CC ATC AAC CAG CAG GCT AGG GAC CAA CTG TAC TAT
M139R_rv	ATA GTA CAG TTG GTC CCT AGC CTG CTG GTT GAT GG
D199A_fw	CAA CCC CTC ACA CCA GCT GAG TAC CTG ACA TAC
D199A_rv	GTA TGT CAG GTA CTC AGC TGG TGT GAG GGG TTG
D199K_fw	GGA CAA CCC CTC ACA CCA AAG GAG TAC CTG ACA TAC TCC
D199K_rv	GGA GTA TGT CAG GTA CTC CTT TGG TGT GAG GGG TTG TCC
RK(227-228)EE_fw	CT TTT AAC CTG CCC AGA CTC TGT ATC GAG GAG TTC TTC CCA AAG AAA AAA TGC TTT GT
RK(227-228)EE_rv	AC AAA GCA TTT TTT CTT TGG GAA GAA CTC CTC GAT ACA GAG TCT GGG CAG GTT AAA AG
A318*_fw	G GAG AAC GCA GTC CTG TAA TTG GCC CAG ATA GAG
A318*_rv	CTC TAT CTG GGC CAA TTA CAG GAC TGC GTT CTC C
Q577C_fw	GGA TTT CAA AAA GAA AGC AGA ATA ATG AAA AAT GAG ATA TGC GAT CTC CAG ACG AAA ATG AGA
Q577C_rv	TCT CAT TTT CGT CTG GAG ATC GCA TAT CTC ATT TTT CAT TAT TCT GCT TTC TTT TTG AAA TCC

Appendix B Cryo-EM data collection and processing

Appendix Table B. Cyro-EM data collection and processing for the membrane-bound GBP1 coatomer (EMD-18806) and polymeric GBP1 disks (EMD-18698). STA: subtomogram averaging, SPA: single particle analysis.

Data collection and processing	**EMD-18806**	**EMD-18698**
EM reconstruction method	STA	SPA
Microscope	FEI Titan Krios G3i	FEI Titan Krios G3i
Image detector	Gatan K3	Gatan K3
Magnification	42,000	81.000
Voltage (kV)	300	300
Electron exposure ($e^-/Å^2$)	130.0	60.6
Defocus range (μm)	-2.0 – -5.0	-0.7 – -2.0
Pixel size (Å)	1.1	0.53
Symmetry imposed	C1	C1
Initial number of sub-tomograms/particles	70.160	150.059
Final number of sub-tomograms/particles	6.146	15.952
Map resolution (Å)	26.8	37.0
FSC threshold	0.143	0.143

Appendix C Subtomogram averaging pipeline of membrane-bound GBP1

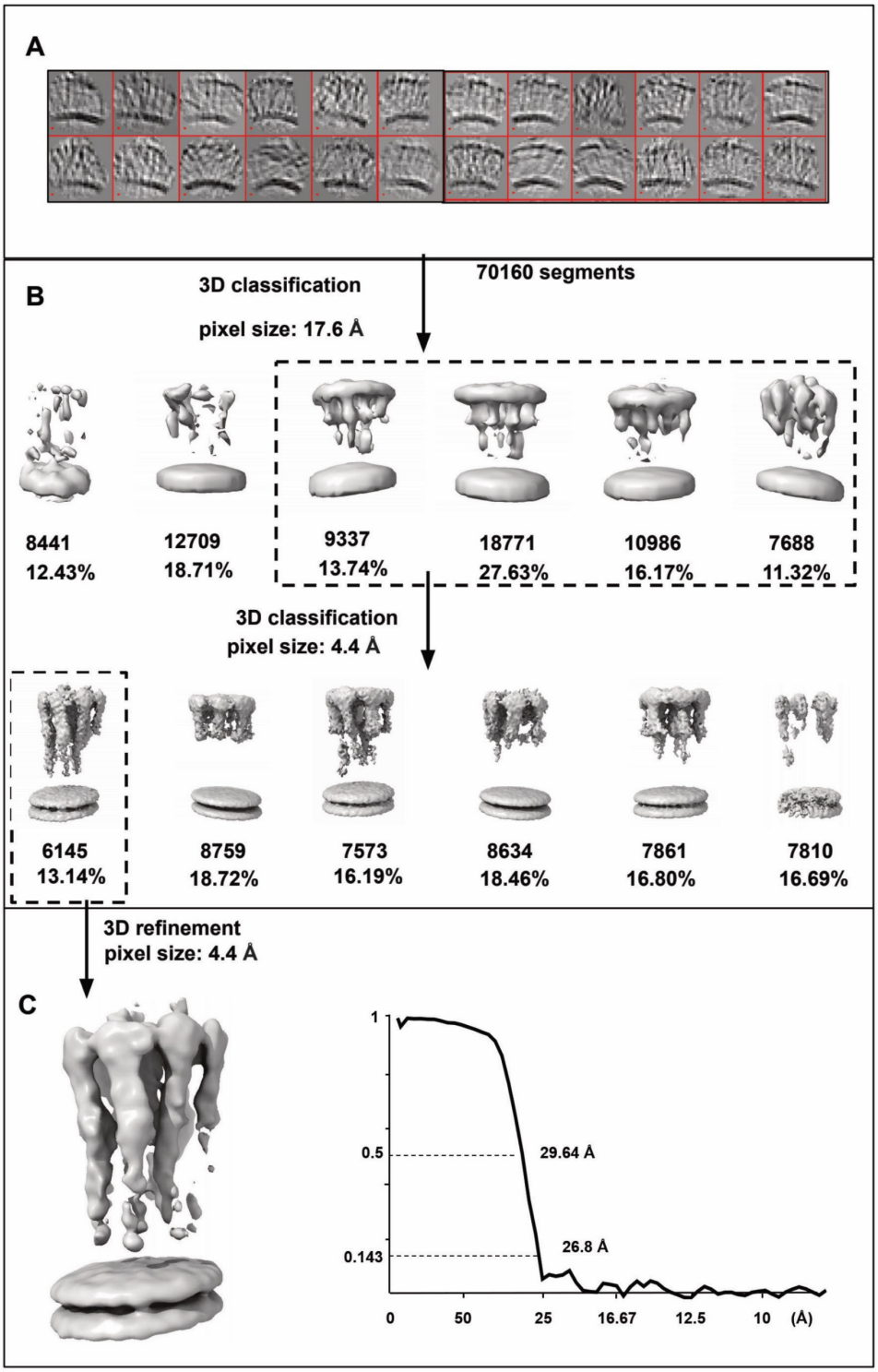

Appendix Figure C. Subtomogram averaging pipeline of membrane-bound GBP1. (A) Cropped segments from GBP1 tomograms are displayed by "dynamo_gallery". (B) Two steps of 3D classification were implemented in pixel size of 17.6 Å and 4.4 Å. Boxes of the dashed line denote the selected classes for next steps. (C) 3D refinement result of the selected class and gold-standard FSC curve. Map was low-passed to 25 Å. Figure was prepared by Xiaofeng Chu (Kudryashev Lab, Max-Delbrück-Center, Berlin).

Appendix D Image processing workflow for polymeric GBP1 disks

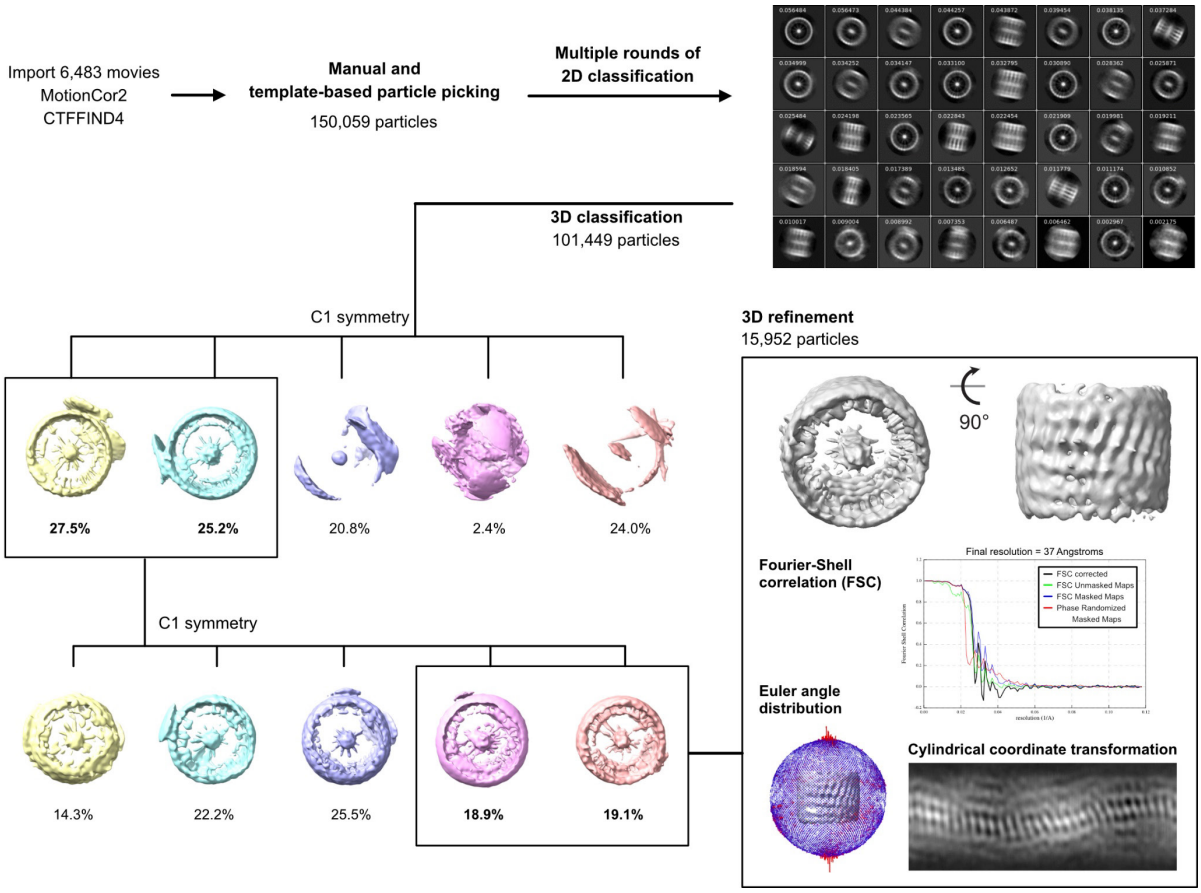

Appendix Figure D. Image processing workflow for polymeric GBP1 disks. Boxes denote selected 3D classes for next steps. 3D refinement result is shown together with gold-standard FSC curves, Euler angle distribution of particles contributing to the final reconstruction, and cylindrical coordinate transformation visualizing the surface of the 3D reconstruction at the heights of the peripheral LG domains.

Appendix E Abbreviations

(v/v)	volume per volume
(w/v)	weight per volume
2-ME	2-mercaptoethanol
A	absorbance or amplitude
a.u.	arbitrary unit
ASC	adaptor molecule apoptosis-associate speck-like protein containing a caspase recruitment domain
AU	absorbance unit
BPL	brain polar lipids
BSA	bovine serum albumin
CARD	caspase activation and recruitment domain
CF	correction factor
CTD	C-terminal domain
CV	column volume
Da	Dalton (g/mol)
DAMP	danger-associated molecular pattern
DMSO	dimethyl sulfoxide
DNA	deoxyribonucleic acid
DOL	degree of labeling
EDTA	ethylenediaminetetraacetic acid
EM	electron microscopy
FRET	fluorescence resonance energy transfer
GBP	guanylate-binding protein
GED	GTpase effector domain
HEPES	4-(2-Hydroxyethyl)piperazine-1-ethanesulfonic acid
HIC	hydrophobic interaction chromatography
His_6	hexahistidine tag
IFN-γ	Interferon-γ
IL	Interleukin
IMAC	immobilized metal affinity chromatography
IPTG	isopropyl β-D-1-thiogalactopyranoside
IRG	immune related GTPase
LB	Lysogeny Broth
LG	large GTPase
LPS	lipopolysaccharides
LRR	leucine rich repeat
MD	middle domain
MW	molecular weight
NF-κB	nuclear factor 'kappa-light-chain-enhancer' of activated B-cells
NLR	NOD-like receptor
OD	optical density
PAGE	polyacrylamide gel electrophoresis
PAMP	pathogen-associated molecular pattern

PCV	pathogen containing vacuole
PRR	pattern recognition receptor
PYD	Pyrin domain
ROS	reactive oxygen species
RT	room temperature
SDS	sodium dodecyl sulfate
SEC	size exclusion chromatography
SPA	single particle analysis
STA	subtomogram averaging
TEM	transmission electron microscopy
TLR	toll-like receptor
TNF	tumor necrosis factor
Tris	2-Amino-2-(hydroxymethyl)-1,3-propanediol
wt	wild type
λ_{em}	emission wavelength
λ_{ex}	excitation wavelength

One letter code and three letter code for amino acids

A	Ala	Alanine	I	Ile	Isoleucine	R	Arg	Arginine
C	Cys	Cysteine	K	Lys	Lysine	S	Ser	Serine
D	Asp	Aspartate	L	Leu	Leucine	T	Thr	Threonine
E	Glu	Glutamate	M	Met	Methionine	V	Val	Valine
F	Phe	Phenylalanine	N	Asn	Asparagine	W	Trp	Tryptophane
G	Gly	Glycine	P	Pro	Proline	Y	Tyr	Tyrosine
H	His	Histidine	Q	Gln	Glutamine			

Chemical elements are abbreviated with the general symbols of the periodic table. For amino acids, the general one-letter and three-letter codes are used.

Acknowledgements

I would like to take this opportunity to thank all those who have contributed to the success of this doctoral dissertation through their professional and personal support.

First, I would like to thank Prof. Dr. Oliver Daumke, who supervised and reviewed my thesis. I would like to express my sincere thanks for the assignment of this fascinating and challenging research topic, the helpful suggestions, the commitment in supervising this thesis, and the great support in publishing this work. I really appreciated the scientific freedom you gave me during my doctoral studies, that you were always around when I needed to discuss my project, and the positive work environment in your group.

I would also like to thank Prof. Dr. Mikhail Kudryashev for being second reviewer of this thesis and a member of my Thesis Advisory Committee. I would also like to thank Prof. Dr. Hagen Hofmann and Dr. Daniel Roderer as members of my Thesis Advisory Committee. It was great to receive your advice on my project. Your critical questions and the constructive discussions made an important contribution to the direction and outcome of this project.

The result of this work would not have been possible without the people I collaborated with. Many thanks go to Xiaofeng Chu and Misha Kudryashev for the efforts in image processing and subtomogram averaging of my dataset and the amazing outcome! Xiaofeng, thank you for taking this extra load of work, helping me when I faced problems with data processing, and answering the many questions I had. Many thanks also go to Miriam Kutsch not only for performing the in vitro binding assay with my constructs, but especially for increasing the impact of this story with your results. Miriam, thank you also for your contribution in preparing/editing/improving the manuscript, your useful suggestions, and your amazing expertise on GBP1. Many thanks also go to Paul Lauterjung and Christian Herrmann for providing protein for the structural studies and expertise on sample preparation and GBP1 biochemistry. It was a pleasure to collaborate with all of you!

Furthermore, I would like to thank the whole Daumke lab for the friendly work atmosphere and the constant willingness to help. In particular, I would like to thank Audrey Xavier for preparing me technically, scientifically, and mentally to work on the GBP1 project

and Yvette Roske for teaching me how to use the Talos, for all the technical and scientific support in EM and crystallization, and for helping me with the many questions I had. I would like to thank Elena Vázquez for giving me advice on tomogram reconstruction and subtomogram averaging in the beginning of my work and for answering all questions I had, Julia Smirnova for assistance in single particle analysis and all the useful suggestions about data analysis, Tobias Bock-Bierbaum and Katja Fälber for the discussions on my project, and all other members that provided me with scientific advice and support. Thanks also go to Caro Bernert and Jeanette Schlegel for their excellent support in the lab. Caro, I really enjoyed sharing the office with you and always having a person to talk to. I would also like to thank Varvara Plotnikova, Antonia Nowicki, and Fatma Bolhos not only for giving me the experience of supervising students, but also for your interest and effort in the lab to work with me on this project and supporting me with cloning and protein production. Further thanks go to Jeannine Engel for administrative support during this time. And of course, many thanks go to Eva Nathanail, Ashwin Natarajan, and Tobias Bock-Bierbaum for proofreading and giving this thesis the finishing touch.

I would also like to thank Thiemo Sprink, Metaxia Stavroulaki, and Christoph Diebolder from the core facility for cryo-EM at Charité Universitätsmedizin Berlin for cryo-EM grid preparation, data collection, and support on this project, as well as Oxana Krylova and Heike Nikolenko from the Biophysics Unit at Leibniz-Forschungsinstitut für Molekulare Pharmakologie (FMP) for providing access to the Jasco J-720 CD spectropolarimeter and assistance in performing the experiments.

Thanks also go to the iNAMES-MDC-Weizmann Helmholtz International Research School (HIRS) for Imaging and Data Science from the NAno to the MESo for funding and offering a truly interdisciplinary environment, in particular to all iNAMES members for having a great time during our peer mentor groups, seminars, workshops, and our retreat and to Sanja Drakulic for coordinating this program.

Last, I would like to thank my family and friends for all kinds of support during this time. Special thanks go to Larissa, who always supported me, no matter what happened. This work would not have been possible without her.